EVALUATION OF CYCLOTRON PRODUCED RADIOMETALS FOR RADIOLABELING

OF IMMUNO- AND BIO-CONJUGATES FOR NUCLEAR IMAGING

by

Gemma Marie Dias

M.Sc. Medical Biophysics, Western University, 2010
B.Sc. Medical Biophysics and Biomaterials, Western University, 2008

A THESIS SUBMITTED IN PARTIAL FULFILLMENT OF

THE REQUIREMENTS FOR THE DEGREE OF

DOCTOR OF PHILOSOPHY

in

THE FACULTY OF GRADUATE AND POSTDOCTORAL STUDIES

(Interdisciplinary Oncology)

THE UNIVERSITY OF BRITISH COLUMBIA

(Vancouver)

August 2017

Abstract

The development of novel bioconjugates; antibodies, antibody mimetics and peptides is revolutionising the targeted molecular imaging approach to oncology. Many bioconjugates with high and specific uptake in tumours are transitioning into clinical oncology imaging. Monoclonal antibodies are returning to diagnostic imaging due to the clinical impact and commercial success of many disease-modifying monoclonal antibodies and antibody-drug conjugates. One hindrance to mAb based imaging is their long biological half-life; requiring days to visualise high tumour-to-non-target contrast. A variety of avenues to improve the contrast and clearance of circulating mAbs are in development. Radiometals that are well suited for imaging antibodies as well as antibody mimentics or peptides are becoming more in demand as clinical translation occurs. Current constraints and requirements for conventional radiometal production can limit the accessibility to certain cyclotron centers and may not be easily integrated into existing cyclotron centers. Efforts have been made to modify conventional radiometal production by introducing a liquid target approach. Limitations with yield and purification methods are hindering the feasibility of producing radiometals with a liquid target.

Herein, we propose to produce radiometals with a liquid target and compare yields, optimize purification procedures to ensure high radiolabeling yields and assess their usefulness to radiolabel existing and novel bioconjugates. Additionally, we use a variety of strategies to improve tumour-to-non-target contrast ratios and pharmacokinetics of mAbs which can be applied to imaging of novel mAbs.

We demonstrate the ability to produce and purify ^{89}Zr with both a solid and liquid target with sufficient yields for radiolabeling of antibodies. We demonstrate that liquid target produced ^{89}Zr is a suitable alternative approach to conventional solid target ^{89}Zr by demonstrating suitable antibody radiolabeling yields for *in vivo* imaging. We demonstrate that liquid target produced ^{68}Ga can be separated effectively from the staring zinc material and from other metal impurities. This successful purification enabled high radiolabeling of DOTATOC. The radiolabeled ^{68}GaDOTATOC from liquid target ^{68}Ga was compared with an *in vivo* study to that of

conventional generator ^{68}Ga. We demonstrate the feasibility of producing, purifying and radiolabeling liquid target ^{68}Ga for *in vivo* imaging.

Lay Abstract

Traditional production of radiometals for cancer imaging requires the use of cyclotron with a solid target system. This method may not be easily integrated into current cyclotron centres and requires an extensive dedicated solid target set up and specific expertise. New methods of radiometal production with a liquid target offer the opportunity to expand the availability of radiometals to a large number existing cyclotron facilities with minimal investments. We explore the feasibility of producing radiometals with a liquid target on a clinical cyclotron. Here we successfully produce radiometals with sufficient yields and optimise purification process to enable high radiolabeling of antibodies and peptides for preclinical cancer imaging.

Preface

All chapters are based on work primarily conducted at the BC Cancer Agency and BC Cancer Research Centre in Dr. Francois Benard's laboratory.

In chapter 2, I conjugated and radiolabeled Trastuzumab and E-cadherin antibodies with ^{111}In. The determination of the number of chelates and the immunoreactivity assay for chelator studies were performed by Julie Rousseau and Caterina Ramogida (post-doctoral fellows, (PDF)). I prepared xenograft models of the mice, including surgical implantation of estrogen pellet. Injection of the mice and μSPECT were conducted with assistance from Nadine Colpo and Navjit Hundal (Nuclear Medicine Technologists, (NMT)). I prepared samples for *in vitro* and *ex vivo* E-cadherin analysis and flow cytometry data was conducted with assistance by Helen Merkens (lab technician), Chengcheng Zhang and Julie Rousseau (PDFs). I compiled and performed statistical analysis of the acquired data.

In chapter 3, I worked with cyclotron operators (Jean-Pierre Appiah, Wade English and Julius Klug) to optimize irradiation parameters. I performed all the ^{89}Zr purification procedures with hydroxamate resin which I made in-house. I conjugated and radiolabeled Trastuzumab and E-cadherin antibodies with ^{89}Zr studies. Number of chelates and immunoreactivity studies were performed jointly with Julie Rousseau (PDF). I prepared xenograft models of the mice, including surgical implantation of estrogen pellet. Injection of the mice and μPET were performed jointly with assistance from Nadine Colpo (NMT) and Julie Rousseau. I compiled and performed statistical analysis of the acquired data.

In chapter 4, I was the lead in this project and responsible for production and purification of all solid-target produced ^{89}Zr. In collaboration with TRIUMF, Caterina Ramogida (PDF) performed purification of liquid-target produced ^{89}Zr. With the assistance of Julie Rousseau (PDF), we cohesively performed radiolabeling, number of chelates and immunoreactivity studies. μPET imaging and biodistribution of was jointly performed. I compiled and performed statistical analysis of the acquired data.

In chapter 5, I was the lead in this project and was responsible for the preparation of the zinc oxide starting material and the production of ^{68}Ga. I worked with cyclotron operators, Wade English and Julius Klug to optimize irradiation parameters. In collaboration with TRIUMF with assistance from Caterina Ramogida (PDF) and Petra Martini (Phd student) we optimized purification conditions for liquid target produced ^{68}Ga. I prepared xenograft models of the mice, including surgical implantation of estrogen pellet. We cohesively radiolabeled DOTATOC for a comparison study. With assistance from Nadine Colpo (NMT) I injected the mice and performed μPET acquisitions while Caterina and I jointly performed biodistribution studies. I compiled and performed statistical analysis of the acquired data.

The research in this thesis was conducted under animal protocols A15-0238, A11-0185 and A15-0185, which were approved by the Institutional Animal Care Committee of the University of British Columbia in compliance with the Canadian Council on Animal Care Guidelines

Table of Contents

List of Tables

List of Figures

List of Abbreviations

%ID/g	% injected dose per gram
^{18}F-FDG	2-deoxy-2-[^{18}F]fluoro-D-glucose
^{18}F-FES	16-α[^{18}F]fluoro-17β-oestradiol
Abdegs	Engineered antibodies
ACSI	Advanced Cyclotron Systems Inc
ADCC	Antibody-dependent cell-mediated cytotoxicity
β$^-$	Beta
β$^+$	Positron
BCCA	BC Cancer Agency
Bn	Benzyl
C18	Carbon 18
cc	Cubic centimeters
CDC	Complement-dependent cytotoxicity
CDH1	Cadherin 1
CHX	Cyclohexyl
CO_2	Carbon dioxide
CT	Computed tomography
cyclo	Cyclotron
d	Diameter
DFO	Desferrioxamine
DGA	N,N,N',N'-tetra-n-octyldiglycolamide
DMSO	Dimethylsulfoxide
DOTA	1,4,7,10-Tetraazacyclododecane-N,N',N'',N'''-tetraacetic acid
DOTATOC	DOTA-Phe1-Tyr3 octreotide
DTPA	Diethylenetriaminepentaacetic acid
EC	Electron capture
E-Cadherin	Epithelial cadherin
EDTA	Ethylenediaminetetraacetic acid
EGFR	Epidermal growth factor receptor
EMT	Epithelial mesenchymal transition
EOB	End of bombardment
EPR	Enhanced permeability retention
ER	Estrogen receptor
Fab	Fragmentation binding
Fc	Fragment crystallisable
FcRn	Fc neonatal receptor
FcϒR	Fc gamma receptor
Fe	Iron

g	Gram
GBq	Gigabequerel
Ge	Germanium
gen	Generator
GMP	Good Manufacturing Practices
h	Hour
HCl	Hydrochloric acid
HEPES	4-(2-hydroxyethyl)-1-piperazineethanesulfonic acid
HER2	Human epidermal grown factor receptor 2
HPLC	High pressure liquid chromatography
IgG	Immunoglobulin G
ILC	Invasive lobular carcinoma
iTLC	Instant thin layer chromatography
IV	Intravenous
kDa	kilodaltons
KeV	kilo electron volts
L	Litre
LT	Liquid target
M	Molar concentration
mAb	Monoclonal antibodies
MBq	Megabecquerel
MeCN	Acetonitrile
MeV	Mega electron volt
min	Minute
mL	Millilitre
mm	Milimeter
mM	Millimolar
Mol	Mole
MW	Molecular weight
n	Neutron
Na_2CO_3	Sodium carbonate
NaCl	Sodium chloride
NaI	Sodium iodide
nm	Nanometer
nmol	Nanomole
NSG	NOD.Cg-$Prkdc^{scid}Il2rg^{tm1Wjl}$/SzJ
O_2	Oxygen
OSEM3D	3 Dimensional order-subsets expectation maximization
p	Proton
PBS	Phosphate buffered saline

PET	Positron emission tomography
pH	Potential of hydrogen
ppm	Parts per million
psi	Pounds per square inch
RCY	Radiochemical conversion yield
RF	Radiofrequency
Rf	Retention factor
s	Seconds
SA	Specific activity
SCN	Isothiocyanate
SD	Standard deviation
SEC	Size exclusion chromatography
SPECT	Single photon emission tomography
ST	Solid target
t	Tumour
$T_{1/2}$	Half life
TRIUMF	Tri-University Meson Facility
μA	Micro amp
μg	Microgram
μL	Microlitre
UV	Ultraviolet
$Y(NO_3)_3$	Yttrium nitrate
$Zn(NO_3)_2$	Zinc nitrate
ZnO	Zinc oxide
$ZrCl_4$	Zirconium chloride

Acknowledgements

To my parents, Jeff and Melinda and my brother Alex.

Chapter 1: Introduction

1.1   Molecular Imaging

Molecular imaging is a rapidly evolving and growing multidisciplinary field due to the advances in molecular biology, probe development, imaging technology, nuclear chemistry and radiopharmacy. It is being recognized as having the potential to impact and improve cancer treatment and management. This multifaceted approach to diagnostics is paving the way for improved personalized cancer care [1]. Molecular imaging involves non-invasive monitoring of biological events at the cellular level and is often accompanied with the acquisition of associated anatomical information. To obtain optimal information imaging probes consisting of a targeting and signaling component are required. The targeting component is typically a biological compound (small molecule, peptide, antibody or antibody fragments) while the signaling component is a radionuclide, fluorochrome or paramagnetic chelate. The diversity of the signaling component of molecular imaging probes requires the use of an appropriate method of detection.

1.2   Nuclear Medicine Imaging Modalities

There are several imaging modalities that encompass the umbrella of molecular imaging; these non-invasive modalities are designed for detection of a specific type of signaling component and have unique properties and advantages. Nuclear medicine imaging modalities are used for imaging probes bound to a radionuclide provide physiological and metabolic information. Optical imaging will detect imaging probes by fluorescence or optical tags for molecular information. Magnetic resonance imaging will detect paramagnetic chelates for both anatomical or physiological information [2]. Computed tomography (CT) is a diagnostic tool for its ability to obtain anatomical information based on tissue density differences. High resolution capabilities on the order of 50 μm are achievable with CT and provide excellent anatomical information [2]. While CT is used as a standalone modality for diagnostics, the integration of CT with nuclear medicine imaging modalities enables the dual acquisition of functional

information coupled with anatomical information. More importantly attenuation correction from the acquired CT images improve visualization quality and quantitative accuracy of the images [3].

Single photon emission computed tomography (SPECT) is the predominant imaging modality used in general nuclear medicine. SPECT imaging involves the detection of single photon emissions by the use of a scintillation detector. The detector is comprised of collimator and a scintillator in the form of sodium iodide crystal and photomultiplier tubes (Figure 1.1). The emitted photons from the radioactive source injected into the patients pass through the collimator holes and cause a scintillation event in the form of lower energy photons within the crystal. Photomultiplier tubes situated next to the scintillator converts these lower energy photons to electric signals [4] .The two-dimensional images that are acquired at different angles around the patient are collated to generate a three-dimensional estimation of the distribution of radioactivity [5]. The collimators play an integral role in sensitivity and resolution of the acquired images. Typically, sensitivity and resolution are in constant competition. Low-energy collimators have thinner septa and come with various hole sizes. Collimators with larger holes accept more photons which increase sensitivity, while smaller holes are less sensitive but provide improved spatial resolution. Most collimators are made of lead and some with tungsten, which make for heavy and expensive equipment. Low energy collimators are appropriate for low energy radioisotopes such as thallium-201 (^{201}Tl), technetium-99m (^{99m}Tc) and iodine-123 (^{123}I). Medium collimators have thicker collimators for higher energy radioisotopes such as gallium-67 (^{67}Ga) or indium-111 (^{111}In). For iodine-131 (^{131}I), ultra-high energy collimators are required; these collimators can also be used for SPECT imaging of 511 keV annihilation photons from position emitting radionuclides. SPECT is predominately utilized for myocardial imaging using ^{99m}Tc based radiopharmaceuticals or ^{201}Tl. In addition to myocardial imaging, there are several SPECT based radiopharmaceuticals used for oncology diagnostic scans [3].
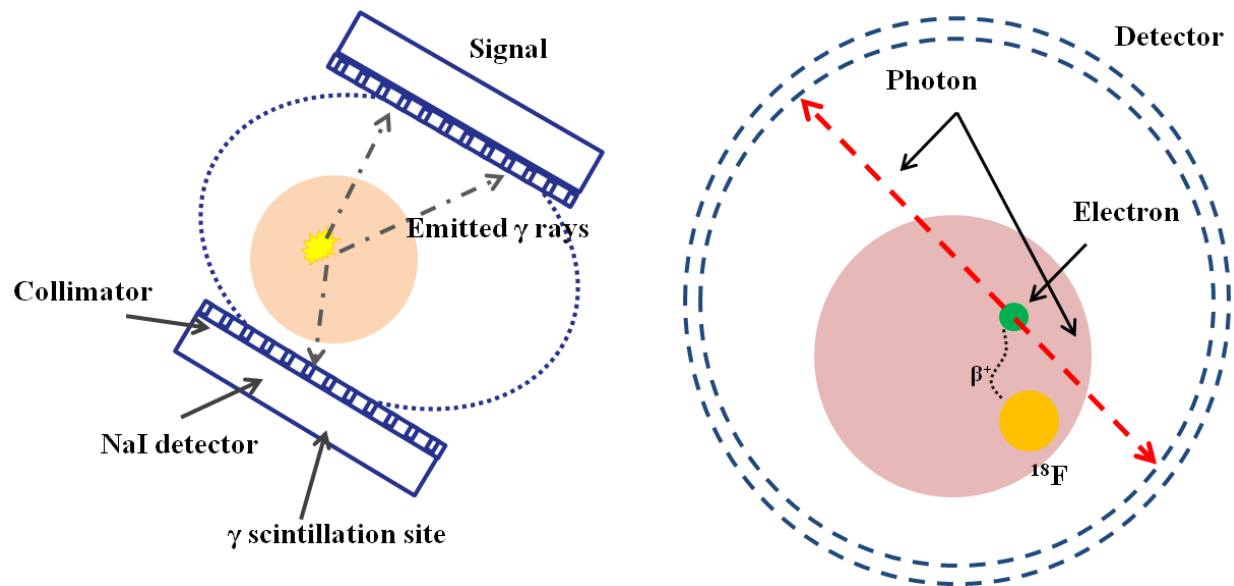
Figure 1.1 A schematic of the principles of SPECT (left) and PET (right) scanners.

Positron emission tomography (PET) is a widely-used modality for oncology diagnosis, staging and treatment management. The use of PET has shown to have a substantial impact on patient management and care. Over the past decade, the number of PET centers in Canada alone has increased. In 2011, there were 34 publicly funded PET centers with 45 scanners distributed over 8 provinces [6]. Positron emission tomography with computed tomography (PET/CT) enables the acquisition of metabolic and anatomical information. PET scanners detect the emission of positrons from positron emitting radioisotopes. The positron that is emitted from the radioisotope annihilates with a nearby electron causes the release of two 511 keV photons. These photons are emitted at approximately 180° (180° ± 0.25°) from each other and are detected when they reach the sodium iodine crystals. Photomultiplier tubes converts the light photons produced in the detectors to an electrical pulse. Unlike SPECT scanners, PET imaging does not require the use of collimators and thus spatial resolution in general is higher. The choice of radioisotope contributes to spatial resolution and the distance by which a positron travels before annihilation with an electron is called the positron range. The positron range is an effective range of the shortest distance from the emitted nucleus to the annihilation; lower positron ranges give rise to higher resolution images [7]. Fluorine-18 (^{18}F) has one of the shortest mean positron ranges of 0.66 mm used for PET imaging [8].

1.3 Cancer Imaging

1.3.1 Fluorodeoxyglucose

[18]F is predominately used in clinical oncology to radiolabel a glucose derivative as 2-deoxy-2-[^{18}F]fluoro-D-glucose (^{18}F-FDG). Oncology, encompasses almost 90% of clinical PET scans, with the rest taken up by cardiology and neurology [9]. PET plays an important role in oncology, serving as an effective tool for detection and localization of primary tumours, differentiating between tissue types; benign and malignant, staging, treatment planning and monitoring response to treatments [10]. The standard for PET oncology imaging is ^{18}F-FDG; it serves as a powerful tool for the detection of a variety of cancers [10, 11]. The glucose analogue provides functional information based on the uptake and glycolysis of cancer cells. It is transported via glucose transporters into cells. Once internalized, is phosphorylated to form FDG-6-phosphate and is trapped in the cells [12]. ^{18}F-FDG imaging has been shown to be effective imaging tool for staging, restaging and treatment monitoring [13], however it not cancer-specific [14]. Uptake in inflammatory processes and brown adipose tissue contributes to a lower specificity of ^{18}F-FDG [15]. For low metabolic tumours or small tumours that may have low requirements for glucose they can exhibit low ^{18}F-FDG avidity [16]. There is a drive for development of imaging molecules or vectors that can provide more specific and targeted options to image the complex and diverse nature of tumours.

1.3.2 Targeted Approach to Breast Cancer Molecular Imaging

The targeted approach to molecular oncology imaging offers the opportunity to obtain specific information regarding proteins, receptors or antigens associated with a tumour and to classify or characterize the tumour *in vivo* [1, 17]. Specifically, for imaging, the use of targeted tracers can be used as a standalone diagnostic tool to provide more specific information that cannot be ascertained or concluded by ^{18}F-FDG alone. Estrogen receptor targeting is an example of the importance of targeted imaging approach thay may have a positive impact on patient care and health care costs [18]. Conventional methods of tumour information acquisition require biopsies; an invasive procedure which is limited by sampling error and tumour heterogeneity and often requires multiple sampling [19]. The radiotracer 16-α[^{18}F]fluoro-17β-oestradiol (^{18}F-FES) targets estrogen receptor (ER) expression. Imaging with ^{18}F-FES is used to obtain baseline

tumour information to ascertain a course of treatment. In Figure 1.2, uptake of ^{18}F-FDG in a patient identifies the presence of multiple tumour nodes. With the same patient, the uptake of ^{18}F-FES identifies only some of the nodes. This would suggest a difference in tumour expression of estrogen receptors and some nodes will benefit from treatment; ultimately altering the course or effectiveness of treatment.
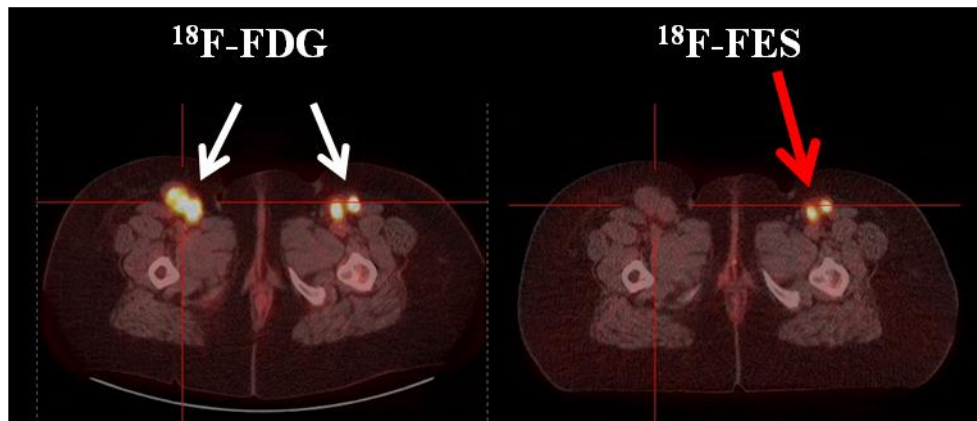
Figure 1.2 A PET/CT fused image of ^{18}F-FDG uptake (left) and ^{18}F-FES uptake (right). Uptake of ^{18}F-FDG indicates presence of multiple tumour nodes. On the other hand, the uptake of ^{18}F-FES identifies a difference in estrogen receptor expression in the nodes. Figure courtesy of F. Bénard.

There are many other receptors that have been targeted and are used for both *in vivo* and *ex vivo* diagnostic analysis. The human epidermal growth factor 2 (HER2) induces intracellular signaling pathways in response to extracellular signals. The involvement of HER2 in human breast cancer pathogenesis was established 30 years ago [20]. The HER2 protein structure consists of an extracellular ligand binding domain, a transmembrance domain and an intracellular tyrosine domain [21-23]. Over expression of the HER2 protein is seen in approximately 25-30% of breast and ovarian cancers [22, 24]. Breast cancers with amplified HER2 have a higher propensity for progression and are accompanied with a poor prognosis. It is a tumour marker that has played a role in not only identifying breast cancer sub type but also a target for therapy [25, 26]. Trastuzumab is a monoclonal antibody (mAb) that binds to the extracellular domain of

HER2 and inhibits proliferation and cell survival [27, 28]. Obtaining information of HER2 expression *in vivo* in primary or metastatic sites has provided a method for monitoring efficacy of treatment and adjusting treatment if necessary [23].

The epithelial cell-cell adhesion molecule cadherin 1 (CDH1 or E-cadherin) is a transmembrane glycoprotein epithelial marker found and expressed in adherent junctions between normal epithelial cells. E-cadherin expression offers another target for breast cancer tumours. Many breast cancers anarchically overexpress E-cadherin [29, 30]. It has been established that E-cadherin expression can aid in the diagnosis of invasive lobular carcinoma (ILC). Mutations in E-cadherin resulting in the loss of E-cadherin expression is linked to mesenchymal transition and propensity to metastasize to regional lymph nodes in breast cancer [31]. Triple negative breast cancers showed a reduction of E-cadherin expression; which is associated with poor outcome especially in patients in stage II disease [32]. When metastatic cells with low E-cadherin home to new sites, E-cadherin expression is restored. There has been a link between E-cadherin positive cases at stage II of diagnosis having better prognosis than E-cadherin positive cases in stage I [32]. Due to its function as a cell-to-cell adhesion glycoprotein, it is most likely not readily accessible for targeting in normal tissues [33]. However, due to the leaky vasculature of and high and anarchic expression of E-cadherin in tumours opens the possibility to target this protein. E-cadherin serves as a predictive marker to classify subgroups of breast cancer and the change in expression of the primary tumour could be used as a marker for metastatic potential.

1.4   Bioconjugates for Molecular Targeted Imaging.
1.4.1   Antibodies

Monoclonal antibodies (mAb) are powerful therapeutic and diagnostic tools due to their high target specificity and ability to induce effector functions for therapeutic response [34, 35]. In the last 20 years, antibodies as a tool for therapeutic treatment are considered one of the most successful strategies in oncology treatment [35]. Immunoglobulins (IgG), a type of antibody, are heavy glycoproteins typically on the order of 150 kilodaltons (kDa). The "Y" shaped protein consists of four polypeptide chains, two of which are identical heavy chains (~ 55 kDa) and two identical light chains (~ 25 kDa) all bound by disulfide and noncovalent bonds. Each light chain contains one variable (V_L) and one constant domain (C_L), while each heavy chain contains one

6

variable (V_H) and 3 constant domains (C_H) [36, 37]. The variable domain and one constant domain comprise the fragment antigen binding (Fab) regions of the antibody. The carboxy terminal sections of the heavy chains comprise the fragment crystallizable (Fc) region of the antibody Figure 1.3. The Fc region is involved in promoting enhanced serum half-life to maintain circulation of antibodies but also is involved in recruiting effector functions for a therapeutic response [35]. The CH1-CH2 domain is involved in Fc gamma receptor (FcγR) binding for antibody effector functions while the CH2-CH3 domain of the Fc is responsible for binding to the Fc neonatal receptor (FcRn), involved in recycling of mAbs [38].
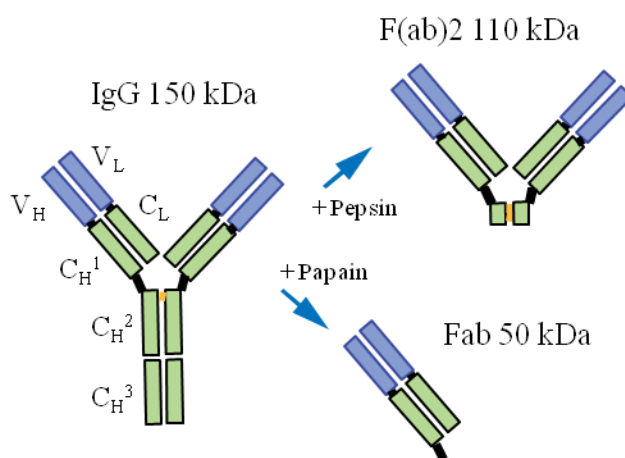
Figure 1.3 Antibody schematic of whole intact IgG of 150 kDa and antibody fragments: (Fab)2 from IgG digestion with pepsin or Fab from IgG with incubation with papain.

The binding and interaction of the Fc region of the IgG to the FcRn contributes to the pharmacokinetics of the IgG. The FcRn has been shown to extend the serum half-life of albumin and in FcRn deficient mice the percentage of circulating albumin is 40% of normal levels [37, 39-41]. Circulating IgG in the blood (in a physiological pH environment) are taken up by endothelial cells and or monocytes. Within the endothelial cells, the acidic conditions of the endosome permit the binding of the IgG to FcRn. The bound IgG-FcRn complex migrates to the surface of the cell and is released back into the normal physiological blood. Any IgG not bound to FcRn will be sorted for lysosomal degradation. This relationship between Fc region of the IgG and FcRn can be manipulated to either enhance circulation of the mAb or enhance degradation and clearance of IgG from the circulatory system. Attempts have been made to

increase IgG turnover by saturating or blocking IgG binding to FcRn with either high doses of intravenous IgG or modification of the Fc portion of the IgG or injection anti-Fc antibodies [39]. One major factor to the interaction of Fc and FcRn and recycling of mAbs is the amount of mAb in circulation. When higher levels of mAb is present, more of the mAb will be sorted to lysosomes for degradation, while with lower levels of mAb, more will be recycled for recirculation. While an increase in injected mAb may improve the tumour uptake of the mAb, there is a point at which the binding sites of the tumour will become saturated and excess mAb will remain in circulation. Clinical studies demonstrate the effect of injected mAb mass on tumour uptake and localization. In general, an increase in injected mAb improved the localization and reduced the time required to visualize the tumour [42].

The internalizing or non-internalizing properties of antibodies once bound to the antigen impacts the route of therapeutic action and diagnostic potential [43]. Non-internalizing antibodies that engage at cell surface receptors can activate or inhibit signaling, activate antibody-dependent cell-mediated cytotoxicity (ADCC) or complement-dependent cytotoxicity (CDC) [35]. Internalizing antibodies can induce a therapeutic response by delivering toxins within the cytoplasm. With both approaches, it is the antigen-binding domain of the antibody, located on the Fab region of the antibody that is crucial to targeting antigens on the cell surface. There are a variety of mAbs that target a variety of tumour associated antigens subtypes. In breast cancer particularly, the use of the mAb Trastuzumab as a therapeutic to target HER2 has been very effective in improving patient outcomes [7, 27, 44]. There has been a development in imaging of HER 2 expression using a variety of techniques including the use of radiolabeled Trastuzumab [45-47]. The therapeutic success of mAbs has pushed the development for antibody based imaging to obtain not only tumour antigen expression of the primary tumour, but also to assess expression in any metastatic sites or in the primary tumour over the course of treatment [48].

1.4.2   Antibody Fragments and Mimetics

Antibodies are limited for imaging by their biological half life and there are ways to make compounds that have the same binding affinity but with faster clearance. Separating the Fab from the Fc domain will result in an intact compound that binds to the antigen or receptor with the same specificity as whole intact mAb. Incubation of mAb with papain separates the Fab

region into 2 fragments and from the Fc fragment [49, 50]. Incubation with pepsin, cleaves the mAb below the disulphide bonds cleaving the Fc into small fragments and leaves an intact F(ab')2 region [49, 51]. The removal or separation of the Fc from the mAb alters the pharmacokinetics of these newly formed fragments; most notably, a reduction in serum half-life and alteration of clearance route (Table 1.1). Further constructs such as minibodies, diabodies can be made with modifications to reduce molecular weight and serum half-life. Achieving high tumour contrast at earlier time points negates the need for radioisotopes with long half lives [52, 53]. This is advantageous as there are many short-lived isotopes suitable for imaging small molecular weight antibody constructs than long lived isotopes for intact whole mAb. Affibodies are engineered protein molecules that are derived from the domain of the IgG region of staphylococcal protein A. These antibody mimetics are typically 58 amino acids long and in the range of ~6 kDa. Due to their small molecular weight, they are cleared via the renal pathway. Due to the faster clearance of these mimetics compared to whole intact mAb, tumour imaging is achievable within hours rather than days. The beneficial nano or picomolar affinities of affibodies make them ideal conjugates for targeted imaging. In addition, the radiolabeling of affibodies is not constrained by pH or temperature [54, 55]. This allows a facile radiolabeling approach with established conditions to a variety of short lived radioisotopes. The development of faster clearance antibody constructs and mimetics require suitable short lived radioisotopes suitable for imaging.

Table 1.1 Antibody and antibody constructs. Adapted with permission from Freise and Wu [56]

	Format	Molecular Weight (kDa)	Serum half-life	Clearance route	Radioisotope to satisfy half-life
	Intact IgG	150	1 – 3 weeks	Hepatic	^{111}In, ^{124}I, ^{89}Zr
	F(ab')2	110	8 – 10 h	Hepatic	^{64}Cu, ^{99m}Tc
	Minibody	75	5 – 10 h	Hepatic	^{64}Cu, ^{99m}Tc
	Fab	50-55	12 – 20 h	Renal	^{61}Cu, ^{44}Sc, ^{64}Cu
	Diabody	50	3 – 5 h	Renal	^{61}Cu, ^{44}Sc
	scFv	28	2 – 4 h	Renal	^{18}F, ^{68}Ga, ^{61}Cu, ^{44}Sc
	Nanobody	12-15	30 – 60 min	Renal	^{18}F, ^{68}Ga
	Affibody	6	30 – 60 min	Renal	^{18}F, ^{68}Ga

1.4.3 Peptides

Peptides are a different type of bioconjugate used for targeted imaging; these short amino acid sequences (< 50 amino acids) can vary in molecular weight, charge and lipophilicity. While mAbs and antibody constructs enable high specific targeting, they are also accompanied with limitations or constraints in permeability, clearance and radiolabeling conditions [57]. Peptide based radiotracers that target receptors offer an avenue for high specific targeting without such constraints. There has been extensive development of peptides aimed to target receptors found in a variety of cancers [57, 58]. Such receptors include somatostatin receptors, gastric releasing peptide receptors, melanocortin-1 receptors and bradykinin receptors to name a few [58-60].

Many of these peptides have been radiolabeled and tested *in vivo* for their biodistribution in tumour bearing mice. The primary concern with peptide based radionuclide therapy is the clearance through the renal pathway potentially contributing to nephrotoxicity, although this is not a concern for imaging due to lower administered doses [61]. One benefit of peptides is the ability to make small modifications in the amino acid sequence to alter pharmacokinetics or stability of the peptide [59]. Unlike with mAb based imaging where more mAb provides optimal tumour visualization, increasing the peptide dose can contribute to saturation of the receptor. This limits the ability to visualize the tumour with high contrast due to increased background and non-specific binding [57]. Radiolabeling approaches with peptides should ensure high specific activity of the final labeled peptide.

1.5   Radioisotopes for Bioconjugates

In nuclear medicine imaging many factors contribute to the selection of the radioisotope. Firstly, the application whether diagnostic or therapeutic plays a crucial role [62, 63]. Here the emission type governs the effectiveness of the radioisotope for the intended application. Diagnostic applications such as SPECT or PET require radioisotopes that emit gammas, while therapeutic applications require radioisotopes that emit alpha and beta particles [63]. Decay characteristics such as energy emission will factor in when taking into account dose to a patient. The physical half-life of the radioisotope should complement the biological half-life of the intended molecule or bioconjugate to be radiolabeled [64, 65]. Production methods of the intended radioisotope as well as the cost or availability of the starting material and the efficiency of the purification method further impact the choice of radioisotope. The production of radioisotopes can be classified into neutron rich, requiring the use of a reactor or neutron deficient, requiring production via a particle accelerator. A few radioisotopes produced via either method then serve as the starting material (parent) for downstream (daughter) radioisotopes. The daughter radioisotopes are obtained through chemical separation with the use of a generator.

1.5.1   Radioisotopes for Diagnostic Imaging

Carbon-11 (^{11}C), nitrogen-13 (^{13}N), oxygen-15 (^{15}O) and fluorine-18 (^{18}F) are radioisotopes used clinically for PET. ^{11}C, ^{13}N and ^{15}O with short half-lives (20.3, 9.9 and 2.0 min respectively) are

produced on a cyclotron [66] and can directly substitute naturally occurring atoms to radiolabel molecules of interest without disturbing or effecting their normal biological processes [67]. Efficient production of radiotracers with either of the aforementioned radioisotopes must be done within a short time points and can be a challenge due to the short half-lives. ^{18}F, also a positron emitter has a longer half-life compared to the other conventional isotopes at 109 min. Sufficient amounts of ^{18}F can be produced, radiolabeled to FDG and quality control conducted within a few hours to service a clinical PET department. In addition, ^{18}F-FDG can be produced and transported to other clinical PET departments that do not have a cyclotron; extending the use of PET to rural areas. While the half-life of a radioisotope certainly plays a factor for PET imaging the decay properties are just as important. ^{18}F has a short mean linear positron range of 0.6 mm, which is the distance between the radioisotope and annihilation with nearby electrons. This contributes to the resolution; shorter positron ranges result in higher resolution. Table 1.2 lists the decay properties, half-lives, positron ranges and production methods of commonly used radioisotopes. ^{18}F is suitable for radiolabeling and imaging of short half-life compounds such as glucose, however, for longer circulating compounds such as antibodies, longer half-life radioisotopes are required.

1.5.1.1   Diagnostic Radioisotopes for Antibody Imaging

The use of radiolabeled IgGs for targeting and cancer treatment emerged in the 1950s [68]. Iodinated radiolabeled antibodies were the first to be used clinically. Due to the availability of iodine and the ability to radiolabel amino acids, ^{125}I and ^{131}I were used for antibody radiolabeling. While antibodies are easily iodinated, ^{125}I or ^{131}I are note ideal for imaging due to their physical gamma emission. ^{123}I offered a possibility for better image detection capabilities; however, low stability and limited but expensive availability of the isotope rendered this isotope less desirable for antibody imaging [69]. An alternate radioisotope easily or readily available with properties suitable for imaging detection and a physical half-life matching that of the biological half-life of circulating mAbs was needed for radiolabeled mAbs. Already established for diagnostic use, ^{111}In provided an option for mAb radiolabeling. The physical half-life of 2.8 days is ideal for a mAb and the gamma emissions of 173 keV and 247 keV are detectable on clinical available instruments [70]. However, unlike the iodine isotopes ^{111}In cannot be used for

directly radiolabeling antibodies. As such; a bifunctional chelator to link the antibody and radiometal is required. Chelators and radiolabeling systems have expanded the options for radioisotopes for antibody imaging and will be discussed later in section 1.6. The development of the PET scanner, the use of ^{18}F-FDG and the limited positron emitters suited for PET imaging rendered antibody based imaging to be almost obsolete. However, the high specificity of antibodies accompanied with the high sensitivity and resolution of PET encouraged the production of positron emitting radioisotopes. In addition to matching the half-life of an antibody, the radioisotope must be compatible with the mechanisms of antibody-antigen binding. The positron emitter ^{124}I, served as an option for radioimmuno PET imaging, however, once internalized, the iodinated antibody complex is degraded. The iodine permeates out of the cell leading to lower tumour contrast. Positron emitters such as copper-64 (^{64}Cu), yttrium-86 (^{86}Y) and zirconium (^{89}Zr), are trapped once internalized and have been used for radioimmuno PET imaging. The 12.7 h half-life of ^{64}Cu permits imaging up to 48 h post injection which isn't optimal for antibody imaging; this holds true for ^{86}Y with the slightly higher half-life of 14.7 h. One advantage of these two radioisotopes is the ability to predict dosimetry calculations for when the antibody of interest is radiolabeled with copper-67 (^{67}Cu) or yttrium-90 (^{90}Y) for radioimmunotherapy [71]. Superior to both these diagnostic radioisotopes is ^{89}Zr ($T_{1/2}$ = 78.4 h); it is well-suited to the pharmacokinetics of antibodies, permitting optimal tumour-to-background ratios. In addition, ^{89}Zr offers higher spatial resolution and the high-energy gammas (E_{max} = 909 keV) exceed the energy window making it an attractive isotope for clinical and preclinical use. Furthermore, ^{89}Zr can be produced using cyclotron at a low energy using highly abundant and relatively inexpensive starting material, yttrium-89.

1.5.1.2   Diagnostic Radioisotopes for Antibody Fragments, Mimetics and Peptides

Antibody fragment, mimetics and peptides are alternatives for antibody imaging with shorter biological half-lives and thus can be radiolabeled with shorter half-live radioisotopes. Gallium-68 (^{68}Ga, $T_{1/2}$ = 68.4 min), copper-61 (^{61}Cu, $T_{1/2}$ = 3.3 h), scandium-44 (^{44}Sc, $T_{1/2}$ = 3.97 h) and technetium (^{99m}Tc) are well suited to antibody fragment or affibody imaging [72, 73]. The pharmacokinetics of peptides is fast and thus also require short half-life radioisotopes; ^{18}F and ^{68}Ga are used extensively for peptide imaging. As described previously, ^{18}F is predominately

13

used for clinical oncology imaging due to the half-life and ideal decay properties for PET imaging. The well-established chemistry of ^{68}Ga allows for radiolabeling variety of compounds via chelators that have been conjugated to these compounds [74]. Radiolabeling with short half-lived isotopes requires fast and efficient labeling kinetics in conditions that are suited to the compound in question.

Table 1.2 Radioisotopes for PET or SPECT imaging. Adapted with permission from Holland et al. [66] and Price and Orvig [75].

Radioisotope	Half life	Decay mode	Mean positron range in water [mm]	Production route	E [keV]
^{11}C	20.38 m	β^+ (100%)	1.1	^{14}N(p,α)^{11}C	511
^{13}N	9.96 m	β^+ (100%)	1.5	^{16}O(p, α)^{13}N	511
^{15}O	122.4 s	β^+ (100%)	2.5	^{15}N(p,n)^{15}N	511
^{18}F	109.7 m	β^+ (100%)	0.6	^{18}O(p,n) ^{18}F	511
^{68}Ga	68 m	β^+ (90%) EC (10%)	2.9	^{68}Ge/^{68}Ga	511
^{86}Y	14.7 h	β^+ (33%) EC (66%)	2.5	^{86}Sr(p,n)^{86}Y	511, 1221
^{44}Sc	3.97 h	β^+ (94%) EC (6%)	2.5	^{44}Ti/^{44}Sc	511, 1474
^{61}Cu	3.3 h	β^+ (62%) EC (38%)	1.32	^{61}Ni(p,n)^{61}Cu	511, 1220, 1150
^{64}Cu	12.7 h	β^+ (90%) EC (41%) β^- (40%)	3.2	^{64}Ni(p,n)^{64}Cu ^{67}Zn(p,α) ^{64}Cu	511, 656
^{124}I	100 h	β^+ (68%)	3	^{124}Te(p,n)^{124}I	511, 603, 1691
^{99m}Tc	6.6 h	β^-	N/A	^{99}Mo/^{99m}Tc	140
^{89}Zr	78.4 h	β^+ (27%)	4.6	^{89}Y(p,n)^{89}Zr	511, 909
^{111}In	67.2 h	EC (100%)	N/A	^{111}Cd(p,n)^{111}In	170, 245

β^+ = positron decay, EC = electron capture, β^- = beta decay

1.6   Chelate and Radiolabeling Systems

The development of novel compounds and targeting molecules for cancer imaging is driving the demand to develop radioisotopes to suit the pharmacokinetics of the compounds and imaging acquisition requirements. Additionally, there is a demand for facile radiolabeling of these compounds in suitable (pH and temperature) conditions. Chelators are one avenue that provides a solution for facile radiolabeling of antibodies, fragments, mimetics or peptides. Covalently linked to the compound via reactive functional groups, the chelator is then radiolabeled with a suitable radioisotope to match the biological half life of the compound [76]. Price et al. discuss the challenges, advantages, constraints and stability of a variety of chelators and radiometals [75].

For antibody and antibody fragment radiolabeling, two important considerations for chelator choice must be respected: pH and temperature. The chelator should be able to complex the radiometal of choice in neutral or slightly neutral pH conditions and ideally at room temperature, or not exceeding 37°C. This requirement should also be considered for conjugation of the chelator to the antibody or fragment [77]. The conjugation of chelators directly to antibodies and like-structures requires an isothiocyanate or maleimide functional group on the chelator [78]. Typically, in basic conditions (pH 8.5-9.1), the chelator conjugates via the primary amines or thio groups of the antibody. After the incubation time of ~ 20 h at room temperature, unconjugated chelator is separated from the antibody with size exclusion separation either with molecular weight filters or PD-10 purification. The conjugated antibodies are ready to be radiolabeled and are typically stable up to two weeks at -20°C. The development of the bifunctional chelator diethylenetriaminepentaacetic acid (DTPA) provided an avenue for ^{111}In radiolabeling due to its 8 site coordination number. The isothiocyanate functionalized DTPA (p-SCN-Bn-DTPA) has been used extensively in preclinical and clinical antibody SPECT imaging [79]. It is conjugated efficiently to antibodies at pH ~8.9 and chelates ^{111}In in slightly acidic conditions (pH ~ 5.5) at room temperature. DTPA can also chelate with lutetium-177 (^{177}Lu) or ^{90}Y for antibody based therapy [80]. Due to the versatility of DTPA for both diagnostics and therapeutics many advances have been made to further improve its stability [81]. While DTPA covers antibody imaging with SPECT the development of the PET scanner offered the high-

resolution imaging properties and drove the demand for more suitable PET based radioisotopes for antibody imaging. As mentioned previously, ^{89}Zr is a suitable radioisotope for antibody PET imaging due to its half-life and decay properties. Considering the 8 coordination sites of ^{89}Zr, DTPA could be an obvious choice with ^{89}Zr bounding to the chelator through 3 nitrogen and 5 oxygen atoms. However, radiolabeling of DTPA with ^{89}Zr is extremely poor [82]. Desferrioxamine is currently the only commercially available chelator for ^{89}Zr. The addition of the bifunctional isothiocyanate group allows for successful conjugation of p-SCN-Bn-DFO (DFO) to protein based constructs [83]. It is well suited to mAb conjugation as it is easily conjugated to mAbs in slightly basic and low ionic conditions. Radiolabeling of ^{89}Zr to the conjugated-mAb is achievable in a low ionic and pH neutral reaction at room temperature [78, 84, 85].

1.7   Production Methods

1.7.1   Generators

Radionuclide generators have expanded the availability of a variety of radioisotopes to clinical centers without the need for an onsite accelerator. The first generator used for biological applications dates back to 1920; and the first commercial generator was developed at Brookhaven National Laboratory in the early 1960s; over the last 50 years has positively impacted nuclear medicine [86]. A radioisotope generator is essentially a radiochemical separation of the daughter radionuclide (desired isotope) that decays from the parent isotopes. Parent radionuclides are often obtained from uranium fission products; for example, molybdenum-99 (^{99}Mo). Alternatively, parent isotopes are produced directly in nuclear reactors or accelerators such as strontium-82 (^{82}Sr) or germanium-68 (^{68}Ge). The most widely used generator produced radioisotope in nuclear medicine is technetium-99m (^{99m}Tc) covering over 80% of diagnostic radiotracers. The development of the ^{99}Mo/^{99m}Tc generator in 1959 at Brookhaven National laboratories greatly advanced the use of this versatile radioisotope. ^{99m}Tc with a half-life of 6 h is eluted from the generator with saline and separated from the parent isotope, ^{99}Mo ($T_{1/2}$ = 66 h). It is used to radiolabel a variety of compounds including ^{99m}Tc-sestamibi for cardiac SPECT scans, ^{99m}Tc-medronic acid for bone scintigraphy and ^{99m}Tc-pertechnetate for thyroid tests. Over 95% of the ^{99}Mo used for generators is produced in nuclear

reactors via fission of uranium-235 (^{235}U) [87]. The five major reactors that produce most of the world's ^{99}Mo are over 40 years old and between 2007 and 2011 a multitude of planned and unplanned shutdowns caused disruption to the global distribution and availability of ^{99}Mo and consequently ^{99m}Tc. In Canada, the National Research Universal reactor that supplies over 30% of ^{99}Mo globally experienced several shutdowns due to leaks and is expected to completely shut down by 2018 [87]. Thus, there has been a dedicated investment into alternative methods for ^{99m}Tc production and in the past few years many advances have been made [88, 89]. Other clinically used generator produced radioisotopes include rubidium-82 (^{82}Rb) and gallium-68 (^{68}Ga) which are produced from ^{82}Sr/^{82}Rb and ^{68}Ge/^{68}Ga generators respectively. The positron emitting ^{82}Rb has a half-life of 76 s and is used for cardiac perfusion studies. The ^{82}Sr/^{82}Rb generator is eluted with saline and connected directly to a patient already positioned in a PET scanner [90]. Development of the ^{68}Ge/^{68}Ga generator led to the advancement of the first positron scintillation camera in the early 1960s [91]. These early ^{68}Ge/^{68}Ga generators retained the ^{68}Ge on aluminum oxide and eluted ^{68}Ga in the form of ^{68}Ga complexes with ethylenediaminetetraacetic acid [92]. Towards the end of the century ^{68}Ge/^{68}Ga generators were redesigned and commercialized; these new generators use a cationic elution method using titanium oxide or silicon oxide to elute the ^{68}Ga with low concentrations of hydrochloric acid [92]. The ^{68}Ga cation expanded the versatility of this PET radioisotope for facile labeling to compounds bound to chelators; DOTA being the most commonly used [78].

1.7.2   Cyclotrons

Cyclotrons are a type of particle accelerator that bombard particles with high energy onto a target material of choice to create a radioactive isotope. The energy at which a cyclotron can operate determines the type of reaction that can occur. Level I accelerators can obtain a maximum single proton or deuteron energy of 10 MeV. Level II accelerators can produce single or multiple protons and deuterons with a maximum energy of 20 MeV. Conventional clinical radioisotope production is serviced with level I or II cyclotrons. Level III accelerators have the capacity for single or multiple particles and operate at a maximum energy of 50 MeV. Higher energy beam accelerators range from 70 – 500 MeV; these are typically found in National laboratories [93].

The number of cyclotrons has increased over the years due to the increase in the number of PET facilities.

Charged particles, typically protons are accelerated with high radiofrequency (RF) alternating voltage between two electrodes, also known as dees (Figure 1.4). The RF oscillator alternates the charge on the individual dees causing the protons to accelerate. The dees are placed perpendicular to a magnetic field; this causes the accelerating particle to move in a circular path; moving in a spiral motion outward from the center. Protons or negative hydrogen ions are pulled from the ion source and are attracted towards a dee with an opposite charge. The dees reverse their potential when the particles are inside the dee gap. The particles are then attracted to the opposite dee and gain kinetic energy. The gain in energy forces a larger trajectory in the dee; the kinetic energy of the charge particle is governed by the radius, charge and mass of the particle and the magnetic field. The foil stripper strips two electrons from the charged particle to produce protons [7]. The energy of the internal beam is dependent on the radius and can be changed to fit production requirements.
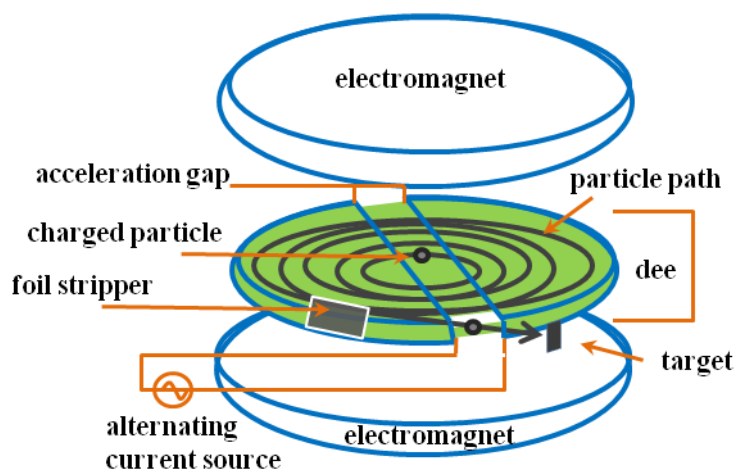
Figure 1.4 A schematic illustration of a cyclotron.

The energy of the accelerated particles required will depend on the starting material and the reaction required for producing the intended radioisotope [94, 95]. For example, to produce copper-64 (^{64}Cu) on a cyclotron either nickel-64, or zinc-67 can be used as starting material. Using beam energies of the following: 12 or 30 MeV for the respective starting materials ^{64}Cu

production is achievable [96-99]. The isotopic purity of the starting material will affect the overall yield and radionuclidic purity of the intended radioisotope [93]. Naturally abundant starting material sources such as yttrium-89 (^{89}Y) are available at greater than 99% isotopically purity. With appropriate beam energy, high yields of zirconium-89 (^{89}Zr) with high radionuclide and radiochemical purity is achievable from ^{89}Y. Naturally abundant starting material sources that are less pure will produce the intended radioisotope, but with lower radionuclide and radiochemical purity. When this happens, the final yield of the radioisotope will be lower and purification and separation from the other produced isotopes becomes a challenge. To alleviate this, isotopically enriched starting materials must be used. Depending on the availability of the source and the percentage of the isotopic contents a significant increase in cost can incur [100-102].

The starting material is held in a dedicated target holder and can be in a solid, liquid or gas state. Cyclotron production of radioisotopes used clinically (^{18}F, ^{15}O, ^{13}N and ^{11}C) is produced from either a liquid or gas starting material [7, 66]. As a result, most clinical cyclotrons are designed with a liquid target holder and transfer system. Traditionally, the production of radiometals developed for PET imaging are limited to generators or solid target stations on cyclotrons. The solid target approach offers the opportunity for high yield production to centres with the infrastructure to contain a separate solid target station. In addition to a separate solid target system, specialized equipment is required for prepping the starting material. Plating and electrodeposition techniques plate starting material onto a metal plate [99, 103, 104] and each group utilizes different plate dimensions, designed for their solid target parameters. As such, development and set up for routine production is limited to such centres. Additionally, solid target stations require specialized equipment to retrieve the irradiated target and transfer to the dedicated hot cell; this is also unique to the physical setup of the centre. Purification of the material and recycling of the target plates and material requires an integrated or adjacent radioactive chemistry lab. The physical requirements of solid target production are diverse and thus require on site personnel with specialized expertise. The requirements for solid target setup make it a challenge to implement a set up in existing cyclotron centres [105, 106].

The production of radiometals with a liquid target (LT) offers the opportunities for production in cyclotron centres that are only equipped with liquid target production. This could significantly expand the availability of these isotopes and accelerate preclinical and clinical development. Production yields of a wide range of radiometals with a liquid target have been reported previously [105, 107, 108]. High production yield was limited by concomitant gas formation and pressure increases during irradiation [108], as well as target density and target performance. Purification of ^{89}Zr with a LT uses the same procedures used for conventional solid target (ST) ^{89}Zr purification. Similar purification systems make the transition between ST and LT facile and can typically result in similar radiolabeling yields of mAbs. The production yield of ^{89}Zr LT is one factor that may not permit successful high specific activity of radiolabeled mAbs and may affect biodistribution or the ability to acquire PET images. LT production of radiometals is not limited to ^{89}Zr; developments for ^{68}Ga, ^{44}Sc, ^{86}Y production have been established in clinical cyclotrons [109]. Most notably, LT production of ^{89}Zr eliminates the need for solid target dissolution, making for a simpler post irradiation process. Purification of ^{68}Ga on the other hand is considerably different than that for generator ^{68}Ga. Most notably for ^{68}Ga is the lengthy purification time, a disadvantage when working with a short-lived radioisotope and the difficulties separating the ^{68}Ga from the staring material [104]. Advances in radiometal production via an LT system have demonstrated some improvements in yield; however, radiolabeling efficiency of the purified isotopes for pre-clinical immunoconjugate imaging has not been assessed.

1.8   Thesis Theme and Rationale

Antibodies are effective tools for targeted imaging. The long *in vivo* half life of antibodies is attributed to the interaction of the Fc portion of the antibody to the Fc receptor. This necessitates imaging acquisitions to take place several days post injection of the antibody for optimal tumour contrast. We explored different methodologies to enhance the clearance rate of antibodies by altering the interaction between the Fc domain and Fc receptor. The modulation of this interaction was studied in an established antibody/receptor system (Trastuzumab/HER2). We then proceeded to evaluate E-cadherin as a target for breast cancer diagnosis with radiolabeled antibodies.

The development of molecular antigen recognitions molecules (antibodies, antibody fragments, and peptides) targeting different cancer markers are paving the way for personalized medicine. These vectors often require non-conventional radioisotopes that match their biological half-lives and are suitable for imaging. Methods for facile production and purification of suitable radioisotopes exist; however, they either require a dedicated solid target system for cyclotron production or they are eluted from generators. We adapted current methods of conventional radioisotope production for two radiometals, ^{89}Zr and ^{68}Ga, using a liquid target system on a clinical system. This is expected to increase accessibility of these two isotopes for PET centers.

1.8.1   Objectives and Hypothesis

1) Tumour to non-target contrasts of radiolabeled antibodies can be enhanced by targeting the FcRn receptor.

2) E-cadherin is a promising diagnostic marker to image metastatic potential in breast cancer xenografts with PET or SPECT.

3) Zirconium-89 can be produced using a cyclotron liquid target system in sufficient yields and purity that will allow for sufficient radiolabeling of antibodies for PET imaging.

4) Efficient purification of cyclotron liquid target produced Gallium-68 can enable high radiolabeling yields of peptides for PET imaging.

Chapter 2: ^{111}In radiolabeling of Antibodies

2.1 Introduction

Monoclonal antibodies (mAb) are powerful tools used to characterize information regarding the characteristics or receptors of tumours. The use of radiolabeled immunoglobulins for targeting and cancer treatment emerged in the 1950s [68]. These mAbs will be conjugated with a chelator and radiolabeled with ^{111}In for μSPECT/CT imaging of mouse xenografts. Custom ordered milligram quantities of mAb are very expensive and to ensure conjugation, intact immunoreactivity, radiolabeling and imaging of the mAb, conditions were optimized using the clinical available Trastuzumab an anti-human epidermal growth factor 2 (HER2) receptor antibody. Manipulation of a mAb during conjugation with a chelator can affect the binding or can result in aggregation which has the potential to affect *in vivo* biodistribution. The conjugation of a chelator to a mAb requires a delicate balance of conjugating enough chelator to allow high radiolabeling yield and specific activity, but without compromising immunoreactivity.

The first part of this chapter focuses on ensuring methods for mAb conjugation, radiolabeling, immunoreactivity and μSPECT imaging for ^{111}In-Trastuzumab. As mentioned previously, the bifunctional chelator p-SCN-Bn-DTPA (DTPA) is an ideal candidate for radiolabeling mAbs with ^{111}In. It is used extensively for preclinical and clinical mAb imaging [70, 110, 111]. Conjugation of DTPA to mAbs is achieved at ambient temperatures and antibody acceptable basic pH conditions. Radiolabeling of the conjugated mAb with ^{111}In is achieved within 30 minutes with high radiochemical yield in low buffer concentrations and without the need for conventional heat. Developed initially, and tested with yttrium-90, a group of CHX-DTPA chelators were assessed for stability; the CHX-A"-DTPA chelator emerged as showing high serum stability both *in vitro* and *in vivo* [81]. The high stability of the CHX-A" was promising for therapeutic radioisotopes such as bismuth-213, yttrium-90 and lutetium-177 for radio immunotherapeutic applications [112, 113]. For imaging applications, the CHX-A" has been compared to the standard DTPA using ^{68}Ga and ^{64}Cu and to our knowledge *in vivo* studies

comparing tumour uptake and biodistribution of the CHX-A" to the DTPA using ^{111}In has not been published [44, 114]. A study comparing the effects of the amount of injected radiolabeled mAb on biodistribution and tumour uptake will be assessed using Trastuzumab conjugated with DTPA and radiolabeled with [111]In. In conjunction; a comparison of radiolabeling, immunoreactivity and *in vivo* biodistribution of tumour bearing mice injected with either ^{111}In-CHX-A"-DTPA-Trastuzumab or ^{111}In-DTPA-Trastuzumab.

The second part of this chapter compares strategies to increase the clearance rate of circulating radiolabeled antibodies for higher tumour to background ratio by exploiting the relationship between the Fc region of the circulating radiolabeled mAb and the neonatal Fc receptor (FcRn). Following injection of radiolabeled Trastuzumab, whole intact rabbit IgG or rabbit IgG Fc fragments were injected into the mice. The interaction of these compounds with the FcRn of the mouse should hinder the interaction of the circulating radiolabeled mAb with the FcRn; limiting the recirculation of radiolabeled mAb. Consequently, the circulating radiolabeled mAb will undergo degradation which should lead to an improved biodistribution and tumour contrast. To obtain high tumour-to-background contrast images of a radiolabeled mAb, image acquisitions need to occur several days post injection of the radiolabeled mAb. Interfering with the interaction of the FcRn and radiolabeled mAb by saturating the FcRn with an IgG may alter the biodistribution and pharmacokinetics of the radiolabeled mAb. This may in turn permit high tumour-to-background contrast at earlier time points, eliminating the need to acquire images several days post injection of the radiolabeled mAb. For this novel study, Trastuzumab was conjugated with the DTPA chelator and radiolabeled with [111]In.

The final part of the chapter examines the use of novel mAbs targeting the epithelial cell-cell adhesion molecule cadherin 1 (CDH1). It has been established that E-cadherin expression can aid in the diagnosis of invasive lobular carcinoma (ILC). Immunohistochemistry has been used to assess E-cadherin expression in breast cancer patients. Many breast cancers anarchically over express E-cadherin; the loss of E-cadherin expression or mutations in expression is linked to mesenchymal transition and propensity to metastasize to regional lymph nodes [29]. Exploiting these characteristics, E-cadherin can be used as potential target for breast cancer imaging and therapy. Breast cancer cells were screened for E-cadherin expression using three E-cadherin

mAb (anti-E-cad); these anti-E-cads will be radiolabeled with ^{111}In using the DTPA chelator and injected into mice xenograft bearing the selected E-cadherin positive breast cancer cells. μSPECT imaging and biodistribution assessed the efficacy of these anti-E-cads to detect E-cadherin expression. Breast cancer cells were screened for E-cadherin expression using three E-cadherin mAb (anti-E-cad). These anti-E-cads will be radiolabeled with ^{111}In using the DTPA chelator and injected into mice xenograft bearing the selected E-cadherin positive breast cancer cells. μSPECT imaging and biodistribution assessed the efficacy of these anti-E-cads to detect E-cadherin expression.

2.2   Materials and Methods

Trastuzumab was purchased as Herceptin from Genentech (San Francisco, CA) Monoclonal E-cadherin antibodies were chosen for their reactivity to both mouse and human; rabbit host clone 24E10 from Cell Signaling (Beverly, MA), rabbit host clone EP700Y from abcam (Cambridge, UK) and rat host clone DECMA-1 from eBioscience (San Diego, USA) and were custom ordered free of excipients. Rabbit monoclonal IgG isotype control, clone EPR25A was purchased from abcam (Cambridge, UK). Goat anti-rabbit secondary IgG with 488 flurochrome was purchased from Invitrogen (Waltham, USA). Rabbit IgG protein A Purified Low Endotoxin (Innovative Research, Novi, MI, USA) and ChomPure Rabbit IgG, Fc fragment (Jackson Immuno Research Laboratories, West Grove PA, USA) were purchased for studies involving the FcRn.   Chelators pSCN-Bn-DTPA or pSCN-Bn-CHX-A"-DTPA were purchased from Macrocyclics (Dallas, TX, USA). ^{111}In was purchased from Nordion (Ottawa or Vancouver, Canada) as [^{111}In]InCl$_3$. Purification and quality control of antibody conjugates and radiotracers were performed on an Agilent (Santa Clara, CA) HPLC system equipped with a model 1200 quaternary pump, a model 1200 UV absorbance detector, and a Bioscan (Washington, DC) NaI scintillation detector with a size exclusion column (SEC) (Phenomenex, 5 µm SEC-s3000, 300 × 7.8 mm). Radioactivity of tracers were measured using a Capintec (Ramsey, NJ) CRC$^{®}$-25R/W dose calibrator. The radioactivity of mouse tissues collected from biodistribution studies were counted using a Perkin Elmer (Waltham, MA) Wizard2 2480 automatic gamma counter.

2.2.1 Flow Cytometry Analysis for E-Cadherin Antibody Candidate

Cells (1.0E5 per well) were seeded in a V-bottom 96-well polystyrene plate and washed twice in 200 µl of FACS buffer (PBS + 2% FBS + 0.02% NaN_3). Cells were then incubated for 30 min on ice and in dark with 100 µL of FACS buffer or the DECMA-1, 24E10 or EP700Y primary antibodies (2.5 µg/mL in FACS buffer). 80 µL of FACS buffer were added to the reaction and cells were then washed twice with 200 µL of FACS buffer. Cells that were incubated with the Fluor 488 conjugated antibody were ready for flow cytometry at this time. For the rabbit IgG and rat IgG antibodies, secondary anti-rat and goat anti-rabbit both with 488 flurochrome were diluted to a concentration of 2.5 µg/ml in FACS buffer. 100 uL were added to the respective reactions and incubated in the dark for 30 minutes on ice. 80 µl FACS buffer were added to the reaction and cells were washed twice with 200 µL of FACS buffer. Cells were screened in a FACSCalibur analyzer (BD Biosciences), using the blue excitation laser (488 nm, emission 530/30nmBP). Data were acquired with BD CellQuest™ Pro software. Flow cytometry data were analyzed using FLOWJO™ software.

This procedure was repeated for cells from tumours from mice bearing MCF, T47D or MDA-MB-231 tumours (refer to section 2.2.7 for xenograft preparation of E-cadherin positive tumours). Once tumours reached at approximately 100 mm^3 the mice were euthanized using CO_2 asphyxiation; tumours were harvested and transferred into 5 mL of media (Dulbecco's Modified Eagle Medium: Nutrient Mixture F-12) with 5% FBS and 2X concentration of human collagenase / hyaluronidase = 200 µl for 1 mL medium; and 1% P/S antibiotics). The tumours were incubated at 37°C for 2 h and vortexed every 20 min and subsequently centrifuged at 1200 rpm, 5 min at 4°C; the supernatant was discarded. Trypsin was added to dissociate cells into a single suspension and then centrifuged as described above with Hanks Balanced Salt Solution and supernatant discarded. Dispase + DNAse (5 mL) was added to prevent clumping of cells before being passed through a 40 µm cell strainer. The cells were then centrifuged and supernatant discarded. Cells were prepped as above for FACS analysis. At the time of this analysis controls were run using either: unstained cells for the DECMA-1, cells stained with rabbit isotype control IgG conjugated with 488 for 24E10 or cells stained with secondary antibody only for EP700Y.

2.2.2   Immunohistochemistry

To validate E-cadherin expression, histological tissue analysis of MCF7, T47D and MDA-MB-231 tumours was performed. Tumours were harvested and fixed in 4% paraformaldehyde in PBS for 48 h at room temperature. After dehydration, tissues were embedded in paraffin and 4 µm sections were mounted onto Superfrost plus slides (Fisherbrand, Ottawa, Canada). Immunostaining was performed by Histology Services at the BC Cancer Agency using the Ventana Discovery XT instrument (Ventana Medical Systems Inc, Tucson, USA). Slides were incubated with the three E-cadherin antibodies for 1 h without heat at dilutions of 1/100 with signal stain for 24E10 and 1/000 for EP700Y and EPR25A in a cell conditioning solution antigen retrieval buffer. Subsequently a Ventana Discovery UltraMap anti-Rb HRP was added to the samples and incubated 16 minutes. Immunodetection was analysed using the Discovery ChromoMap DAB kit (Ventana) and counterstained with Leica SelecTech hematoxylin and bluing reagent (Leica Biosystems, Concord, Ontario, Canada). The stained sections were examined and analysed with a Leica DM 2500 light microscope.

2.2.3   Conjugation of *p*-SCN-Bn-DTPA or *p*-SCN-Bn-CHX-A"-DTPA to mAbs

Trastuzumab was purified to remove α,α-treholase dehydrate, L-, and polysorbate 20 additives using centrifugal filter units with a 50 kDa molecular weight filter (Amicon, Millipore, Darmstadt, Germany) and washed with PBS (pH 7.4, 15 mL) at 4000 g for 20 min four times. 1 mg was then conjugated with either *p*-SCN-Bn-DTPA or *p*-SCN-Bn-CHX-A"-DTPA in PBS (buffered to pH 8.9 with 0.1 M Na_2CO_3). A 5:1 molar ratio of chelator to mAb with a minimum concentration of mAb of 2 mg/mL was used. The reactions were incubated overnight at room temperature with gentle agitation. The reaction was purified using 50 kDa Amicon filters to remove any unconjugated chelator. DTPA-Trastuzumab conjugates were washed twice with PBS before being resuspended in 0.15 M ammonium acetate (pH 5.5). For each E-cad mAb, 50 µg per mouse was conjugated with *p*-SCN-Bn-DTPA in PBS with the same procedure.

2.2.4 Isotopic Dilution and Number of Chelates

The number of accessible chelating ligands conjugated per antibody was determined using previously described methods [115, 116] A working solution of non-radioactive In^{3+} spiked with ^{111}In was prepared with a final In^{3+} concentration of 500 µM in ammonium acetate buffer (0.15 M, pH 6) with 37 kBq/µL of $[^{111}In]InCl_3$. In duplicate, for each DTPA-Trastuzumab or CHX-A"-Trastuzumab, 50 µg of bioconjugate (30 µL) was prepared into separate 1.5 mL Eppendorf tubes. Aliquots of 20, 25, and 30 µL of the $[^{111}In]InCl_3$ solution were added to the two chelate-antibody samples. Positive controls containing 50 µg of bioconjugate and 25 µL of buffered [111]InCl_3 only (no non-radioactive In^{3+} added) were prepared in duplicate. Negative controls containing 30 µL of PBS, and 25 µL of $[^{111}In]InCl_3$ working solution were prepared in duplicate. Samples were allowed to incubate at room temperature overnight, after which time EDTA (50 mM, pH 5) was added at 1/9 of the reaction volume to scavenge any unspecifically bound In^{3+}, and incubated for 15 min. Each reaction mixture was spotted onto iTLC-SG plates, and developed using EDTA (50 mM, pH 5) as mobile phase. Strips were cut in half, each placed separately in test tubes, and counted on the calibrated gamma counter to determine the extent of radiolabeling. The average number of chelates per mol of antibody was calculated by dividing the cpm of the bound [111]In (Rf =0) by the cpm of the unbound [111]In (Rf >0.5) and multiplying that by the number of moles (n) of free In^{3+} divided by moles of conjugated-Trastuzumab.

2.2.5 Immunoreactivity Fractions

Immunoreactivity fractions of radiolabeled Trastuzumab with ^{111}In was determined according to the Lindmo cell-binding assay. HER2-positive SKOV-3 cells were suspended at different concentrations (0.4 to 4.5 x 10^6 cells/mL in PBS). ^{111}In-DTPA-Trastuzumab or ^{111}In-CHX-A" Trastuzumab (50 µL diluted in 1% PBS-BSA at 0.5 MBq/mL) were added to each tube in triplicates. After 1 h incubation at ambient temperature and under gently agitation, cells were centrifuged and washed twice with PBS. The binding and unbound fractions of the radiolabeled antibodies were determined for each sample using a gamma counter (with background and decay correction). Immunoreactive fractions were estimated by linear regression analysis of total/bound activity against 1/[cell concentration].

2.2.6 ^{111}In Radiolabeling of *p*-SCN-Bn-DTPA and *p*-SCN-Bn-CHX-A" -mAbs

^{111}In in a chloride saline solution (20 – 40 MBq per mouse) was added to conjugated-mAb, 50 µg per mouse and left to react at room temperature for 60 min. Radiochemical efficiency was assessed by iTLC and SEC HPLC. The ^{111}In-DTPA-mAb or ^{111}In-CHX-A"-DTPA-mAb were then purified via PD-10 columns in PBS followed by purification with centrifugal filter units (50 kDa). The final product was collected in 0.9% saline and radiochemical purity and specific activity were determined by SEC HPLC.

2.2.7 Xenograft Preparation of HER2 Positive and E-Cadherin Positive Tumours.

All animal experiments were performed at the Animal Resource Centre of the BC Cancer Agency Research Centre in accordance with the institutional guidelines of the University of British Columbia Animal Care Committee (Vancouver, BC, Canada) and under the supervision of authorized investigators.

Female immunodeficient NOD.Cg-*Prkdc^{scid}Il2rg^{tm1Wjl}*/SzJ (NSG) mice (obtained from our in-house breeding colony at the Animal Resource Centre at BC Cancer Research Facility) were used in all imaging and biodistribution experiments. For the radiolabeling of Trastuzumab, mice were subcutaneously injected with 8 x 10^6 SKOV-3 cells in a 50:50 mixture of PBS and basement membrane matrigel (BD science).   For E-cadherin studies, the mice were subcutaneously implanted with a 17β-estradiol pellet (Innovative Research of America). Seven days later the mice were subcutaneously injected with 6 x 10^6 MC7 or T47D cells as stated above. Mice that were inoculated with MDA-MB-231 cells did not require the use of an estrogen pellet.

2.2.8 µSPECT/CT Imaging

Tumour bearing mice were sedated with 2% isoflurane (in O$_2$) by inhalation and injected intravenously with the radiolabeled mAb. Two weeks post cell implantation the SKOV-3 cells, mice were injected with the radiolabeled Trastuzumab. To assess the effect on the amount of antibody injected, mice were either injected with 10.4 ±0.4 µg (3.67 ± 0.2 MBq) or 30.5 ±1.4 µg (10.76 ± 0.5 MBq) of ^{111}In-DTPA-Trastuzumab. To compare the CHX-A" and DTPA chelators,

mice were injected with similar amounts of radiolabeled antibody with ^{111}In-DTPA-Trastuzumab (45.24 ± 5.53 µg) or ^{111}In-CHX-A"-Trastuzumab (51.43 ± 3.32 µg). For the FcRn study, all mice were injected with equal amounts of radiolabeled ^{111}In-DTPA-Trastuzumab. Mice were then grouped, and received either 6.6 nmol of rabbit IgG or Fc rabbit IgG fragments or saline 8 h post injection of ^{111}In-DTPA-Trastuzumab. Five-six weeks after cell implantation the mice were injected via intravenous tail vein injection with ^{111}In-DTPA-E-cadherin (24E10, EP700Y or DEMCA-1) or ^{111}In-DTPA-rabbit isotype control (EPR25A). µSPECT/CT images were acquired on a U-SPECT-II scanner (MILabs, Utrecht, Netherlands). Mice were sedated and placed on the scanner bed; body temperature was maintained with the use of a heating pad. A baseline CT acquisition was obtained for localization prior to every µSPECT acquisition with a voltage setting of 60 kV and current of 615 µA. A single static emission scan was acquired for 1 h using an ultra-high-resolution multi-pinhole rat (1 mm pinhole size) collimator. Data were acquired in list mode acquisition, reconstructed using the U-SPECT II software, and co-registered for alignment. The SPECT images were reconstructed using maximum-likelihood expectation maximization (3 iterations), pixel-based ordered subset expectation maximization (16 subsets) and a post-processing filter (Gaussian blurring) of 0.5 mm centered at photopeaks 171 keV and 245 keV with a 20% window width. Imaging files were visualized with either PMOD or Inveon Research Workplace software. µSPECT/CT images were acquired at 1, 3 and 5 days post injection for DTPA chelator studies, 1 day post injection for FcRn studies and 1, 3 and 5 days post injection for the E-cadherin studies.

2.2.9 Biodistribution Studies

Tumour bearing mice were injected intravenously with the radiolabeled mAb. At the desired time point, mice were euthanized by CO_2 asphyxiation. Blood was withdrawn, and organs/tissues of interest were harvested, rinsed with saline, blotted dry and weighed. Radioactivity in collected tissues was counted on a calibrated gamma counter, normalized to the injected dose and expressed as the percentage of the injected dose per gram of tissue (%ID/g). Biodistribution was conducted at day 5 post injection for effects on antibody amount, days 1, 3 and 5 for DTPA chelator studies, 1 day post injection for FcRn studies and day 3 and 5 for E-cadherin studies. Statistical analyses for biodistribution data were performed using GraphPad

Prism (version 7). *P* values were calculated using ANOVA and valued < 0.05 were considered statistically significant.

2.3 Results and Discussion

2.3.1 Effects of Amount of Injected Antibody

Images of the mice in the DTPA-30 group at day 1 demonstrated typical mAb distribution (tumour, liver and spleen uptake); due to the low injected activity in the DTPA-10 group images were not acquired. Statistically no differences were found between the biodistribution data of organs of each group at day 5 post injection. A trend of higher absolute uptake in blood, kidney, heart, muscle and tumour in the DTPA-30 group compared to DTPA-10 (Figure 2.1) was observed. A reverse trend was observed with spleen and liver uptake; both demonstrating a trend for higher uptake in the DTPA-10 group. Unlike small molecules and peptides where the effect of mass can affect tumour uptake, the uptake of antibodies is not affected as much. Injecting increasing doses of peptide will cause a blocking effect in the tumour. The major effect that is observed with varying the injected dose of antibodies is observed in the liver and spleen. Normal physiological characteristics of the spleen, liver and bone marrow make them a homing site for antibodies due to the many sinusoidal clefts present in these organs [117]. A high percentage of the injected dose of radiolabeled antibody is therefore expected in the spleen and liver. The liver is a site of antibody metabolism and a potential site for intact and non-intact antibodies; most commonly in the form of ^{111}In-ferritin, ^{111}In-intact antibody and ^{111}In-low molecular weight fractions [118]. Trends of increased uptake with decreased injected antibody dose have been presented with the use of ^{64}Cu-labeled amatuximab; a decrease in injected amatuximab resulted in a significant increase in liver uptake, with the spleen following a similar trend [119]. The involvement of the FcRn plays an integral role in antibody excretion and recirculation especially in the spleen and liver [120]. The higher blood and heart uptake observed in the DTPA-30 group may be a result of the involvement of the interaction between the circulating ^{111}In-DTPA-Trastuzumab and the FcRn. Increasing the amount of injected antibody may contribute to a saturation of Fc receptors in the liver. This saturation may limit the amount of antibody degraded by the liver resulting in lower liver percentage of the injected antibody in the DTPA-30 group. Due to the potential reduced percentage antibody degradation

in the liver, there is more intact antibody available for circulation; and this may contribute to the higher blood and heart uptake in the DTPA-30 group. Keeping the antibody in circulation increases the bioavailability and consequently increases tumour uptake; evident with the higher tumour uptake in the DTPA-30 group.
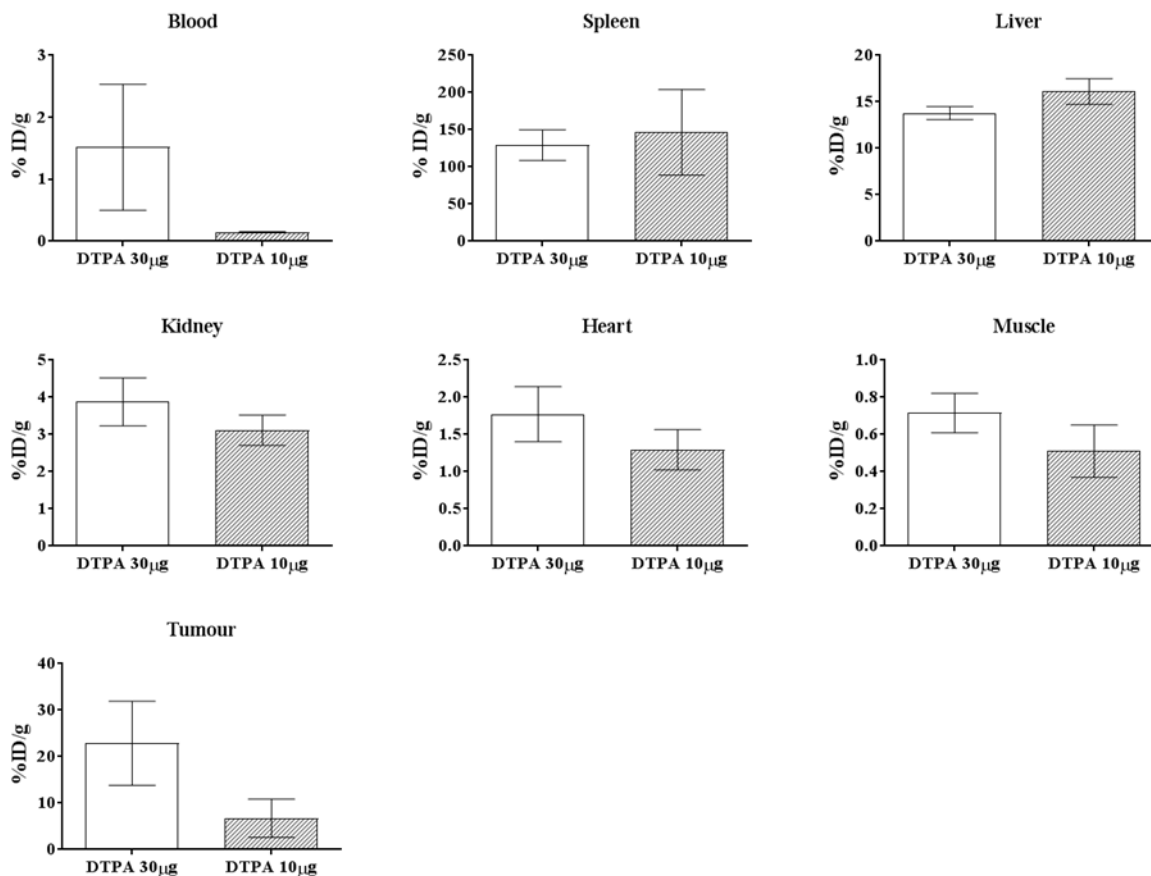
Figure 2.1 Tumour and organs of interest uptake at day 5 to assess effects of amount of injected antibody. Graphs are displayed as a percentage of injected dose per gram of tissue (%ID/g).

When assessing ratio of uptake in tumour to non-tumour organs, the DTPA-30 exhibited a trend of higher tumour to spleen, liver, kidney, heart and muscle in comparison to the DTPA-10. Tumour to blood ratio is slightly higher with the DPTA-10 group, however the large standard deviation in the DTPA-30 group renders any possible differences obsolete; a trend might emerge with a greater number of subjects (Figure 2.2). The demonstration of the effect of injected

antibody is important for optimizing and assessing novel antibodies for imaging and potentially therapy.
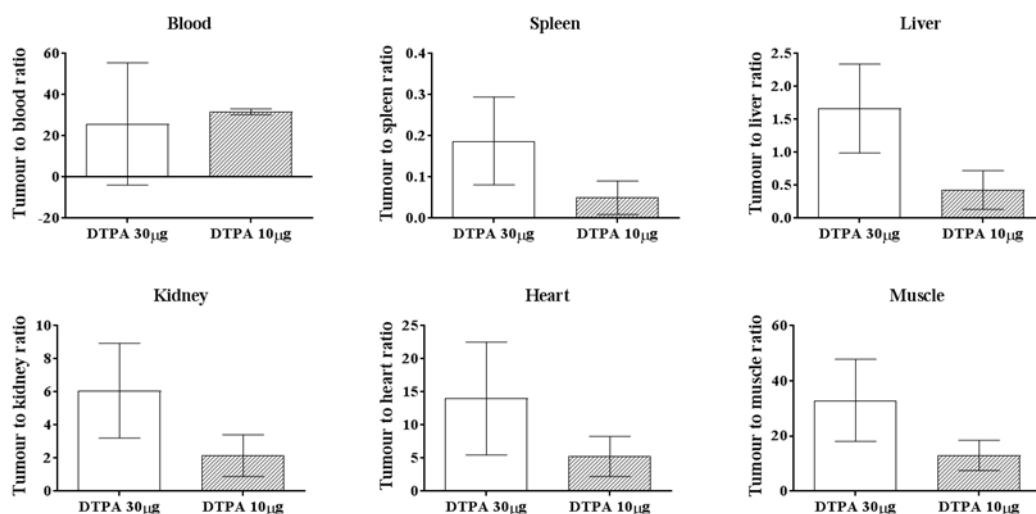
Figure 2.2 Tumour to organ of interest ratio to assess effects of amount of injected antibody. Graphs are displayed as a ratio of tumour %ID/g to organ of interest %ID/g.

2.3.2   Comparison of Two Chelators for [111]In Antibody Radiolabeling

The conjugated and purified *p*SCN-Bn-DTPA-Trastuzumab (DTPA-Trastuzumab) or *p*SCN-Bn-CHX-A"-DTPA-Trastuzumab (CHX-A"-Trastuzumab) demonstrated no aggregation; evident by SEC HPLC analysis (data not shown).   Isotopic dilution analysis determined a chelate to antibody ratio of 4.7 ± 0.6 for the DTPA-Trastuzumab and 4.6 ± 0.7 for CHX-A"-Trastuzumab. Radiolabeling efficiency of greater than 90% was confirmed by iTLC for both conjugates. SEC HPLC analyses confirmed specific activities: DTPA-Trastuzumab (0.88 MBq/µg) and CHX-A"-Trastuzumab (0.77 MBq/µg); with radiochemical purity of greater than 99% for both compounds.   Immunoreactivity fraction was determined as DTPA-Trastuzumab: 70.7% and CHX-A"-Trastuzumab: 99 %; which were satisfactory for *in vivo* studies.

To compare biodistribution of the two chelators mice were injected with approximately equal amount of radiolabeled mAb, the ^{111}In-DTPA-Trastuzumab group (which will be referred to as DTPA) received 45.24 ± 5.53 µg while the ^{111}In-CHX-A"-Trastuzumab group (which will be

32

referred to as CHX-A") received 51.43 ± 3.32 µg of mAb. µSPECT/CT imaging at day 1 showed high uptake in the tumour, heart, spleen and liver (Figure 2.3). Over the course of 5 days, both radiolabeled conjugates exhibited typical antibody pharmacokinetics with clearance by day 5 giving rise to a high tumour to background contrast.
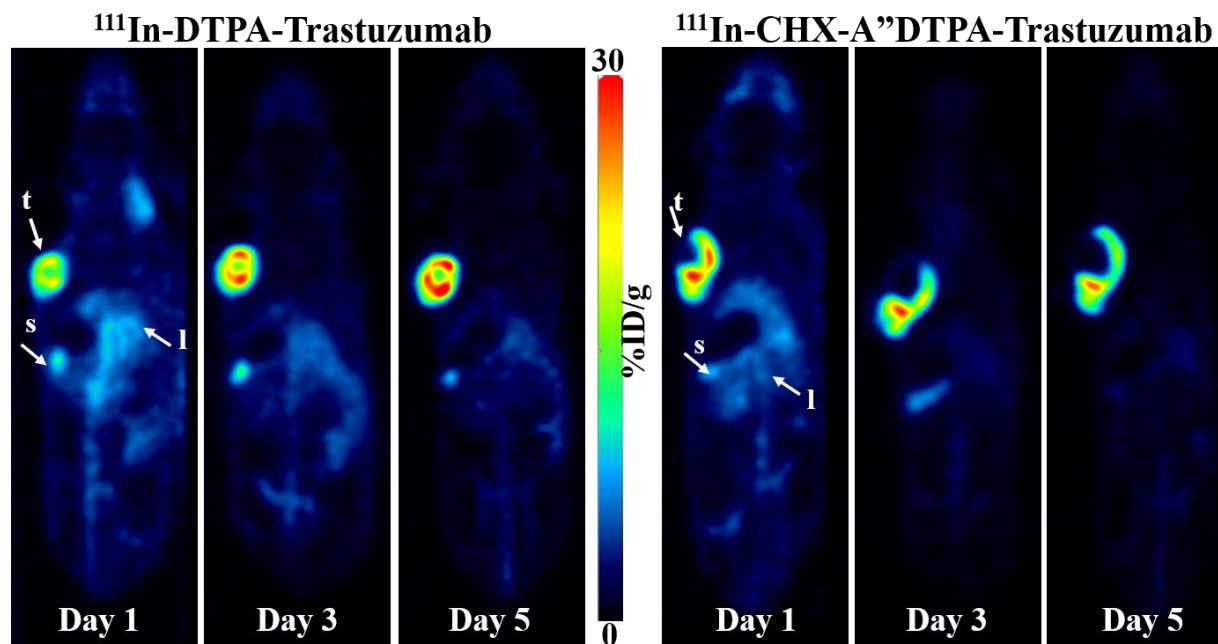
Figure 2.3 Representative µSPECT images through the middle of the tumour (t) at day 1, 3 and 5 of mice injected with Trastuzumab conjugated to DTPA or CHX-A"-DTPA. At day one uptake is visible in the tumour (t), spleen (s) and liver (l). The scale bar provides a qualitative max and min intensity decay corrected to injection time.

Biodistribution data (Table 2.1) showed no differences with uptake in the tumour or organs of interest (spleen, liver, heart, muscle, kidney or blood) at day 1. Within each group, tumour uptake between day 1 and 3 did not differ, although a slight increase was noted at day 3 (Figure 2.4). There was significant increase in tumour uptake from day 1 to 5 within the groups ($p = 0.0045$ DTPA and $p < 0.0001$ CHX-A"). In general, the CHX-A" had slightly higher absolute tumour uptake than the DTPA and at day 3 this difference was significantly significant ($p < 0.05$); however, by day 5 this significant difference was no longer present. The spleen was the only organ of interest to demonstrate a difference at days 3 and 5 compared to day 1 within each

group respectively. The spleen uptake increased from day 1 to 3 ($p < 0.0001$) for both groups and then decreased at day 5 with respect to day 3. There was significantly higher uptake in spleen with the DTPA group compared to CHX-A" at day 3 ($p = 0.0083$) and day 5 ($p = 0.0025$). Considering the two groups were injected with similar amounts of antibody, it is unclear what caused this difference or whether this is simply due to biological or batch-to-batch variability. The stability of the CHX-A"-Trastuzumab may be a contributor to the differences in spleen uptake, however, bone uptake was similar between the two groups.

However, when taking into consideration the tumour to spleen ratios did not differ between the two groups at any time point. This relationship was the same for the tumour to blood, heart, kidney, liver and muscle ratios. It is evident that overall, the biodistribution of p-SCN-Bn-CHX-A" conjugated to Trastuzumab was relatively similar to that of the standard p-SCN-Bn-DPTA conjugated with Trastuzumab. While not performed in this study, the CHX-A" chelators demonstrated high serum stability of ^{64}Cu labeled ritiximab, outperforming the DTPA [114]. However, ^{64}Cu is not well suited for DTPA and as such, the better suited ^{111}In is a more appropriate radiometal to test the stability and performance of the CHX-A" [75]. Based on biodistribution data, the CHX-A" performed as well as DTPA, however with an improved and decreased spleen uptake, which may be advantageous for antibodies conjugated with CHX-A" for ^{177}Lu or ^{90}Y radioimmunotherapy.

Table 2.1 Biodistribution for ^{111}In-pSCN-Bn-DTPA-Trastuzumab and ^{111}In-pSCN-Bn-CHX-A"-DTPA-Trastuzumab at day 1, 3 and 5 post injection. Data is presented as mean ± SD, %ID/g. Significant differences between ^{111}In-pSCN-Bn-DTPA-Trastuzumab and ^{111}In-pSCN-Bn-CHX-A"-DTPA-Trastuzumab at the respective time point are highlighted by stars (* $p < 0.05$, ** $p < 0.001$).

	^{111}In-DTPA-Trastuzumab			^{111}In-CHX-A"-Trastuzumab		
	Day 1	Day 3	Day 5	Day 1	Day 3	Day 5
N of mice	N = 3	N = 3	N = 4	N = 4	N = 4	N = 4
Dose (MBq)	40 ± 4.89			39.58 ± 2.54		
mAb (μg)	45.24 ± 5.53			51.43 ± 3.32		
Blood	16.47 ± 1.18	9.37 ± 1.71	2.68 ± 1.65	17.01 ± 1.53	10.87 ± 1.81	4.17 ± 1.24
Fat	0.7 ± 0.05	0.73 ± 0.26	0.65 ± 0.31	0.62 ± 0.08	0.6 ± 0.25	0.48 ± 0.14 *
Uterus	12.89 ± 0.68	14.53 ± 3.78	22.13 ± 20.93	15.44 ± 3.2	13.92 ± 1.92	10.67 ± 1.54
Ovaries	9.87 ± 0.89	10.1 ± 0.54	6.99 ± 8.10	9.98 ± 0.94	10.69 ± 1.20	7.5 ± 2.58
Intestine	3.73 ± 0.24	5.26 ± 0.64	4.12 ± 0.21	3.68 ± 0.55	5.55 ± 0.13	4.39 ± 0.34
Spleen	27.32 ± 3.97	69.82 ± 20.9	63.96 ± 26.52	25.6 ± 1.06	55.76 ± 3.84 **	49.65 ± 6.79 **
Liver	8.12 ± 0.48	5.98 ± 0.39	4.89 ± 0.46	8.88 ± 1.03	6.89 ± 0.76	5.15 ± 0.26
Pancreas	3.98 ± 4.20	1.4 ± 0.47	1.02 ± 0.09	1.51 ± 0.17	1.54 ± 0.19	0.97 ± 0.21
Stomach	2.75 ± 0.07	2.61 ± 0.24	1.87 ± 0.12	2.99 ± 0.35	2.74 ± 0.26	2.05 ± 0.27
Adrenals	3.52 ± 0.67	2.93 ± 1.07	1.39 ± 0.35	3.78 ± 1.06	3.04 ± 0.98	1.51 ± 0.52
Kidney	6.1 ± 0.55	4.32 ± 0.72	2.18 ± 0.13	5.01 ± 0.33	3.51 ± 0.34	2.03 ± 0.19
Lungs	7.33 ± 0.64	5.03 ± 0.81	2.92 ± 0.64	7.25 ± 0.63	5.4 ± 1.23	3.34 ± 0.68
Heart	4.11 ± 0.07	2.28 ± 0.44	1.04 ± 0.24	4.71 ± 0.36	2.9 ± 0.57	1.37 ± 0.38
Muscle	1.2 ± 0.17	0.82 ± 0.31	0.69 ± 0.37	0.93 ± 0.11	0.99 ± 0.18	0.44 ± 0.10
Bone	3.54 ± 0.82	4.07 ± 1.04	3.86 ± 0.42	4.03 ± 0.21	4.24 ± 0.39	2.9 ± 0.43
Brain	0.36 ± 0.00	0.26 ± 0.03	0.14 ± 0.03	0.32 ± 0.05	0.3 ± 0.03	0.15 ± 0.04
Tail	3.06 ± 0.15	2.5 ± 0.53	1.68 ± 0.22	3.38 ± 0.27	2.46 ± 0.42	1.63 ± 0.11
Tumour	36.45 ± 5.61	39.06 ± 5.36	51.23 ± 14.07	41.76 ± 17.94	51.01 ± 7.6 *	59.14 ± 7.70
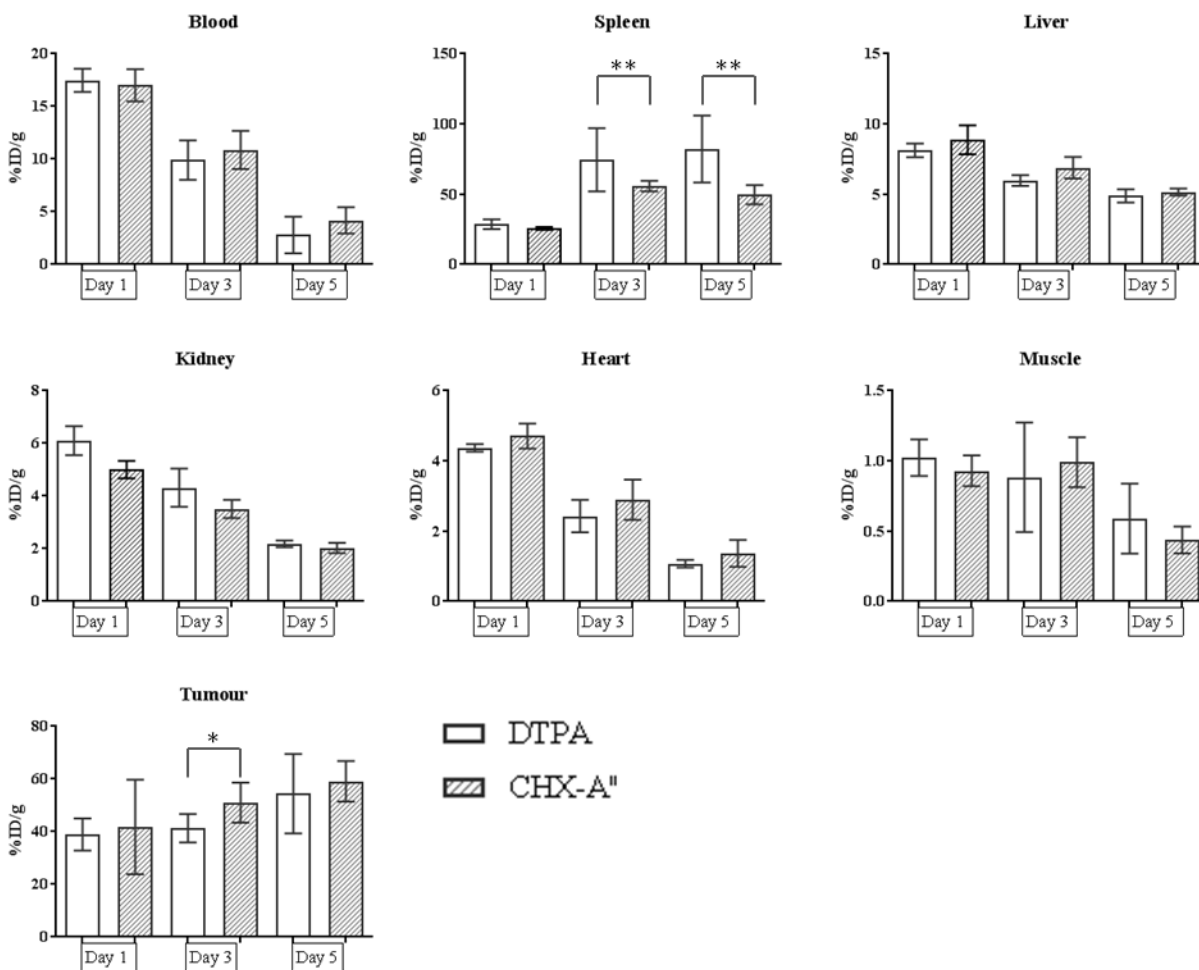
Figure 2.4 Tumour and organ of interest uptake comparing Trastuzumab conjugated to DTPA or CHX-A"-DTPA. Graphs are displayed as absolute uptake expressed as %ID/g at day 1, 3 or 5 post injection of ^{111}In-pSCN-Bn-DTPA-Trastuzumab or ^{111}In-pSCN-Bn-CHX-A"-DTPA-Trastuzumab. Significant differences between ^{111}In-pSCN-Bn-DTPA-Trastuzumab and ^{111}In-pSCN-Bn-CHX-A"-DTPA-Trastuzumab at the respective time point are highlighted by stars (* $p < 0.05$, ** $p < 0.001$)

2.3.3   FcRn Saturation to Improve Tumour to Background Ratios

To improve imaging of mAb, especially tumour to background ratios, by increasing the elimination rate, studies were performed by saturating the FcRn receptor. To this aim, we

36

compared the biodistribution and tumour ratios of mice injected with ^{111}In-DTPA-Trastuzumab at time zero, followed with an injection of saline (control), intact rabbit IgG or Fc fragments from rabbit IgG, 8 h following the initial ^{111}In-DTPA-Trastuzumab. The 8 h time point permitted normal circulation of ^{111}In-DTPA-Trastuzumab allowing for tumour uptake. For Rabbit IgG was chosen as the method for saturating the mouse FcRn as it has the highest binding affinity to mouse FcRn compared to mice (about 6x better affinity) and other rodent or human IgG [121].

For all groups, µSPECT images acquired at 24 hours showed typical antibody distribution, evident with tumour, spleen and liver uptake (Figure 2.5). There was visible heart uptake in the IgG and Fc groups at 24 hours compared to the control. This would suggest higher blood uptake as compared to control. The IgG group appeared to have higher blood uptake and less tumour contrast in comparison to the control group. Tumour uptake in the representative mouse of the Fc group appeared to be substantially higher than control and IgG groups. For absolute data for the uptake, quantification biodistribution data was analyzed. The biodistribution data (Figure 2.2), showed no significantly differences in the uptake of ^{111}In-DPTA-Trastuzumab in the antibody organs of interest (kidney, liver, heart, muscle). There was a significantly higher uptake in the blood of the IgG group (17.95 ± 2.04 %ID/g) compared to control (8.23 ± 2.02 %ID/g), ($p < 0.0001$). This was quite unexpected as the in similar studies the blood uptake in mice injected with IgG trended lower than controls but this did not reach statistical significance [122]. The spleen uptake in the control group (51.43 ± 12.11 %ID/g) was significantly higher than the Fc group (18.54 ± 5.29 %ID/g, p = 0.0075) and IgG (45.26 ± 8.30 %ID/g, p < 0.001). The IgG even was significantly lower than the Fc (p <0.001); we can speculate that a sizable percentage of the spleen may have been taken up with the Rabbit IgG minimizing uptake of Trastuzumab. This technique may be of use for therapy where high uptake of a therapeutic radioimmunoconjugate is evident in the spleen. No differences were evident with muscle or tumour uptake among the three groups.
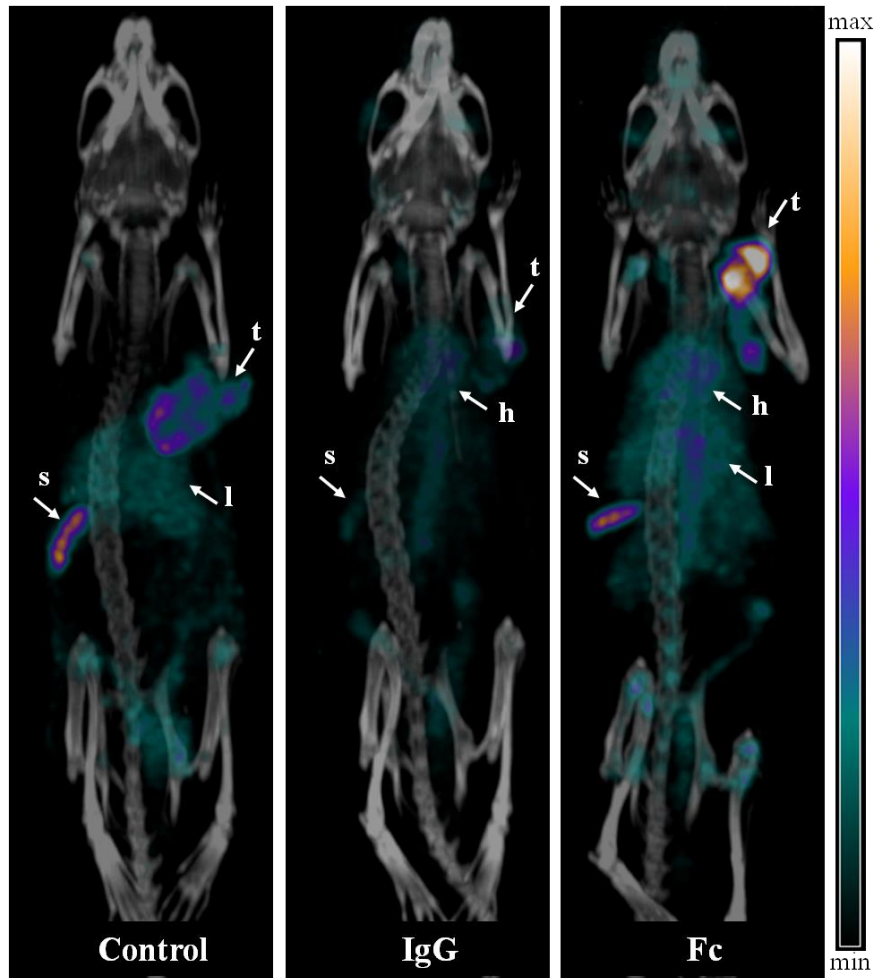
Figure 2.5 µSPECT images of ^{111}In-Trastuzumab in control, rabbit IgG chaser and rabbit Fc chaser groups at 24 h. There is visible uptake in the tumour (t) in all groups with high uptake in the spleen (s) and liver (l) in the Control and Fc group. Visible uptake in the heart (h) is evident in the IgG chaser and Fc groups.

Table 2.2 Biodistribution of tumour and non-tumour organs for ^{111}In-pSCN-Bn-DTPA-Trastuzumab uptake at 24 h post injection. Groups were separated into mice injected with saline (control) Rabbit IgG or Rabbit Fc 8 hours post injected. Data is presented as mean ± SD, %ID/g. Significant differences are highlighted by stars (* $p < 0.05$, ** $p < 0.0001$)), number of mice ≥ 4 compared to control.

^{111}In-DTPA-Trastuzumab	Control	IgG	Fc
Blood	8.23 ± 2.02	17.95 ± 2.04 **	12.95 ± 1.96
Fat	0.77 ± 0.28	1.06 ± 0.64	0.52 ± 0.15
Uterus	15.32 ± 4.31	11 ± 2.85	14.17 ± 2.16
Ovaries	7.86 ± 3.00	6.69 ± 3.69	8.34 ± 2.2
Intestine	8.31 ± 1.57	3.01 ± 0.12 *	4.64 ± 0.35
Spleen	51.43 ± 12.11	18.54 ± 5.29 **	45.26 ± 8.30 **
Liver	12.56 ± 1.86	8.23 ± 1.04	9.79 ± 0.72
Pancreas	1.7 ± 0.30	1.9 ± 0.29	2.26 ± 0.23
Adrenals	3.6 ± 1.09	5.5 ± 3.27	5.82 ± 1.56
Kidney	5.94 ± 0.66	6.87 ± 1.12	7.91 ± 1.39
Lungs	8.01 ± 3.76	8.44 ± 0.67	8.49 ± 1.88
Heart	2.74 ± 0.37	4.07 ± 0.52	3.56 ± 0.28
Tumour	14.34 ± 9.66	16.72 ± 5.37	12.28 ± 4.61
Muscle	1.02 ± 0.17	1.29 ± 0.25	1.08 ± 0.18
Bone	4.82 ± 1.86	3.33 ± 0.89	5.12 ± 1.56
Brain	0.25 ± 0.06	0.37 ± 0.08	0.34 ± 0.06

Although this was not expected, the significantly higher blood in the IgG group would suggest a higher tumour to blood and heart ratios for the control compared to the IgG. However, no significant differences in tumour to blood or heart ratios were evident (Figure 2.6). This was the same for tumour to liver, muscle and kidney. The IgG group did exhibit a higher but not

significant tumour to spleen ratio, which is expected due the significantly lower spleen uptake in this group. Based on these results, the use of IgG as a mechanism to improve tumour contrast is not an effective method. The affinity of the Rabbit IgG to the mouse FcRn may not be sufficient to hinder the recycling of the radiolabeled antibody and thus another method is needed. The optimal conditions for the FcRn recycling are in acidic conditions (pH < 6.5). This phenomenon is why the FcRn works most efficiently in the intestine of rodents and across the placenta to the fetus in humans [39]. At the time of this study, the Ward group demonstrated the use of engineered antibodies (Abdegs) that are able to bind with increased affinity through their Fc region to the FcRn in a pH range of 6.0 -7.4. These Abdegs have been shown to compete with endogenous wild- type IgG and increase their degradation. They demonstrated with the use of these Abdegs at 8 h post injection of ^{125}I-pertuzumab, the uptake in the blood, spleen, heart, kidney were all significantly lower than their control group at 24 h. They also demonstrate an improved tumour to blood ratio in the Abdeg compared to the control both at 24 and 48 h. In contrast to waiting at least 3-5 days post injection of a radiolabeled antibody for sufficient tumour contrast the use of Abdegs out performs using IgG as a method of improved tumour contrast and is achievable at 24 h [122].
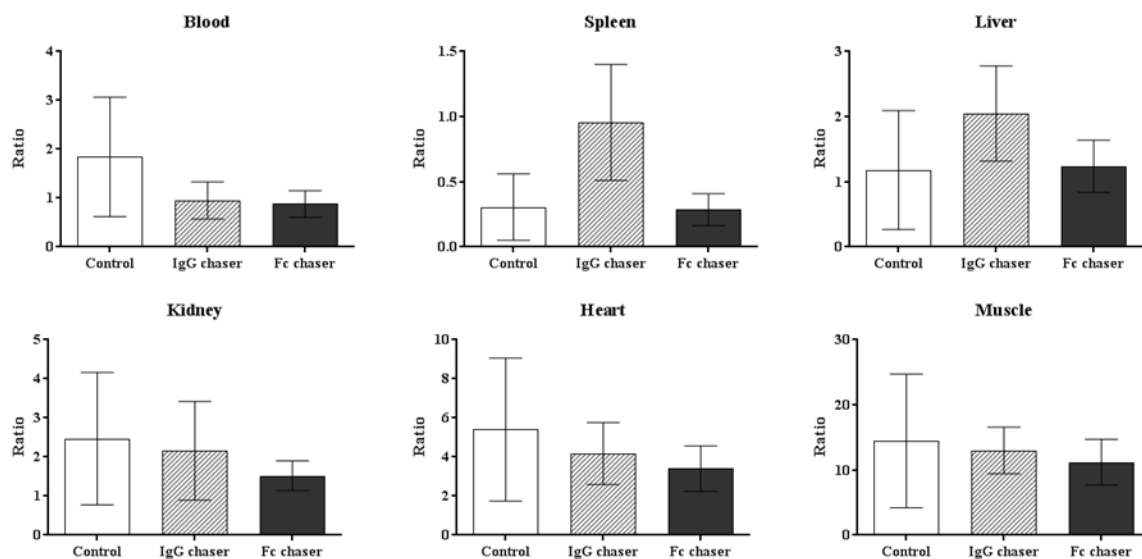
Figure 2.6 Tumour to organ of interest ratio to assess effects of IgG or Fc chasers on antibody clearance. Data is presented as a ratio of tumour %ID/g to organ of interest %ID/g at 24 h post injection of ^{111}In-DTPA-Trastuzumab.

2.3.4   Targeting E-Cadherin Expression as a Potential Marker in Breast Cancer

2.3.4.1   *In vitro* and *ex vivo* Analysis of E-Cadherin Expression

The E-cadherin (E-cad) monoclonal antibody candidates were selected based on their reactivity to both mouse and human E-cad. Since E-cad is endogenously expressed it was important to use a mAb with reactivity to mouse E-cad. Breast cancer cell lines were selected for analysis; MCF7, T47D and MDA-MB-231; the first two being luminal and estrogen receptor (ER) positive carcinomas and the latter a basal and triple negative carcinoma [123]. E-cad expression has been found to be prevalent in ductal normal epithelial mammary glands while aberrant expression evident in breast carcinomas is linked to ER negative, high grade and potential to metastatic behavior [124].

Florescence activated cell sorting (FACS) of cells data demonstrated E-cad expression prevalence in MCF7 and T47D but not with the MDA-MB-231 cells as expected due to their characteristics (Figure 2.7). In comparison of the three E-cad mAb, the rabbit host, close EP700Y showed higher affinity to E-cadherin in all the positive cell lines than the rat DECMA-1 and rabbit 24E10 clones. The rat host, clone DECMA-1 showed affinity to E-cadherin with both T47D and MCF7. Rabbit clone 24E10 showed minimal affinity to E-cadherin with the MCF7 and T47D, even though preliminary studies with western blot showed high expression of E-cadherin. Following literature investigation into 24E10 binding domain showed that 24E10 binds to the intracellular domain of the E-cadherin protein [125]. Comparing the E-cad positive cell lines; T47D demonstrated evidence of higher E-cadherin expression than MCF7. With all three E-cadherin antibodies no affinity for E-cadherin was detected with MDA-MB-231.

Figure 2.7 Flow cytometry data representing E-cadherin expression in breast cancer cell lines. A histogram overlay of MCF7, T47D and MDA-MB-231 cells stained with DECMA-1, 24E10 or EP700Y (blue line). Control conditions with either 2nd alone for DECMA-1, isotype control conjugated and non-conjugated with 488 for 24E10 and EP700Y respectively (red line).

Immunohistochemistry results on tumour slices indicated expression of cytoplasm and membranous E-cadherin using the rabbit 24E10 antibody (dilution 1/100) and rabbit EP700Y (dilution 1/1000) for both MCF7 and T47D tissues. The intensity of staining in these tissues was consistent with the squamous epithelial cells in human tonsil for E-cadherin expression [126]. Staining with DECMA-1 antibody was not performed as it was not suitable for immunohistochemistry. None or minimal expression of E-cadherin was evident in MDA-MB-231 tissue which was expected due to its high aggressive nature and poorly differentiated tumour state. This confirmed specificity of the E-cadherin antibodies to E-cadherin expressing cells. To

further confirm specificity of the antibodies to E-cadherin, the tissues were stained with Rabbit isotype control IgG EPR25A (1/1000); no staining was evident with the control (Figure 2.8).
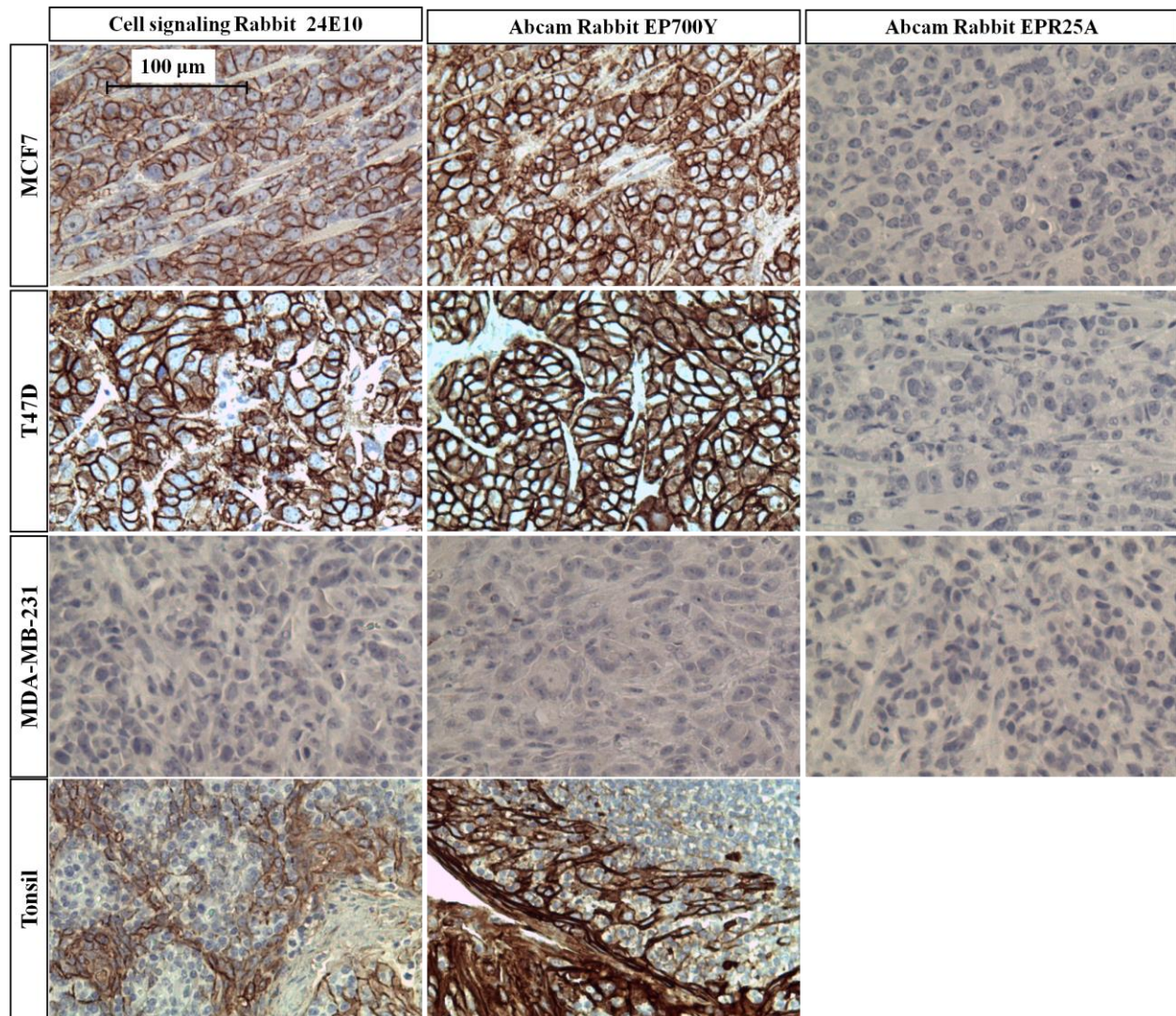
Figure 2.8 E-cadherin expression in MCF7, T47D and MDA-MB-231 cancer model. E-cadherin expression in cell model was confirmed *ex vivo* with immunohistochemistry in MCF7 and T47D stained with 24E10 or EP700Y. Magnification 20x, scale bar 100 μm.

2.3.4.2   Analysis of E-Cadherin Expression *in vivo* with Radiolabeled [111]In E-Cadherin mAbs with SPECT

Conjugation of the selected mAbs with pSCN-Bn-DTPA was achieved using approximately 50 µg of mAb per mouse. SEC HPLC analysis showed intact conjugated mAb post purification and no evidence of aggregation. Radiolabeling with approximately 40 MBq per mouse and all of the conjugated mAb was achieved at ambient temperatures at pH 5.5 at 1 h. Radiolabeling efficiency of 60-80% and radiochemical purity > 95% was assessed by SEC HPLC. Mice with MCF7 and T47D tumours were injected with the maximum amount of E-cadherin antibody radiolabeled to obtain the best tumour uptake. For 24E10 the radiolabeling yield was poor, resulting in only 98 MBq for 6 mice. To obtain µSPECT images, 3 mice were injected with 28.06 ± 1.00 MBq, corresponding to 19.75 ± 0.71 µg of 24E10 and were imaged up till day 5 until biodistribution. The remaining 3 mice were injected with 4.96 ± 0.78 MBq (3.49 ± 0.55 µg) and were kept for biodistribution at day 3. For the DEMCA-1 and EP700Y antibodies, radiolabeling yield was more successful and mice. All mice received 34.81 ± 2.93 MBq (30.2 ± 2.5 µg) of DEMCA-1 or 39.65 ± 3.28 MBq of EP700Y (34.3 ± 3.1 µg). For the rabbit isotype control antibody, the yield of the collected antibody was much lower than that of the E-cadherin antibodies. It was not possible to inject the mice with similar quantities of mAb as the dose to the mice would exceed our animal ethics protocol agreement. As a result, the mice received the maximum dose possible of 36.83 ± 6.13 MBq (8.71 ± 1.5 µg) of EPR25A.

µSPECT/CT acquisitions obtained at day 1 showed typical mAb biodistribution for all E-cad mAb and rabbit isotype control (Figure 2.9). EP700Y appeared to have higher tumour uptake than 24E10 and DECMA-1 at day 1. Low background activity was noted suggesting an elevated E-cadherin expression in the tumour xenografts compared to endogenously expressed E-cad. The tumour uptake of DECMA-1 was unexpectedly lower than 24E10 considering its superior *in vitro* performance (Figure 2.9). T47D tumour uptake was surprising low compared to MCF7 with E-cadherin mAbs considering the higher expression shown in the *in vitro* data. Assessment of biodistribution data at day 3 showed similar uptake in the MCF7 tumour with EP700Y (12.59 ± 3.32 %ID/g) than 24E10 (11.4 ± 0.54 %ID/g). Tumour uptake of both rabbit E-cadherin antibodies was superior to DEMCA-1 in the MCF7 tumour (4.22 ± 0.76 %ID/g). A similar trend

was evident with T47D tumours with uptake of: EP700Y 9.10 ± 1.08 %ID/g, 24E10 5.19 ± 0.13 %ID/g and DECMA-1 2.53 ± 0.98% ID/g. At day 5, MCF7 uptake was still higher than T47D with all E-cadherin antibodies. There was a shift in leading antibody uptake; uptake in the MCF7 tumour of 24E10 appeared to be maintained (12.53 ± 0.75 %ID/g) while uptake of EP700Y decreased to 8.37 ± 3.93 %ID/g as did DECMA-1, 3.13 ± 0.40 %ID/g. The uptake of 24E10 in both MCF7 and T47D was similar from day 3 to 5. The antibody uptake is maintained from day 3 to 5; initial thoughts suggested that this could be attributed due to mAb internalization as at the time of this *in vivo* study we had not realized that the 24E10 bound to the intracellular domain of the E-cadherin protein [125].
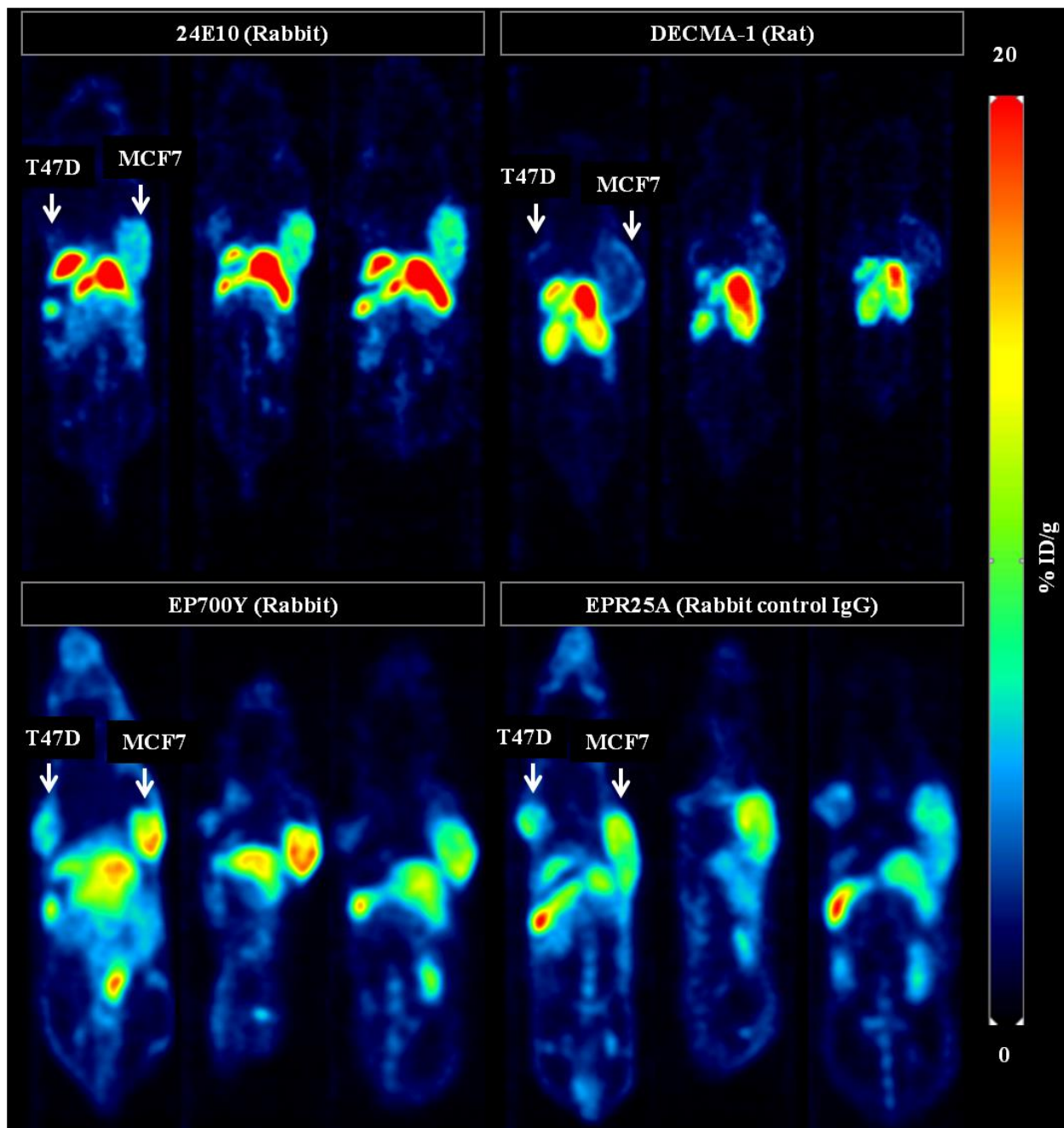
Figure 2.9 µSPECT images of mAb uptake of E-cadherin mAbs: 24E10 (rabbit), DECMA-1 (rat) and EP700Y (rabbit) and control rabbit IgG EPR25A in T47D and MCF7 xenograft models. Representative coronal slices were acquired through the center point of the MCF7 tumour at day 1, 3 and 5 for each antibody. Scale bar represents % ID/g.

Even with relatively low tumour uptake of E-cadherin antibodies, control studies were needed to ascertain whether uptake of the E-cadherin mAb was E-cadherin expression driven or due to the enhanced permeability retention (EPR) effect. Due to the overall higher uptake in the rabbit E-cadherin mAbs EP700Y and 24E10 compared to rat DEMCA-1 a rabbit isotype IgG control mAb (EPR25A) was conjugated and radiolabeled and injected into tumour bearing mice. Rabbit IgG EPR25A control mAb had lower tumour uptake in the MCF7 tumours (10.09 ± 1.05 %ID/g) than the counterpart rabbit E-cadherin mAbs at day 3 and 5 (Table 2.3). The T47D tumours had uptake of EPR25A (8.40 ± 1.54 %ID/g) that was lower than the EP700Y but higher than 24E10 at day 3. At day 5 however, EPR25A uptake in the T47D tumour was higher (6.83 ± 1.02 %ID/g) in the IgG than both EP700Y and 24E10. The use of these selected mAbs as diagnostic markers for E-cadherin was not successful; however, as agents for IHC, the E-cadherin show high specificity. With modification of antibodies during conjugation there is a possibility of affecting the binding affinity. With the E-cadherin studies an immunoreactivity test was not performed with these DTPA-chelated E-cadherin antibodies. As such, the affinity of the E-cadherin antibody may have been significantly reduced resulting in lower uptake compared to the control isotype IgG. We know from Trastuzumab, a DTPA:Trastuzumab ratio of 5:1 maintains the binding affinity when tested with SKOV-3 cells. However, with non-specific conjugation of a chelator to an antibody the possibilities of the conjugation sites of the chelator on the antibody could directly affect the binding site of the antibody. In addition, it is possible that while E-cadherin expression with these cells might be very high and bind to the extracellular domain of the E-cadherin protein; the accessibility of an antibody to the E-cadherin site may be limited due to the gap junctions that are held by E-cadherin. A more exposed E-cadherin may occur during the progression of invasion and metastatic growth and tumour reformation. It has been shown that E-cadherin is re-expressed at distant metastatic foci and it is possible scenario where the antigen sites may be more exposed is during the formations of metastatic tumours.

Table 2.3 Biodistribution of tumour and non-tumour organs for ^{111}In-pSCN-Bn-DTPA-24E10, DECMA-1, EP700Y or EPR25A uptake in MCF7 and T47D tumour bearing mice at day 3 and 5. Data is presented as mean ± SD, %ID/g, n ≥ 3. (NA: not acquired)

| | Day 3 | | | | Day 5 | | | |
	24E10	DECMA-1	EP700Y	EPR25A	24E10	DECMA-1	EP700Y	EPR25A
Blood	1.02 ± 0.05	5.16 ± 0.92	4.36 ± 1.64	2.26 ± 0.45	3.28 ± 1.06	3.99 ± 0.43	0.69 ± 0.35	0.78 ± 0.38
Fat	1.41 ± 0.58	N/A	1.05 ± 0.47	1.84 ± 1.27	2.26 ± 0.62	N/A	1.2 ± 0.44	2.44 ± 1.94
Uterus	14.86 ± 0.47	4.45 ± 1.48	25.89 ± 4.95	26.87 ± 4.90	11.56 ± 1.71	0.9 ± 0.49	23.26 ± 8.13	18.31 ± 2.54
Ovaries	6.97 ± 0.67	5.94 ± 1.63	15.8 ± 3.4	20.05 ± 3.73	7.08 ± 0.55	7.24 ± 2.48	10.9 ± 3.27	13.52 ± 4.94
Intestine	3.01 ± 0.36	4.58 ± 1.83	5.89 ± 2.41	4.43 ± 0.37	2.43 ± 0.22	2.21 ± 0.32	2.59 ± 0.91	3.29 ± 1.86
Spleen	63.85 ± 10.50	12.66 ± 3.90	136.01 ± 22.0	146.68 ± 51.0	121.31 ± 11.75	10.23 ± 2.44	122.5 ± 16.5	135.21 ± 27.8
Liver	60.17 ± 0.73	31.90 ± 3.76	16.44 ± 2.15	15.2 ± 2.00	48.37 ± 6.66	23.22 ± 7.25	13.7 ± 2.11	13.56 ± 1.38
Pancreas	1.10 ± 0.07	3.15 ± 2.03	1.65 ± 0.33	1.44 ± 0.27	1.03 ± 0.08	1.76 ± 0.39	1.40 ± 0.44	1.15 ± 0.31
Adrenals	9.24 ± 4.62	2.45 ± 0.72	3.29 ± 1.00	3.74 ± 0.59	5.2 ± 0.34	1.61 ± 0.59	2.11 ± 0.57	3.06 ± 1.61
Kidney	8.77 ± 0.65	21.35 ± 7.60	4.69 ± 0.85	5.17 ± 0.35	7.87 ± 0.82	19.73 ± 4.44	3.39 ± 1.19	4.15 ± 0.77
Lungs	1.84 ± 0.13	3.46 ± 0.93	4.58 ± 1.32	3.14 ± 0.61	2.49 ± 0.41	2.60 ± 0.48	1.60 ± 0.46	1.92 ± 0.88
Heart	1.44 ± 0.13	1.30 ± 0.35	2.01 ± 0.25	1.92 ± 0.31	1.46 ± 0.12	0.93 ± 0.21	1.01 ± 0.21	1.08 ± 0.18
MCF7	11.4 ± 0.54	4.22 ± 0.76	12.59 ± 3.32	10.09 ± 1.05	12.53 ± 0.75	3.13 ± 0.40	8.37 ± 3.93	7.83 ± 2.13
T47D	5.19 ± 0.13	2.53 ± 0.98	9.10 ± 1.08	8.40 ± 1.54	5.62 ± 0.73	2.12 ± 0.43	4.98 ± 0.66	6.83 ± 1.02
Muscle	0.62 ± 0.08	0.42 ± 0.05	0.78 ± 0.14	0.66 ± 0.11	0.51 ± 0.1	0.32 ± 0.08	0.46 ± 0.23	0.53 ± 0.13
Bone	3.41 ± 0.56	0.87 ± 0.46	4.11 ± 1.38	4.44 ± 2.20	2.16 ± 0.18	0.56 ± 0.02	2.58 ± 0.80	2.87 ± 0.68
Brain	0.08 ± 0.02	0.12 ± 0.02	0.16 ± 0.06	0.10 ± 0.02	0.13 ± 0.03	0.11 ± 0.01	0.08 ± 0.05	0.07 ± 0.02

It is possible that *in vivo* these xenografts do not express E-cadherin as *in vitro*. Since *in vivo* data does not always represent data obtained from *in vitro* analysis, fluorescence activated cell sorting of cells derived from xenograft tumours was performed. Here, there was in-consistent E-cad expression in MCF7 and T47D cells from tumours compared to data collected from cells (Figure 2.10). MDA-MB-231 cells derived from tumours did not exhibit E-cadherin expression. In general, the tumour cells seem to show a varied expression of E-cadherin compared to the clearer results obtained from cells. This trend was evident with DECMA-1, where more variability in E-cadherin expression was evident in the T47D tumour cells than the MCF7 tumour cells. Antibody 24E10 showed minimal differences between E-cadherin expression in both tumour cells compared to both cell lines. MCF7 tumour cells showed minimal E-cadherin expression when stained with EP700Y compared to the cells, while T47D tumour cells appeared to still retain some expression, although quite varied. Based on biodistribution data, we would expect the MCF7 tumour cells to demonstrate a higher expression than T47D tumour cells. In addition, we would anticipate lower expression with DECMA-1 staining than 24E10. The cells extracted from the xenograft tumour appeared to demonstrate similar E-cadherin expression as the cells alone suggesting that the poor uptake in the tumours could be due reduced accessibility of the antibody to the E-cadherin molecule or possibility reduce binding affinity of the conjugated antibody. *In vivo* glycosylation of E-cadherin may occur and affect the binding of the mAbs to the epitope. However, as we observed a strong staining of the mAbs with IHC and from cells derived from tumour with FACS, this potential glycosylation cannot explain the low binding. Performing an additional FACS analysis on both cells and cells from tumours using both an unmodified E-cadherin antibody and a conjugated antibody may provide more evidence to conclude on the feasibility of using E-cadherin antibodies as an imaging vector.
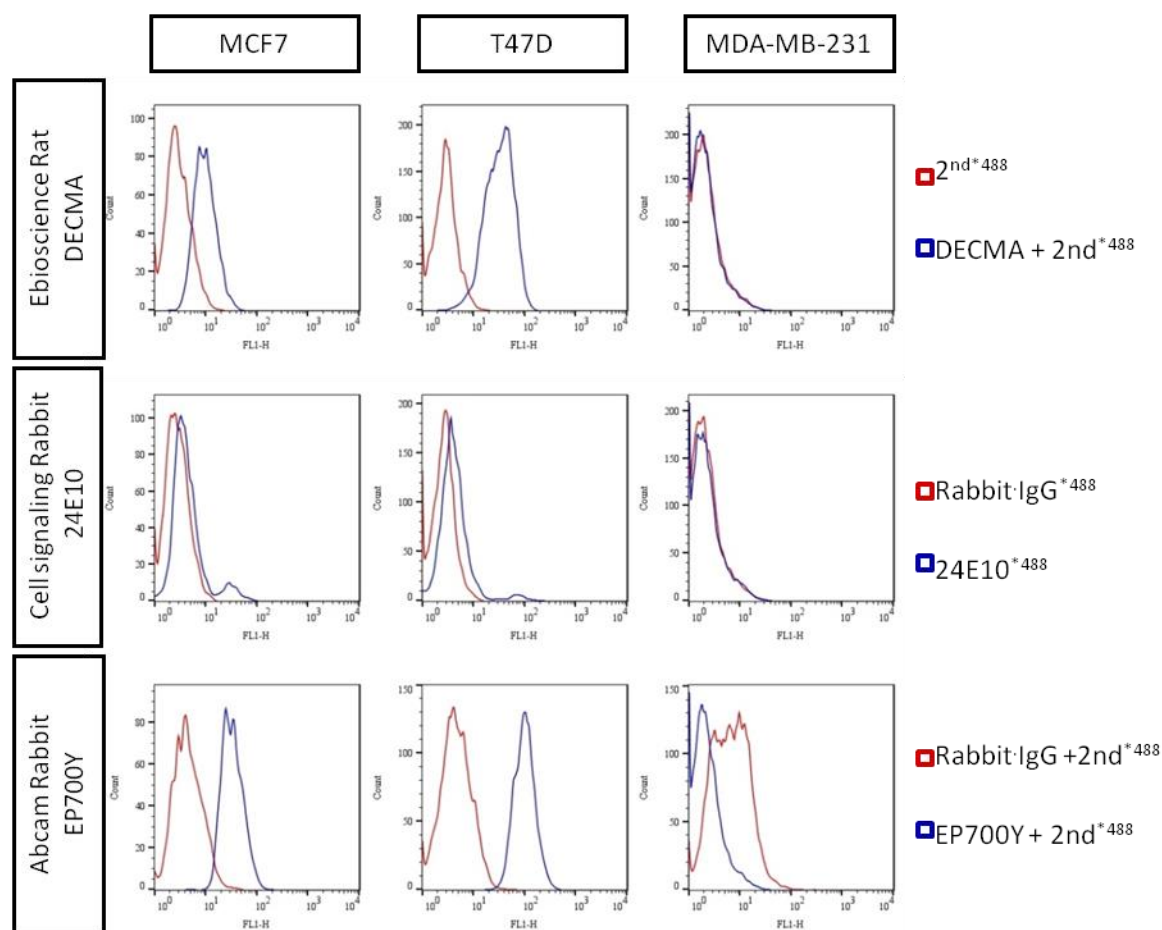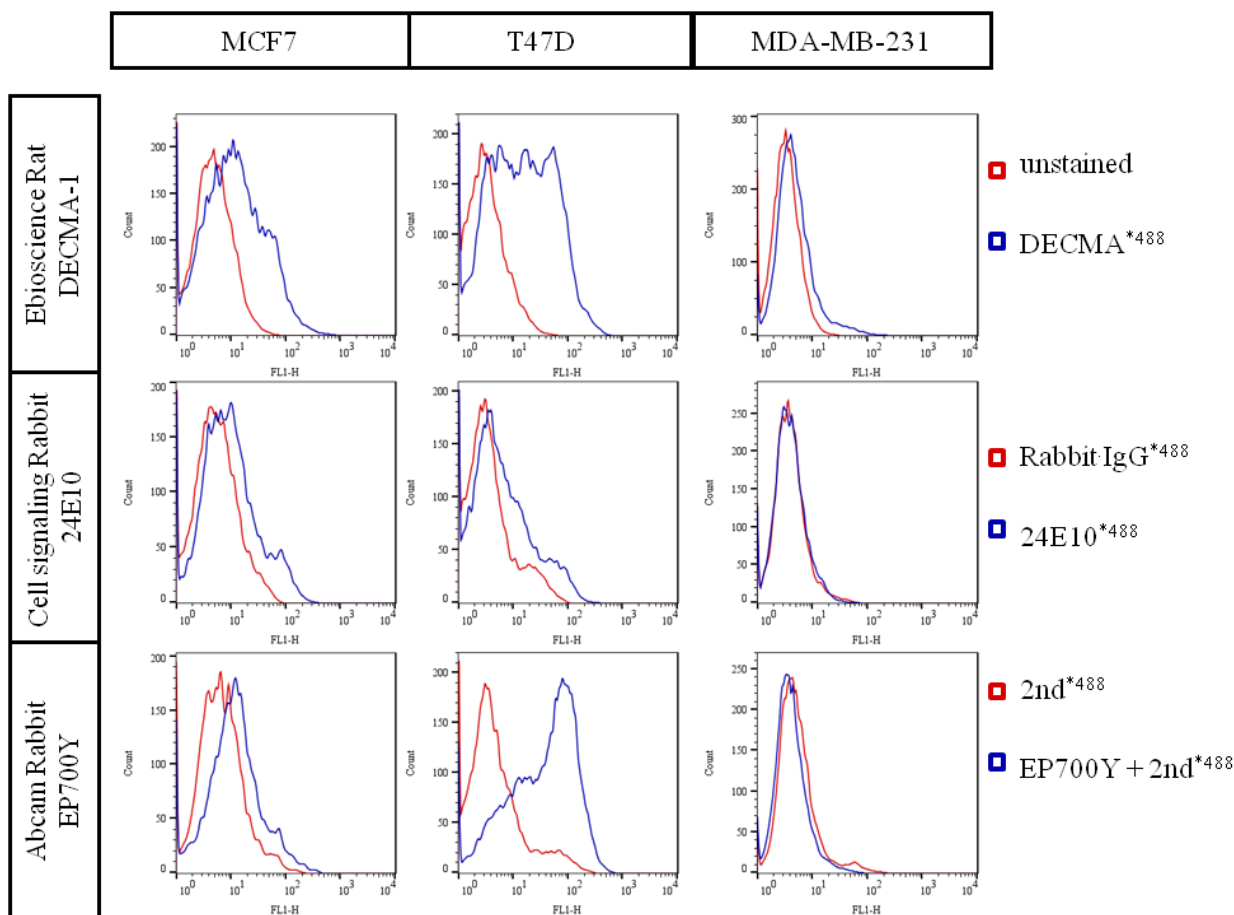
Figure 2.10 Flow cytometry data representing E-cadherin expression in breast cancer cells from tumours. Overlay histogram of MCF7, T47D and MDA-MB-231 cells stained with DECMA-1, 24E10 or EP700Y.

2.4 Conclusion

We demonstrated ^{111}In radiolabeling and μSPECT imaging of Trastuzumab targeting HER 2 and novel mAbs targeting E-cadherin. Reducing the injected dose of ^{111}In-Trastuzumab showed no difference in tumour uptake or biodistribution. However, a trend of higher uptake as injected dose per gram was observed in the liver and spleen with decreasing Trastuzumab dose. A comparison of Trastuzumab conjugated with p-SCN-Bn-DTPA or p-SCN-Bn-CHX-A"-DPTA and radiolabeled with ^{111}In showed no differences in immunoreactivity and minimal biodistribution differences. We demonstrate that p-SCN-Bn-CHX-A"-DTPA performed similarly to the less expensive pSCN-Bn-DTPA with [111]In. Attempts to improve tumour contrast

of Trastuzumab by saturating the FcRn with rabbit IgG or rabbit IgG Fc fragments were not successful. Finally, screening of mAbs to target E-cadherin was confirmed with both fluorescence activated cell sorting and immunohistochemistry of xenograft tumour tissue. *In vivo* biodistribution of E-cadherin xenograft uptake of E-cadherin mAbs was not significantly higher than an isotype control IgG.

Chapter 3: ^{89}Zr for Immuno PET

3.1   Introduction

Prior to the development of the PET scanner, mAb-based imaging was limited to scinitgraphy and then later SPECT. However, limitations in sensitivity and resolution diminished the full potential targeted imaging with radiolabeled antibodies [127]. The development of the PET scanner immensely improved the opportunity to obtain higher sensitive and higher resolution mAb radioimmuno imaging. Utilizing PET opened the opportunity to explore a variety of PET radioisotopes; however only a few would be suitable for mAb PET imaging. The positron emitting radioisotope should havedecay characteristics that provide optimal resolution and quantitative accuracy for PET imaging. In addition; production of the radioisotope should be easy and economically viable, it should radiolabel mAb with temperatures and buffer conditions suited to the mAb and should be stable once radiolabeled. As always with mAb imaging; the radioisotope should have a physical half life suitable to the biological half-life of mAbs [127].

Zirconium-89 (^{89}Zr) is rapidly gaining interest as a valuable radionuclide for immunoconjugate PET imaging. Favourable decay properties of $T\frac{1}{2}$ =78.4 h, $E_{\beta+}$ = 396 keV and a 23% positron yield make this radionuclide ideal for mAb PET imaging. The primary feature of this highly attractive radiometal is its suitable half-life; slightly longer than the previously discussed ^{111}In, but still pairing well with the biological half-life of antibodies. A high energy gamma peak (E_{max} = 909 keV) exceeds the energy window for PET imaging, making this radioisotope attractive for clinical and preclinical use. Additionally; ^{89}Zr can be produced at a low energy using a starting material of naturally abundant, isotopically pure and inexpensive yttrium-89, making it affordable and available on clinical cyclotrons [100, 128] .

The low energy requirements for ^{89}Zr production allowed the possibility of developing ^{89}Zr production on the TR 19 cyclotron at the BCCA. At the start of this project, there were few publications available for ^{89}Zr production and the pitfalls, challenges and ultimate successes with this production will be discussed. Once successful production and purification was achieved,

optimization of mAb radiolabeling was performed. To complete the process µPET CT imaging using HER2 positive xenograft mice was performed using Trastuzumab radiolabeled with ^{89}Zr. To maximize experimental data an *in vivo* study comparing the effects of injected dose on tumour uptake and biodistribution were performed. To compare with ^{111}In radiolabeled antibodies, the *in vitro* data acquired from the EP700Y antibody was promising, and so we performed conjugation and radiolabeling of EP700Y and EPR25A with ^{89}Zr for E-cadherin imaging.

3.2   Materials and Methods

Yttrium-89 metal sheets (3N purity, 0.254 and 1.016 mm thickness) were purchased from American Elements (Los Angeles, California USA) or EPSI (Ashland, Oregon USA) and water jet cut into 10 or 25.4 mm diameter discs. Irradiations were performed on a TR 19 MeV cyclotron (ACSI, Richmond). Ultrapure HCl (TraceSELECT$^{®}$), and sodium oxalate (99.99% trace metal basis) were purchased from Sigma-Aldrich (Oakville, Ontario, Canada). A Millipore system (Direct-Q$^{®}$ 3UV with Pump, 18 MΩ cm^{-1}) provided ultrapure water. The bifunctional chelator *p*-SCN-Bn-deferoxamine (*p*-SCN-Bn-DFO) was purchased from Macrocyclics (Dallas, TX, USA). DMSO used for chelator stock solutions was of molecular biology grade (> 99.9%: Sigma). All other chemicals were analytical grade and used without further purification. Purification of ^{89}Zr-labeled antibody conjugates was performed using GE Healthcare Life Sciences PD-10 desalting columns (GE Healthcare, United Kingdom, MW < 50 kDa filter) that were preconditioned by elution of 25 mL of phosphate buffered saline (PBS, pH 7.4) before use, and centrifugal filter units with a 50,000-molecular weight cutoff (Amicon ultracentrifuge filters, Ultracel-50: regenerated cellulose, Millipore Corp., Billerica, MA). The radiolabeling of bioconjugates was monitored using silica-impregnated instant thin-layer chromatography paper (iTLC-SG) (Agilent Technologies) and analyzed on a Ray Test miniGita with Beta GMC detector radio-TLC plate reader using TLC control Mini Ginastar software. High performance liquid chromatography (HPLC) analyses of purified ^{89}Zr-DFO-trastuzumab were carried out using a size-exclusion chromatography (SEC) column (Phenomenex, BioSep-SEC-s-3000) on an Agilent™ system equipped with a model 1200 quaternary pump, a model 1200 UV absorbance detector (set at 280 nm), and a Bioscan (Washington, DC) NaI scintillation detector

(the radiodetector was connected to a Bioscan B-FC-1000 flow-count system, and the output from the Bioscan flow-count system was fed into an Agilent 35900E interface, which converted the analog signal to a digital signal).

3.2.1 ^{89}Zr Production

Yttrium foil sheets were water jet cut into circular discs either 25.4 mm or 10 mm in diameter. The 25.4 mm diameter discs were loaded directly on the solid target holder while 10 mm discs were sandwiched between an aluminum (Al) ring and backing and then loaded onto the solid target holder adapted from Zeisler et al. [99] (Figure 3.1). The nose-piece of the target mounts into the solid target station on the cyclotron perpendicular to the beam. A vacuum is situated between the beam and a double havar foil window that allows for helium cooling. The target sits in the support ring. For yttrium foils of 25.4 mm, the foil was directly cooled with H_2O while 10 mm diameter foils were cooled at the aluminum backing. Irradiation of solid target production of ^{89}Zr was achieved on a TR19 cyclotron at the BC Cancer Agency. To optimize production yield beam parameters such as energy irradiation time, current and dose were adjusted produce sufficient yields for radiolabeling, taking into consideration operational constraints (Table 3.1).
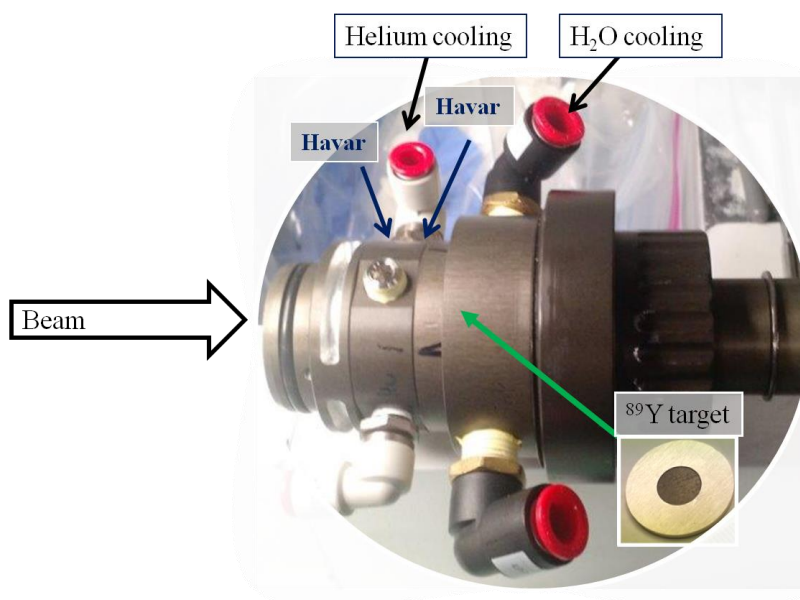
Figure 3.1 Photograph of the solid target holder for ^{89}Zr production. The ^{89}Y target shown in the lower right corner is the 10 mm foil sandwiched between an Al ring and backing.

Table 3.1 ^{89}Zr Production Parameters

Cyclotron	TR19 BCCA				
Starting material Ø [mm]	25.4	25.4	10	10	10
Thickness [mm]	1.016	1.016	1.016	0.254	0.254
Mass [g]	2.3	2.3	0.36	0.09	0.09
Proton energy [MeV]	15.5	15	13.8	13.8	13.8
Beam current [µA]	19.5 ± 5.5	17.2 ± 5.15	15.11 ± 5.0	14.6 ± 4.2	14.6 ± 3.6
Beam time [min]	15 ± 5	49 ± 30	68 ± 36	60 ± 28	125 ± 50

3.2.2 Purification

The hydroxamate resin used for the purification of ^{89}Zr was prepared as described by Holland et al [100]. Briefly, silica-based Waters Accell Plus CM weak cation exchange resin (Waters, Milford MA, USA) was suspended in water with tetrafluorophenol (TPA) in MeCN and 1-ethyl-3-dimethlaminopropyl carbodiimide hydrochloride (EDAC). After an addition of further TFP and EDAC the activated TFP ester group was converted with hydroxylamine hydrochloride into the hydroxamate resin. After 18 h incubation the hydroxamate resin was washed thoroughly with water and MeCN, dried and stored at 4 °C. For each 100 mg of the hydroxamate resin used, it was activated with MeCN (8 mL), washed with H_2O (15 mL) and conditioned with 2 M HCl (4 mL) one hour prior to purification. The 25.4 mm diameter irradiated ^{89}Y foils were dissolved in 4-5 mL of 6 M HCl. This was performed in a closed system and left to dissolve for 1 h to allow particulates from the dissolution to settle. For smaller diameter irradiated ^{89}Y foils, dissolution was achieved with 2 mL of 6 M HCl. The dissolved foil solution was then diluted to 2 M HCl with H_2O and loaded onto the conditioned hydroxamate resins. Once the ^{89}Zr was trapped, the resins were washed with 2 M HCl (10 mL) and washed with H_2O (10 mL) and subsequently air dried. The ^{89}Zr was eluted from the resins with 1.0 M oxalic acid in aliquots of 0.5 mL.

3.2.3   Conjugation of *p*-SCN-Bn-DFO to mAbs

Trastuzumab (Herceptin, Genentech, San Francisco, CA) was purified using centrifugal filter units with a 50 kDa molecular weight cutoff (Amicon ultracentrifuge filters, Ultracel-50: regenerated cellulose, Millipore Corp., Billerica, MA) and washed with PBS (pH 7.4 to 8.9-9.1 for the last wash) to remove α-α-treholase dehydrate, L-histidine, and polysorbate 20 additives. Rabbit host clone EP700Y E-cadherin monoclonal antibody and rabbit monoclonal IgG isotype control, clone EPR25A were custom purchased from abcam (Cambridge, UK) at a concentration of 1.9 mg/mL azide free.   Purified Trastuzumab was conjugated with p-SCN-Bn-desferoxamine (DFO, Sigma-Aldrich, Oakville, Ontario Canada) at room temperature overnight.   To optimize radiolabeling a molecular ratio of both 3:1 and 6:1 (DFO:mAb) in PBS pH 8.9-9.1 were used for the Trastuzumab. The E-cadherin antibody (EP700Y) and rabbit IgG isotype control (EPR25A) both from abcam (Cambridge, UK) were conjugated at a 3:1 ratio. Conjugated antibody (DFO-mAb) was then purified using the centrifugal filter technique described above and washed once with 5 mg/mL dihydrobenzoic acid, in 0.25 M sodium acetate solution (both from Sigma-Aldrich).

3.2.4   Radiolabeling of *p*-SCN-Bn-DFO-mAbs

To optimize radiolabeling yield and to obtain a specific activity appropriate for immune-PET imaging a combination of parameters were used. The volume and amount of ^{89}Zr, the amount of DFO-Trastuzumab and the ratio of DFO:Trastuzumab were varied to obtain ideal radiolabeling conditions (Table 3.2) . For the optimization experiments the radiolabeling yield was assessed by iTLC and the specific activity was calculated based on the radiolabeling yield and the mass of conjugated antibodies used for labeling. Once the optimized protocol was achieved, the ^{89}Zr-DFO-antibody complex was purified using size exclusion PD-10 desalting columns with PBS pH 7.4 and concentrated using 50 kDa molecular weight cut off filters. Final radiochemical purity and specific activity were determined using size–exclusion HPLC.

Table 3.2 ^{89}Zr DFO-Trastuzumab Radiolabeling Parameters

^{89}Zr (µL)	100 - 200					20 -100			< 20
DFO:mAb	3			6		3		6	3
mAb [µg]	500	200	< 50	500	200	200	< 50	200	< 50

3.2.5   µPET/CT Imaging and Biodistribution

All animal experiments were performed at the Animal Resource Centre of the BC Cancer Agency Research Centre in accordance with the institutional guidelines of the University of British Columbia Animal Care Committee (Vancouver, BC, Canada) and under the supervision of authorized investigators.

Female immunodeficient NOD.Cg-Prkdcscid Il2rgtm1Wjl/SzJ (NSG) mice (obtained from an in-house breeding colony) were used for all studies. For the radiolabeling of Trastuzumab, mice were subcutaneously injected with 6 x 10^6 SKOV-3 cells in a 50:50 mixture of growth medium and basement membrane matrigel (BD science). Two weeks post cell implantation the mice were injected with the ^{89}Zr radiolabeled Trastuzumab with doses of either 10.56 MBq (33 µg), 5.76 MBq (18 µg) or 1.28 MBq (4 µg). PET images of 15 min duration were acquired 1, and 3 days post-injection using a Siemens Inveon microPET/CT scanner (Siemens Medical Solutions, Knoxville, TN, USA) and under anesthesia (2% isoflurane-O_2). Each mouse underwent a CT scan for attenuation correction followed by a PET acquisition. Images were reconstructed using the 3-dimensional ordered-subsets expectation maximization (OSEM3D, 2 iterations) followed by a fast maximum a priori algorithm (FastMAP: 18 iterations) and attenuation corrected based on the CT image.

For E-cadherin antibody studies, mice were implanted with a 17β-estradiol pellet (Innovative Research of America). Seven days later the mice were subcutaneously injected with 6 x 10^6 MC7 cells on the right shoulder and T47D cells on the left shoulder. Five-six weeks after cell implantation the mice were anaesthetized with isofluane (2% in O_2) and injected via tail with

^{89}Zr-DFO-E-cadherin-EP700Y or ^{89}Zr-DFO-Rabbit IgG Isotype- EPR25A. PET images of 15 min duration were acquired 1, 3 and 5 days post-injection with a CT scan for attenuation correction.

3.2.6   Biodistribution data

To assess the effect of injected antibody dose; mice were euthanized by inhalation of isoflurane followed by CO_2 at day 3 after injection of ^{89}Zr-DFO-Trastuzumab. At day 3 and 5 after injection of the ^{89}Zr-DFO-E-cadherin-EP700Y or ^{89}Zr-DFO-Rabbit IgG Isotype-EPR25A, mice were euthanized by inhalation of isoflurane followed by CO_2. Blood was withdrawn by intracardiac puncture, and then tumours and organs of interest were harvested, washed in PBS and weighed after blotted drying. Activity of each sample was measured by a gamma counter with decay correction. The activity uptake was expressed as a percentage of the injected dose per gram of tissue (%ID/g). Statistical analyses for biodistribution data were performed using GraphPad Prism (version 7). *P* values were calculated using ANOVA and values < 0.05 were considered statistically significant.

3.3   Results and Discussion
3.3.1 ^{89}Zr Production Results

Initial ^{89}Zr production on the TR19 at BCCA was achieved at 15 MeV with short beam irradiations of 15 ± 5 min (Bombardment condition 1, Table 3.3). These initial irradiations used a 1.016 mm thick yttrium source of ^{89}Y, 25.4 mm diameter and produced 377 ± 213 MBq of ^{89}Zr EOB. Beam current differences between the runs were primarily due to the optimization of beam current (μA) to produce high yield without burning the target. In addition, differences in delivered dose (μA·min) were due to scheduling availability for target loading and retrieval. Due to the infrequency of ^{89}Zr production runs, loading and unloading of the target was performed manually, beam time and target retrieval were dependent on the daily ^{18}F-FDG productions and other research production irradiations. Thus, beam time parameters were modified to ensure sufficient ^{89}Zr at the time of purification (Table 3.3). By increasing the irradiation time and thus delivered dose (Bombardment condition 2) by a factor of 3, an increase in activity at EOB by a factor of 3 was observed (1324 ± 266 MBq). A beam energy of 15 MeV

resulted in the production of yttrium-88 (^{88}Y) a long live ($T_{1/2}$ 106 d) isotope, as observed with gamma spec analysis. While this was separated from the ^{89}Zr during purification it resulted in the generation of unnecessary long lived radioactive waste. The maximum cross section for the ^{89}Y(p,n)^{89}Zr reaction is situated at 15 MeV; and based on published data this is the optimal energy for ^{89}Zr [95, 100]. The ^{89}Y(p,x)^{88}Y reaction is optimal around 25 MeV and while yield is reduced at lower beam energies we still observed ^{88}Y in our sample. This is discordant with Holland et al. [100] who reported the absence of ^{88}Y at 15 MeV. We initially hypothesized that this could be due to slight differences in the accuracy of beam energy determination between sites, even though we used the same cyclotron as Holland et al. in our studies. Precise measurements using the dual copper foil technique [129] confirmed that the beam energy reported by our cyclotron control system was properly calibrated. We thus decided to reduce the beam energy to 13.9 MeV, the minimum energy achievable on that particular beam line at the expense of a slight reduction in ^{89}Zr production yield. With the reduction of beam energy, we could reduce the ^{88}Y produced during the bombardment. A recent publication by Queern et al., at a beam energy of less than 13 MeV provided 100% radionuclidic purity [130].

In addition to the decrease in beam energy, the diameter of the ^{89}Y was also decreased. While the amount of starting material influences the produced yield it also is accompanied with non radioactive impurities in the target material which can affect radiolabeling yields. Decreasing the diameter to 10 mm, decreased the saturated yield as a higher integrated dose was required; however a substantial EOB activity of 896 ± 278 MBq was achieved (bombardment condition 3, Table 3.3). To further improve radiochemical purity, we changed supplier for the ^{89}Y disc used in our target. ^{89}Y from this alternate supplier contained less iron by weight based on the certificate of analysis. By changing the supplier, decreasing the diameter and thickness (from the original 25.4 mm ^{89}Y foil), the iron (Fe^{3+}) content in the starting material decreased from 0.2% to 0.01% by weight (by a factor of 50).

With this new ^{89}Y target with a 10 mm diameter, production run parameters were varied. Shorter runs (60 ± 28 min) where purification was scheduled the same or within one day of the irradiation were run with an average integrated dose of 755 ± 124 µA·min and resulted in 456 ± 115 MBq of ^{89}Zr produced decay corrected to end of bombardment (EOB, n = 9 runs). Longer

irradiations, typically 125 min, where performed when purification was scheduled for at least 24 h post irradiation and were run with an average integrated dose of 1690 ± 422 µA·min and resulted in 739 ± 229 MBq ^{89}Zr decay corrected to EOB (n = 5).

It is a challenge to compare to other published ^{89}Zr production yields due to differences in beam parameters and starting material thickness (Table 3.4). Standardized ^{89}Zr described by Holland [100] demonstrate high EOB yields at 15 MeV with a starting material weight of 0.33 g. With our 2.3 g target at 15 MeV and similar beam current we obtained high saturated yields (96.7 ± 8.20 MBq/µA·h). Taking into account a lower thickness and diameter of the yttrium foil to reduce iron and impurities and decreasing the beam energy to reduce ^{88}Y impurities, the end of bombardment activity was proportional to published data.

Table 3.3 ^{89}Zr Production results

Bombardment condition	1	2	3	4	5
Starting material Ø [mm]	25.4	25.4	10	10	10
Thickness [mm]	1.016	1.016	1.016	0.254	0.254
Mass [g]	2.3	2.3	0.356	0.089	0.089
Dose [µA.min]	266 ± 141	688 ± 151	993 ± 461	755 ± 124	1690 ± 422
Number of runs	5	6	6	9	5
Proton energy [MeV]	15.5	15	13.84	13.9	13.9
Beam current [µA]	19.5 ± 5.5	15.7 ± 4.7	15.1 ± 5.0	14.6 ± 4.2	14.6 ± 3.6
Beam time [min]	15 ± 5	49 ± 30	68 ± 36	60 ± 28	125 ± 50
EOB Yield [MBq]	377 ± 213	1324 ± 266	896 ± 278	456 ± 115	738 ± 229
Saturated Yield [GBq/µA]	9.75 ± 1.75	10.9 ± 0.9	6.83 ± 2.6	3.9 ± 0.6	3.0 ± 1.0

Table 3.4 Comparison of ^{89}Zr production to literature results

	Holland [100]	BCCA	
Starting material [g]	0.33	2.3	0.089
Proton energy [MeV]	15	15	13.9
Beam current [µA]	15	15.7 ± 4.7	14.0 ± 3.8
Beam time [min]	145 ± 18	49 ± 30	137 ± 50
EOB Yield [MBq]	2044 ± 387	1324 ± 266	715 ± 257
Saturated Yield [MBq/µA·h]	56.1 ± 4.3	96.7 ± 8.20	25.1 ± 9.42

3.3.2 ^{89}Zr Purification and Separation Results

Purification of the ^{89}Zr from the starting ^{89}Y material was achieved via solid phase separation on a hydroxamate resin, following previously published methods [100].   Dissolution of the irradiated ^{89}Y 25.4 mm diameter foil was achieved with 4-5 mL of 6 M HCl.   Complete dissolution of the foil was achieved within 30 - 40 min.   The creation of highly volatile radioactive particulates required a closed purification system.   To further minimize the potential spread of radioactive contamination from particulates and allow time for the exothermic dissolution process to cool to ambient temperature, purification started 1 h after complete dissolution.   On average purification was conducted 1 h post complete dissolution of the foil. Once the foil was dissolved purification of ^{89}Zr was achievable in approximately 60 min from the start of loading the solution on the hydroxamate resin.   Due to the difference in starting ^{89}Y material compared to literature, 300 mg of hydroxamate resin was used to purify the ^{89}Zr from the 25.4 mm foils.   For the smaller and thinner foils, 2 mL of 6 M HCl was required for dissolution and complete dissolution was achieved with 5 min.   As the starting material was reduced, the amount of hydroxamate resin was also reduced.

As described in the methods, the dissolved foil solution was diluted to 2 M HCl and loaded onto the resin.   The resin was washed with 2 M HCl (10mL per 100mg of resin) and H_2O (10mL per 100 mg of resin) and air dried.   Using 300 mg of hydroxamate resin, 1.0 mL of 1 M oxalic acid was used to elute the ^{89}Zr (Table 3.5).   This first elution purified $43 \pm 27\%$ of the ^{89}Zr that had

been trapped on the resin. This gave 46 ± 8 MBq of ^{89}Zr in 1.0 mL; an additional 1.0 mL elution resulted in a total of 99 ± 40 MBq of ^{89}Zr. The highest elution yield resulted in a concentration of purified ^{89}Zr of 54 ± 17 MBq/mL. To improve this low concentration, irradiation time was increased (bombardment condition 2, Table 3.3) to produce higher ^{89}Zr yields. In addition to the increase in yield, we attempted to completely elute as much ^{89}Zr from the resin as possible with an increase in elution volume (3 mL). This was to then converted the ^{89}Zr-oxalate into ^{89}ZrCl$_4$ in saline with a QMA column as suggested by Holland [100]. Unfortunately, the procedure was challenging and inconsistent. Between 20-63% of the ^{89}Zr that had been purified from the hydroxamate resin was successfully converted into ^{89}ZrCl$_4$.

At this point, we decided to reduce the diameter of the ^{89}Y foil. With this almost ten-fold decrease in mass (0.356 g) the hydroxamate resin mass was also decreased to 100 mg as per Holland [100]. Dissolution of this 10 mm irradiated foil required only 2 mL of 6 M HCl and was achieved in 10 min. The start of purification was still held to one hour after complete dissolution but was achieved within 30 min once loading of the hydroxamate was started. With the reduced hydroxamate resin, high ^{89}Zr elution yields were achievable in the first 0.5 mL 1M oxalic acid (75 ± 18 %) from the trapped ^{89}Zr. This yield provided 468 ± 300 MBq of ^{89}Zr per mL of 1 M oxalic acid, an improvement from earlier purifications with the larger foil and resin.

Radiolabeling of monoclonal antibodies with the purified ^{89}Zr from the thick target did not result in good radiolabeling yields. On average, the radiolabeling yield of DFO conjugated mAb ranged between 8 – 60%, with an average yield of 39 %. Here, as previously discussed in section 3.2.1 we decided to reduce the thickness of the foil from a new ^{89}Y source with lower iron content per weight. With bombardment conditions 4 and 5 (Table 3.5) 69 ± 19% of the ^{89}Zr trapped on the 100 mg of hydroxamate resin was eluted in 0.5 mL 1M oxalic acid. This resulted in a high concentration of ^{89}Zr (511 ± 40 MBq/mL). The changes in ^{89}Y foil staring material resulted in ^{89}Zr with high chemical purity, a conclusion based on successful radiolabeling (to be discussed in section 3.2.3). Additional elutions with 0.5 mL of 1 M oxalic acid were successful with 80 ± 14% of the trapped ^{89}Zr eluted from the hydroxamate resin. The activity concentration of these additional elutions was ~115 MBq/mL. Based on radiolabeling conditions described by Vosjan et al, [^{89}Zr]; (185 – 912 MBq/ mL) further elutions were not performed [85]

Table 3.5 Purification yields for the different ^{89}Y bombardment conditions

Bombardment condition	1	2	3	4 & 5
Starting material Ø [mm]	25.4	25.4	10	10
Thickness [mm]	1.016	1.016	1.016	0.254
Mass [g]	2.3	2.3	0.356	0.089
^{89}Zr in 1st elution [%]	43 ± 27	76 ± 13	75 ±18	69 ± 19
^{89}Zr in 1st elution [MBq]	46 ± 8	549 ± 303	234 ± 150	284 ± 114
1st elution volume [mL]	1.0	3.0	0.5	0.5
^{89}Zr [MBq/mL]	54 ± 17	305 ± 274	468 ± 300	511 ± 40
Total ^{89}Zr at time of purification [MBq]	99 ± 40	549 ± 303	251 ± 138	337 ± 137

3.3.3 Radiolabeling Optimization of mAb with ^{89}Zr

Studies by Lee JH et al. evaluated the impact of the amount of antibody injected on biodistribution, tumour uptake and clearance [119]. While this may well vary according to the mAb being studied, in general an injected mAb dose of 30-50 µg is considered optimal for small animal imaging and for µPET imaging the optimal injected dose is 3.7 – 7.4 MBq. Consequently, the ideal specific activity of the purified radiolabeled mAb should be between 0.074 – 0.25 MBq/µg. Trastuzumab was conjugated with DFO at both 1:3 and 1:6 antibody to DFO ratios. Initial radiolabeling procedures to assess yield and purity were analysed with iTLC. To optimise radiolabeling conditions, the amount of purified ^{89}Zr (100 – 200 µL, 20 – 100 µL or < 20 µL); the chelate to Trastuzumab radio (3 or 6) and the amount of conjugated DFO-Trastuzumab (500 µg, 200 µg or < 50 µg) were changed. The radiochemical conversion yield (RCY) assessed by iTLC and predicted specific activity (MBq/µg) was calculated based on the starting Trastuzumab amount and RCY (Table 3.6). Based on the results from the radiolabeling studies, the optimal conditions for radiolabeling Trastuzumab to yield an appropriate specific activity were to use 200 µL of purified ^{89}Zr and 200 µg of DFO:Trastuzumab. A DFO:Trastuzumab ratio of 6:1 provided a higher RCY compared to 3:1. When assessing

immunoreactive fraction, both ratios were acceptable for imaging (> 99 % for 3:1 and > 96 % for 6:1) and as such for Trastuzumab radiolabeling a ratio of 6:1 was used. To push the limit of the number of chelators, Trastuzumab was conjugated with a 10-fold molar ratio of DFO. Immunoreactivity with the 10:1 DFO:Trastuzmab conjugate was poor (< 60%). Optimization of DFO: mAb conjugation of novel antibodies was not permitted due to the limited amounts of antibody available and the high cost of customization. For E-cadherin antibody (EP700Y) and isotype control antibody (EPR25A) the DFO: mAb ratio was kept at 3:1 to ensure an acceptable immunoreactive fraction.

Table 3.6 Radiolabeling parameters and yields of ^{89}Zr-DFO-mAb

^{89}Zr (μL)	100 - 200					20 -100			< 20
DFO:mAb	3			6		3		6	3
mAb [μg]	500	200	< 50	500	200	200	< 50	200	< 50
RCY	17%	59%	5%	66%	37%	56%	24%	18%	4%
SA [MBq/μg]	0.02	0.09	0.03	0.06	0.16	0.10	0.03	0.10	0.04

3.3.4 Effect of Injected Dose of ^{89}Zr Radiolabeled mAb

To test the effect of injected dose on tumour uptake and biodistribution; 2 x 500 μg of DFO-Trastuzumab (ratio DFO:mAb, 6:1) were incubated with 174 and 186 MBq of purified ^{89}Zr (200 μL). After a 60 min room temperature incubation the reactions yielded individual RCY of greater than 99 %. The two radiolabeling reactions were pooled and purified with a PD-10 desalting column in PBS. iTLC results of the purified ^{89}Zr-DFO-Trastuzumab was greater than 99% (Figure 3.2), final specific activity determined by SEC HPLC was 0.32 MBq/μg with an ^{89}Zr concentration of 0.088 MBq/μL. Since the final product was in a volume and buffer appropriate for murine injections, further concentration using a molecular weight filter was not used. SKOV-3 tumour bearing mice were grouped into three groups receiving differing doses of ^{89}Zr-DFO-Trastuzumab (Table 3.7).
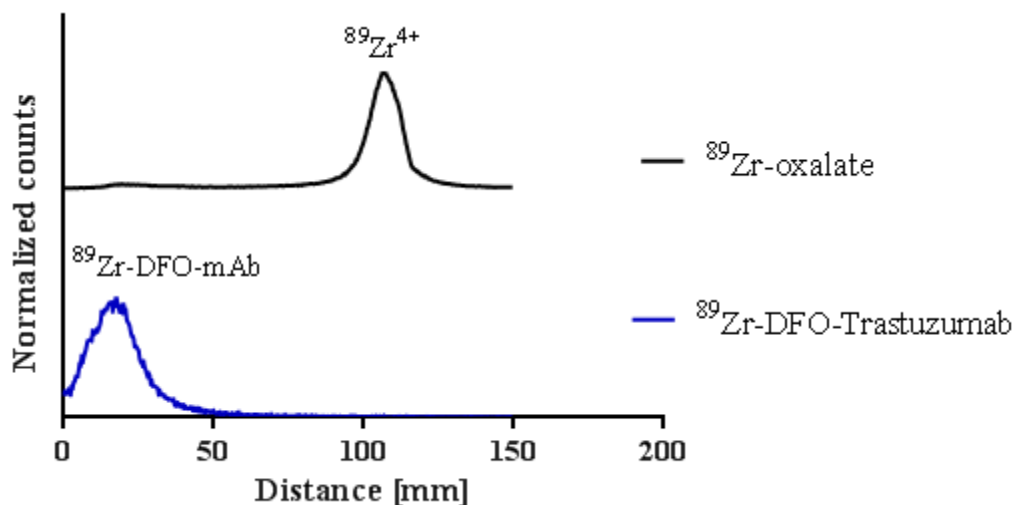
Figure 3.2 Normalized iTLC plot of ^{89}Zr-DFO-Trastuzumab radiolabeling yield; plot of free ^{89}Zr was included as a control.

Table 3.7 Injected dose and biodistribution of ^{89}Zr-DFO-Trastuzumab. Data is presented as mean ± SD, %ID/g, n ≥ 3. Significant differences compared to group 1, denoted with *, p<0.0001.

^{89}Zr-DFO-Trastuzumab	Group 1 (33 µg)	Group 2 (18 µg)	Group 3 (4 µg)
MBq	10.7 ± 0.24	5.7 ± 0.24	1.35 ± 0.06
µg	33.44 ± 0.75	17.82 ± 0.76	4.22 ± 0.18
Blood	3.69 ± 2.08	1.09 ± 0.27	0.19 ± 0.05
Intestine	3.8 ± 0.95	5.36 ± 0.89	3.78 ± 1.4
Spleen	44.11 ± 5.26 *	77.46 ± 9.24 *	119.38 ± 40.87 *
Kidneys	3.04 ± 0.69	2.87 ± 0.25	3.24 ± 0.21
Liver	5.16 ± 0.82	8.07 ± 0.77	14.47 ± 1.23
Heart	1.45 ± 0.48	1.38 ± 0.1	1.46 ± 0.1
Bone	7.47 ± 0.9	10.65 ± 0.5	14.11 ± 1.49
Muscle	0.66 ± 0.23	0.94 ± 0.27	0.59 ± 0.11
Tumour	19.29 ± 14.08	16.33 ± 7.49	11.79 ± 6.88

Absolute tumour uptake did not differ between the groups; this was also evident in all other organs except for the spleen. There was significant higher %ID/g in spleen uptake in groups 2 (18 µg; 77.46 ± 9.24 %ID/g) and 3 (4 µg; 119.38 ± 40.87 %ID/g) compared to group 1 (33 µg; 44.11 ± 5.26 %ID/g); ($p < 0.0001$). There was also a significant higher uptake in group 3 compared to group 2 ($p < 0.0001$). There was a trend between the groups and %ID/g of blood and tumour with a decrease in uptake with decreasing injected dose (Figure 3.3). Intestine, kidney, heart and muscle uptake remained relatively the same between the groups. Liver and bone all exhibited an increase in %ID/g with decreasing injected dose, however no statistical differences were determined between the groups in the liver and bone.
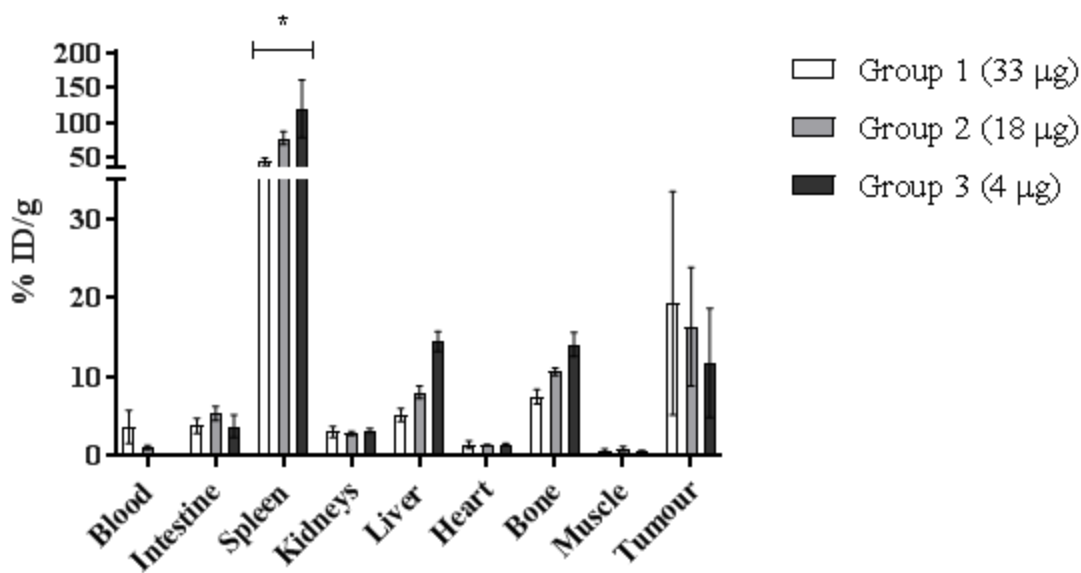
Figure 3.3 Biodistribution of ^{89}Zr-DFO-Trastuzumab at day 3. Uptake of ^{89}ZDFO-Trastuzumab in the blood, tumour and organs of interest is expressed as %IDg. Star (*) indicates significant difference ($p < 0.0001$) between all three groups.

Assessing tumour to organ ratios; the tumour to blood ratio significantly increased between group 3 (4 µg) and groups 1 and 2; ($p < 0.0001$). Group 2 (18 µg) had higher but not significant tumour uptake than group 1 (33 µg). Despite the differences observed with absolute spleen uptake, no differences were observed for tumour to spleen ratio. Similarly, to the results using

[111]In-Trastuzumab, the trend of increased %ID/g in the liver and spleen was seen with the decrease in antibody dose.

3.3.5   E-cadherin Results

Conjugation of the anti-E-cadherin antibody EP700Y and rabbit isotype control EPR25A with DFO was performed at pH 8.9 and ambient temperature. SEC HPLC analysis showed intact conjugated mAb post purification and no aggregation was evident. The two conjugated mAbs were successfully radiolabeled with 200 µL purified ^{89}Zr (131 and 132 MBq). iTLC analysis of the reactions showed greater than 99 % RCY. Post PD-10 purification and concentrations with molecular weight filters resulted in an isolated yield of 97.6 MBq and 103.6 MBq for ^{89}Zr-DFO-EP700Y and ^{89}Zr-DFO-EPR25A respectively. Specific activity was determined by SEC HPLC with 1.29 MBq/µg for ^{89}Zr-DFO-EP700Y and 1.70 MBq/µg for ^{89}Zr-DFO-EPR25A.

MCF7 and T47D tumour bearing mice were injected with 10.18 ± 2.17 MBq corresponding to 7.9 ± 1.7 µg of ^{89}Zr-DFO-EP700Y or 10.69 ± 4.01 MBq corresponding to 6.3 ± 2.4 µg of ^{89}Zr-DFO-EPR25A. µPET CT imaging acquired at day 1 showed typical antibody biodistribution as seen in uptake in liver, spleen, heart and tumour (Figure 3.4). The intensity of uptake in the liver and spleen increased in the EP700Y group and tumour uptake appeared to decrease. An increase in spleen uptake was observed in the images from day 1 to day 5 in the EPR25A group while tumour and liver uptake appeared to be maintained. As with any radiolabeling of ^{89}Zr to DFO demetallation of the ^{89}Zr from the DFO is inevitable in mice [131]; this was evident with the increase in bone uptake from day 1 to 5. Biodistribution at day 3 showed no statistical difference between the two groups. Tumour uptake as expressed as %ID/g of EP700Y in the MCF7 tumour was 8.58 ± 1.13 and 8.56 ±0.32 for the T47D tumour. There was higher uptake of EPR25A in the MCF7 tumour: 12.02 ± 4.03 and T47D tumour: 9.24 ± 1.88 for T47D compared to EP700Y. Between day 3 and 5 there were no statistical differences within each group except for spleen. An increase in spleen uptake was observed with the EP700Y from day 3 (81.3 ± 18.7 %ID/g) to 5 (93.3 ± 8.4 %ID/g) (p = 0.0004). At day 5 tumour uptake of EP700Y decreased with the MCF tumour: 6.83 ± 1.31 %ID/g, while T47D tumour uptake remained stable: 8.56 ± 3.29 %ID/g. The low uptake of the EP700Y in comparison to the control EPR25A could be due to the decreased binding affinity as assessed with the immunoreactivity or just an effect of the antibody

uptake in a tumour due to the enhanced permeability effect. Similar to results obtained from ^{111}In radiolabeling of EP700Y and EPR25A, uptake of the EP700Y was not significantly higher than uptake of EPR25A.
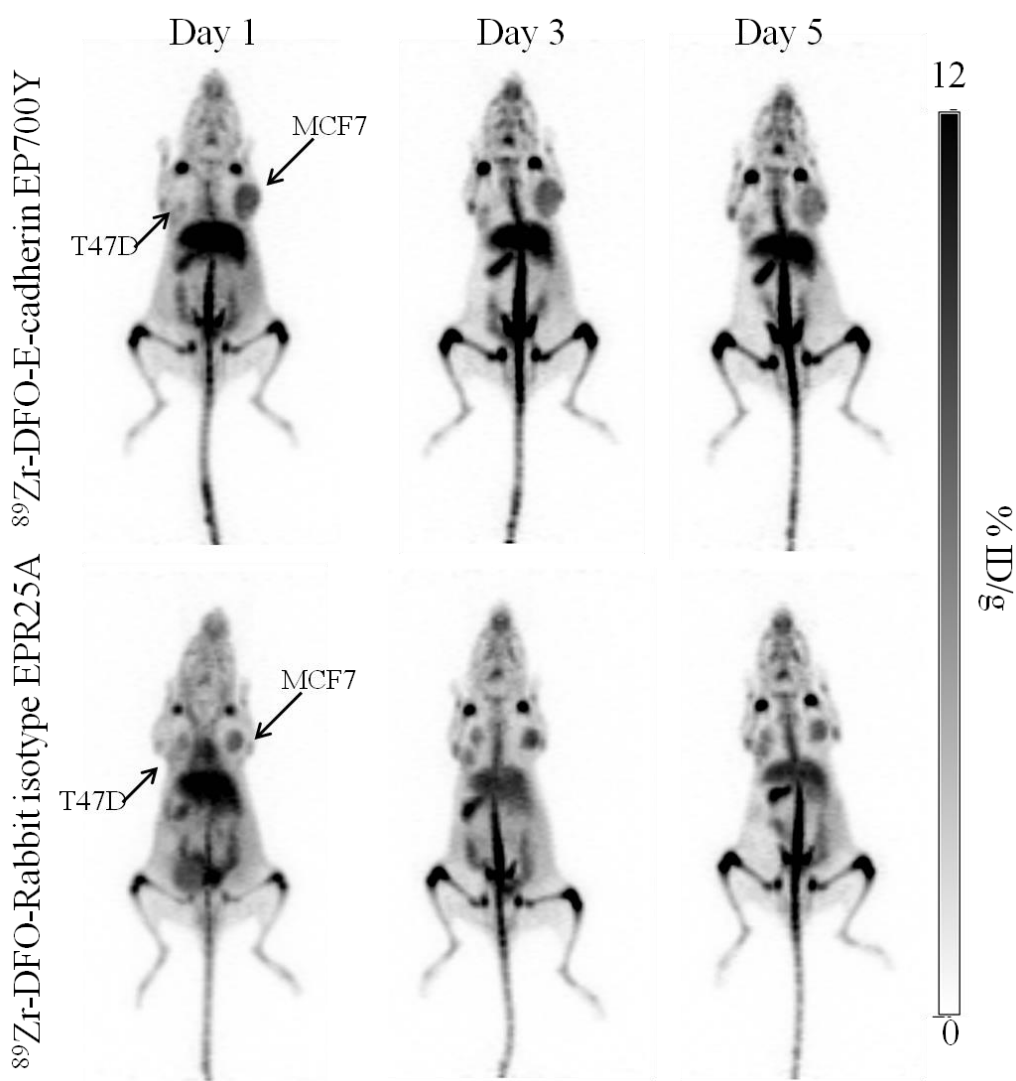
Figure 3.4 Maximum intensity PET images of [89]Zr-DFO-EP700Y (above) or EPR25A (below) at day 1, 3 and 5. The T47D tumour was present on the left shoulder and the MCF7 tumour on the right shoulder. Scale bar indicates %ID/g

3.4 Conclusion

We have demonstrated production and purification of ^{89}Zr using a solid target approach on a clinical cyclotron. Systemically optimizing the starting material quantity and beam parameters improved the purity of the ^{89}Zr reduced long-lived impurities and permitted high radiolabeling yields of monoclonal antibodies. We demonstrated ^{89}Zr radiolabeling and μPET imaging of Trastuzumab targeting HER 2 and novel mAbs targeting E-cadherin. Reducing the injected dose of ^{89}Zr Trastuzumab showed no difference in tumour uptake and overall biodistribution. A trend of higher uptake as injected dose per gram was observed in the liver and spleen with decreasing Trastuzumab dose. Tumour uptake of radiolabeled E-cadherin mAb was not significantly higher than tumour uptake of an isotype control IgG.

Chapter 4: ^{89}Zr Liquid Target Production for Immuno PET

4.1   Introduction

The production of ^{89}Zr on a clinical cyclotron has improved the opportunities for high resolution PET imaging of mAbs. One limitation with conventional ^{89}Zr production is the requirement for an expensive and dedicated solid target station.   In cyclotron centres with established ^{18}F production, the integration of a solid target (ST) may not feasible. Producing radiometals via a liquid target (LT) system could significantly expand the availability of ^{89}Zr and accelerate clinical development. In collaboration with TRIUMF [109], and from the development by others [108] the feasibility of producing ^{89}Zr via a LT system has been demonstrated. However, the feasibility of LT ^{89}Zr for radiolabeling and imaging of mAbs has not been reported. Herein we describe the feasibility of using LT produced ^{89}Zr for radiolabeling and *in vivo* diagnostic PET imaging of an immunoconjugate. In addition to comparing the production and purification yields of ^{89}Zr-(LT) or ^{89}Zr-(ST), we compare the radiolabeling yields, specific activity and *in vivo* biodistribution of an immunoconjugate, p-SCN-Bn-Deferoxamine-Trastuzumab (DFO-Trastuzumab), radiolabeled with ^{89}Zr produced either via the LT or ST systems.

4.2   Materials and Methods

The liquid target material ^{nat}Y(NO$_3$)$_3$·6H$_2$O (99.9%) was purchased from Alfa Aesar (Ward Hill, MA, USA). ^{89}Y metal foils (99.9%, 0.254 mm thickness) were purchased from American Elements (Los Angeles, CA, USA). Ultrapure HCl (TraceSELECT$^®$), and sodium oxalate (99.99% trace metal basis) were purchased from Sigma-Aldrich (Oakville, ON, Canada). Ultrapure nitric acid (TraceMetal™ grade) was obtained from Fisher Scientific (Ottawa, ON, Canada). A Millipore system (Direct-Q$^®$ 3UV with Pump, 18 MΩ cm^{-1}) provided ultrapure water. The bifunctional chelator p-SCN-Bn-Deferoxamine (DFO) was purchased from Macrocyclics (Dallas, TX, USA). Dimethyl sulfoxide (DMSO) used for chelator stock solutions was of molecular biology grade (>99.9%) obtained from Sigma-Aldrich. All other chemicals were analytical grade and used without further purification.

The radiolabeling of bioconjugates was monitored using silica-impregnated instant thin-layer chromatography paper (iTLC-SG) (Agilent Technologies, Santa Clara, CA, USA) and analyzed on a Ray Test miniGita with Beta GMC detector radio-TLC plate reader using TLC control Mini Ginastar software (Straubenhardt, Germany). GE Healthcare Life Sciences PD-10 desalting columns (GE Healthcare, United Kingdom, MW < 5000 Da filter) and 50 kDa molecular weight cutoff filters (Amicon ultracentrifuges, Ultracel-50: regenerated cellulose, Millipore Corp., Billerica, MA, USA) were used for radiolabeling purification. High performance liquid chromatography (HPLC) analyses of purified ^{89}Zr-DFO-Trastuzumab were carried out using a size-exclusion chromatography (SEC) column (Phenomenex, BioSep-SEC-s-3000) on an Agilent™ system equipped with a model 1200 quaternary pump, a model 1200 UV absorbance detector (set at 280 nm), and a Bioscan (Washington, DC, USA) NaI scintillation detector. The radiodetector was connected to a Bioscan B-FC-1000 flow-count system, and the output from the Bioscan flow-count system was fed into an Agilent 35900E interface, which converted the analog signal to a digital signal. The HPLC buffer was an isocratic gradient of 0.1 M sodium phosphate monobasic dihydrate, 0.1 M sodium phosphate dibasic dodecahydrate, 0.1 M sodium azide and 0.15 M sodium chloride (pH 6.2–7.0).

Radionuclidic purity of the irradiated salt solutions was determined by gamma spectroscopy using a Canberra Inc. (Meriden, CT, USA) N-type Co-axial high-purity germanium detector (HPGe). Radioisotopic dilution, immunoreactivity and biodistribution samples were counted on a Perkin Elmer (Waltham, MA, USA) Wizard 2 2480 automated gamma counter.

4.2.1 ^{89}Zr Production

Yttrium(III) nitrate solutions were prepared per previously described protocol [109]. Briefly, ^{nat}Y(NO$_3$)$_3$·6H$_2$O (37.5 g) was dissolved in ultrapure water (22.7 g) and concentrated nitric acid (2.30 mL) by stirring at 40°C overnight to give Y-nitrate in ~0.8 M HNO$_3$ (density = 1.48 ± 0.01 g/mL, metal concentration = 0.203 ± 0.002 g/cm^3). Experiments were performed on TRIUMF's TR13 cyclotron (Vancouver, BC, Canada) (Advanced Cyclotron Systems Inc, Richmond BC, Canada), a 13 MeV self-shielded, negative hydrogen ion cyclotron. Irradiations were performed in a siphon niobium-body target with an internal target volume of 1.48 mL and an expansion chamber with a volume of 1.77 mL. The target was designed in consideration of work performed

by Stokely [132].   The beam window used was a Havar® foil 38 μm thick (Goodfellow Corporation Coraopolis, PA, USA). The oval shaped target chamber was irradiated in the bottom half with a circularly collimated Gaussian beam 10 mm wide, while the top half was sufficient in volume to accommodate produced gasses caused by radiolysis. Loading and unloading of the target was performed using an automated system. The target chamber was filled with solution from the bottom using a syringe pump. A bolus detector positioned past the target chamber at the top was used to verify that the target chamber had been filled. This routinely required pushing approximately 6.2-6.5 mL of solution into the system. Once the bolus detector was tripped, an additional 1 mL of solution was pushed into the system to act as a flush upon unloading of the target. After the target chamber was loaded, the expansion chamber was pressurized with 300 to 350 psi pressure helium in order to increase the boiling point. All valves to the target were then shut in preparation for irradiation. The target and loading system used for these experiments have been previously described [133].   The irradiations were performed in several replicates using proton beams of approximately 10 μA for 60 or 240 min. Initial runs were irradiated for 60 min and increased for *in vivo* studies. The target solution was unloaded with pressurized helium and collected into a vial in a hot cell. This unloading procedure resulted in target solution volumes of 5-7 mL.

As mentioned in the previous chapter, yttrium foil sheets (0.254 mm thick) were water jet cut into 10 mm diameters (0.089 ± 0.002 g). These foils were sandwiched between an aluminum ring and backing and loaded onto the solid target holder. Irradiation of solid target production of ^{89}Zr was achieved on a TR19 cyclotron at the BC Cancer Agency, Vancouver, BC, Canada. Proton beam energy of 13.8 MeV with beam current of 14 μA irradiated a solid ^{89}Yfoil (10 mm Ø, 0.254 mm thick, 99.9% purity). Irradiation beam time was adjusted to match experimental requirements and operational constraints and the integrated current varied.

4.2.2 ^{89}Zr Purification

The hydroxamate resin used for the purification of liquid or solid target ^{89}Zr was prepared as described by Holland et al [100]. Before ^{89}Zr purification, the hydroxamate resin was packed between two frits in a 4 mL reservoir and activated with acetonitrile (8 mL) MeCN, washed with H_2O (15 mL) and conditioned with 2 M HCl (4 mL).

The irradiated ST was dissolved in 6 M HCl (2 mL) in a closed system and for 1 h. The irradiated LT solution was purified at least 1 h or the equivalent of irradiation time after end of beam to reduce the amount of ^{13}N and ^{11}C coproduced during the irradiation. The ^{89}Zr solutions were diluted to 2 M HCl by adding 4 mL of H_2O for the ST; 1.4 mL of 10 M HCl was added to the LT with a further addition of 2 M HCl (5 mL). ST and LT solutions were loaded onto the conditioned hydroxamate resins of 100 and 50 mg, respectively. Once the ^{89}Zr was trapped the resins were washed with 2 M HCl (10 mL) to further remove any ^{89}Y and other impurities; subsequently washed with H_2O (10 mL) and air dried. The ^{89}Zr was eluted from the resins with 1.0 M oxalic acid in aliquots of 0.5 mL.

4.2.3 Radiolabeling of *p*-SCN-Bn-DFO-mAbs

Trastuzumab (Herceptin, Genentech, San Francisco, CA) was purified to remove α-α-treholase dehydrate, L-histadine, and polysorbate 20 additives with centrifugal filter units with a 50 kDa molecular weight cutoff and washed with PBS (pH 7.4) at 4000 g for 20 min four times. The final spin was washed with PBS pH 8.9-9.1. Following a similar procedure to Vosjan et.al., [85] purified Trastuzumab (2 mg) was incubated with p-SCN-Bn-desferoxamine (DFO)(60 μg) at room temperature over night with a DFO:Trastuzumab molecular ratio of 6:1 in PBS pH 8.9-9.1. Conjugated Trastuzumab (DFO-Trastuzumab) was then purified using the centrifugal filter technique described above and washed once with 5 mg/mL dihydrobenzoic acid, in 0.25 M sodium acetate solution. Varying quantities (50 or 200 μL) of ^{89}Zr-oxalate were incubated with either 22.5 or 90 μL of 2 M Na_2CO_3 to adjust the pH of the ^{89}Zr to pH 6.5 – 7.5 at room temperature for 3 min. To this neutralized ^{89}Zr solution, DFO-Trastuzumab (50 or 200 μg) was added and the volume adjusted to obtain at least a concentration of 0.2 μg/μL of DFO-Trastuzumab with PBS (pH 7.4). The reaction was allowed to progress for 60 min at room temperature, and radiolabeling yield of the reaction was assessed on iTLC-SG using 50 mM DTPA (pH 7) as mobile phase and counted on a TLC plate reader. The ^{89}Zr-DFO-Trastuzumab was purified using size exclusion PD-10 desalting columns with PBS pH 7.4 and concentrated using 50 kDa molecular weight cut off filters. For optimization experiments, specific activity was estimated based on radiochemical yield from iTLC results. Specifically, for the *in vivo* study; 200 μL of ^{89}Zr(ST) or ^{89}Zr(LT) corresponding to 78.4 and 42.4 MBq, respectively, were

neutralized with 90 µL 2 M Na$_2$CO$_3$ and then incubated with 200 µg of DFO-Trastuzumab, the final volume was adjusted to 1.0 mL with PBS. Final radiochemical purity and specific activity were determined using size–exclusion HPLC.

4.2.4 Chelate Number with Radiometric Isotopic Dilution

The number of accessible DFO chelates conjugated to trastuzumab was determined by radiometric isotopic dilution assays following a method described by Deri *et al* [115]. Briefly, a stock solution of 1.4 mM ZrCl$_4$ in 1 M oxalic acid was prepared. Approximately ~400 µCi of ^{89}Zr (200 µL, in 1M oxalic acid) was added to 200 µL of the stock 'cold' Zr^{4+} solution. This ^{89}Zr[Zr] mixture was neutralized to pH 7 with 2 M Na$_2$CO$_3$, 1 M oxalic acid, and PBS pH 7.4 to create a working solution with a final Zr^{4+} concentration of 0.23 mM. Triplicate solutions of DFO-Trastuzumab were prepared by pipetting 30 µL of antibody in PBS (48 µg, 0.3 nmol). Negative controls using 30 µL of PBS were also prepared in triplicate. Aliquots of 20, 25, and 30 µL of the ^{89}Zr[Zr] working solution were added to each tube containing DFO-Trastuzumab or PBS. The solutions were incubated at ambient temperature with gentle mixing overnight, and subsequently quenched with a volume of 50 mM DTPA (pH 7) equal to 1/9 of the reaction volume. The reaction mixture was left to incubate for 15 minutes to scavenge any non-specifically bound Zr^{4+}. Each reaction was then analyzed by iTLC-SG using 50 mM DTPA (pH 7) as mobile phase. Strips were cut in half, each placed separately in test tubes, and counted on the calibrated gamma counter to determine the extent of radiolabeling. The average number of chelates per mol of antibody was calculated by dividing the cpm of the bound ^{89}Zr (Rf =0) by the cpm of the unbound ^{89}Zr (Rf >0.5) and multiplying that by the number of moles (n) of free Zr^{4+} divided by moles of DFO-Trastuzumab.

4.2.5 *In vitro* Immunoreactivity Assay

Immunoreactivity fractions of radiolabeled Trastuzumab with ^{89}Zr either from the ST or the LT were determined according to the Lindmo cell-binding assay [134]. HER2-positive SKOV-3 cells were suspended at different concentrations (0.4 to 4.5 x 10^6 cells/mL in PBS). Either ^{89}Zr(ST)-DFO-Trastuzumab or ^{89}Zr(LT)-DFO-Trastuzumab (diluted in 1% PBS-BSA at 0.5 MBq/mL) were added to each tube in triplicates. After 1 h incubation at ambient temperature and

under gentle agitation, cells were centrifuged and washed twice with PBS. The binding and unbound fractions of the radiolabeled antibodies were determined for each sample using a gamma counter (with background and decay correction). Immunoreactive fractions were estimated by linear regression analysis of total/bound activity against 1/[cell concentration].

4.2.6 µPET/CT Imaging and Biodistribution

All animal experiments were performed at the Animal Resource Centre of the BC Cancer Agency Research Centre in accordance with the institutional guidelines of the University of British Columbia Animal Care Committee (Vancouver, BC, Canada) and under the supervision of authorized investigators.

Female immunodeficient NOD.Cg-Prkdc^{scid} Il2rg^{tm1Wjl}/SzJ (NSG) mice (obtained from an in-house breeding colony) were subcutaneously injected with 8 x 10^6 SKOV-3 cells in matrigel (BD Bioscience) on the right flank. Mice were anaesthetised with isoflurane (2% in O$_2$) and injected via tail vein with either ^{89}Zr(ST)-DFO-Trastuzumab (4.0 ± 0.3 MBq) or ^{89}Zr(LT)-DFO-Trastuzumab (3.4 ± 0.2 MBq), 2 weeks after SKOV-3 cell inoculation (n = 3 per group). Each mouse underwent a CT scan for attenuation correction followed by a µPET acquisition, acquired 1, 3 and 5 days post-injection using a Siemens Inveon microPET/CT scanner (Siemens Medical Solutions, Knoxville, TN, USA) and under anesthesia (2% isoflurane-O$_2$). To acquire approximately the same counts for PET images the counting time was adjusted to the injected activity (20 min scan for ^{89}Zr(ST)-DFO-Trastuzumab and 24 min scan for ^{89}Zr(LT)-DFO-Trastuzumab). Images were reconstructed using the 3-dimensional ordered-subsets expectation maximization (OSEM3D, 2 iterations) followed by a fast maximum a priori algorithm (FastMAP: 18 iterations) and attenuation corrected based on the CT image.

At day 5 post injection of the ^{89}Zr-DFO-Trastuzumab, mice were euthanized by inhalation of isoflurane followed by CO$_2$. Blood was withdrawn by intracardiac puncture, and then tumours and organs of interest were harvested, washed in PBS and weighed after drying. Activity of each sample was measured by a gamma counter with decay correction. The activity uptake was expressed as a percentage of the injected dose per gram of tissue (%ID/g). Statistical analyses for

biodistribution data were performed using GraphPad Prism (version 7). *P* values were calculated using ANOVA and valued < 0.05 were considered statistically significant.

4.2.7   Production Results

^{89}Zr (ST) production on the TR 19 was achieved with an average current of 14.6 µA, with integrated doses ranging from 631 to 2112 µA·min due to the differences in irradiation times and days. Differences in integrated currents were primarily due to the scheduling time for manual target loading and retrieval. Thus, beam time parameters for the ST were modified to ensure sufficient ^{89}Zr at the time of purification. Shorter runs where purification was scheduled the same or within one day of the irradiation were run with an average integrated dose of 755 ± 124 µA·min and resulted in 456 ± 116 MBq of ^{89}Zr-(ST) produced decay corrected to end of beam (EOB, n = 9). Longer irradiations, typically 130 min, where performed when purification was scheduled for at least 24 h post irradiation and were run with an average integrated dose of 1797 ± 379 µA·min and resulted in 739 ± 229 MBq ^{89}Zr decay corrected to EOB (n = 6) (Table 4.1).

Due to the 100% natural abundance of ^{89}Y, irradiation of the Y(NO$_3$)$_3$ solution produced solely ^{89}Zr through the ^{89}Y(p,n)^{89}Zr reaction. A one hour irradiation of Y(NO$_3$)$_3$ solution produced on average 37 ± 17 MBq of ^{89}Zr (n = 9 decay corrected to EOB); while this was a sufficient amount of activity to test radiolabeling chemistry, it is likely below the lower limit needed to prepare an antibody conjugate of high enough specific activity for a comprehensive pre-clinical imaging study. To produce sufficient yields of ^{89}Zr to complete a pre-clinical imaging study, four hour irradiations were performed. A 4 h irradiation produced an average of 95 ± 38 MBq of activity (n = 4, decay corrected to EOB, Table 1). The radionuclidic purity of the crude irradiated LT solution 48h after EOB and dissolved ST 72 h after EOB were found to be > 99.0%, confirmed by gamma spectroscopy (Figure 4.1).
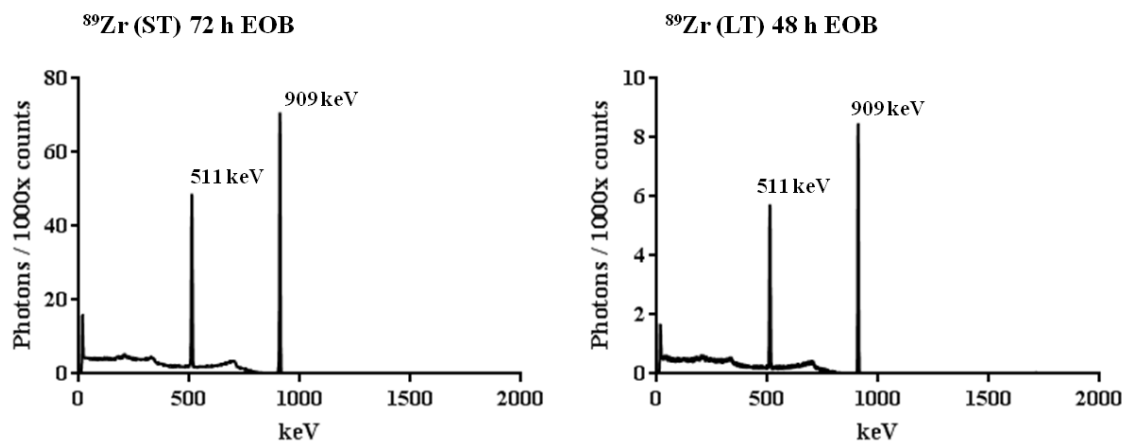
Figure 4.1 Spectrums of the gamma-ray emissions observed from unpurified samples of ^{89}Zr-(ST) left and ^{89}Zr-(LT) right, acquired 72 h (ST) and 48 h (LT) post EOB.

Table 4.1 Summary of ^{89}Zr production parameters for solid and liquid irradiations. Results are given as mean ± SD.

	Solid target		Liquid target	
Cyclotron	TR 19 BCCA		TR 13 TRIUMF	
Integrated dose [μA·min]	755 ± 124	1797 ± 379	639 ± 133	2370 ± 645
Number of runs	9	5	9	4
Proton energy [MeV]	13.8	13.8	12	12
Beam current [μA]	14.5 ± 4.2	14.0 ± 3.8	11.1 ± 2.7	10.6 ± 2.5
Beam time [min]	60 ± 28	137 ± 48	58 ± 4	224 ± 26
EOB Yield [MBq]	456 ± 116	715 ± 247	37 ± 17	95 ± 38
Saturated Yield [MBq/μA]	3990 ± 642	2879 ± 1074	407 ± 160	271 ± 50
Purified ^{89}Zr at EOB [MBq]	339 ± 89	507 ± 237	20 ± 13	76 ± 26

Table 4.2 Comparison of ^{89}Zr liquid target production yields to literature. Data is presented as mean ± SD.

	Liquid target	
	TRIUMF	Pandey et al. [105]
Yttrium [g]	0.3	0.28
Proton energy [MeV]	12	14
Beam current [μA]	10.6 ± 2.5	40
Beam time [min]	224 ± 26	120
EOB Yield [MBq]	95 ± 38	349 ± 49
Yield [MBq/μA·h]	2.3 ± 0.4	4.4 ± 0.6

4.2.8   Purification Results

Purification of the ^{89}Zr from the ^{89}Y target material was achieved with solid phase separation with a hydroxamate resin for both ST and LT productions. Extraction and purification of the ST irradiated foil was often performed at least 24 h after EOB. Due to the current set up at BCCA, manual extraction of the foil was required and performed when the field from the target was acceptable and around daily clinical ^{18}F production runs. Purification of ^{89}Zr-(ST) is achievable within 30 min after the complete dissolution of the irradiated foil using 100 mg of the hydroxamate resin. As described in the methods, the dissolved ST solution was diluted to 2 M HCl and loaded onto the resin, washed with 2 M HCl and H_2O and eluted with aliquot of 0.5 mL of 1 M oxalic acid. The activity from the first elution from ST purification often yielded sufficient activity required for optimizing radiolabeling conditions and for *in vivo* studies. On average, 57 ± 17% of radioactivity from the irradiated foil was eluted in the first 0.5 mL elution from the hydroxamate resin resulting in 281 ± 94 and 359 ± 145 MBq decayed to EOB for the lower and higher integrated dose runs respectively. Additional elutions resulted in the recovery of 71 ± 16 %, with a total yield of 338 ± 89 and 507 ± 237 MBq for the lower and higher integrated dose runs in a total volume of 1.0 - 1.5 mL. For the purification of the *in vivo* study, the activity and concentration in the first elution was sufficient for radiolabeling and so an additional elution was not performed.

Purification of ^{89}Zr-(LT) required the addition of 10 M HCl (1.4 mL) to the irradiated nitric acid solution with an addition of 2 M HCl (5 mL) in order to adjust the acid concentration to 2 M HCl prior to loading the solution onto a 50 mg hydroxamate resin following procedures outlined previously by our group. To reduce radiation exposure due to the presence of co-produced ^{13}N and ^{11}C, purification of the LT solution started 1 or 4 hr post EOB, for a 60 or 240 min irradiation, respectively. Separation efficiency of the LT solution was 93 ± 6%, resulting in 20 ± 13 MBq decay corrected to EOB for a 60 min irradiation. By increasing the irradiation time to 4 hours, 66 ± 26 MBq of ^{89}Zr-(LT) was isolated (76 ± 26 MBq ^{89}Zr decay corrected to EOB).

Table 4.3 ^{89}Zr production and purification parameters and results for *in vivo* study.

| | *In vivo* imaging study | |
	Solid	Liquid
Dose [µA·min]	1500	2830
Energy [MeV]	13.8	12
Current [µA]	10.5	11.7
Beam time [min]	143	243
EOB Yield [MBq]	799	128
Saturated Yield [MBq/µA]	3657	312
Purified ^{89}Zr at EOB*	349	110
^{89}Zr for radiolabeling [MBq]	234	101

*Purified ^{89}Zr based on 1st elution

4.2.9   Radiolabeling

Trastuzumab was incubated with *p*SCN-Bn-DFO overnight at pH 9.0; SEC HPLC analysis showed intact DFO conjugated Trastuzumab (DFO-Trastuzumab) post purification and no aggregation was evident. As determined in chapter 3, the optimal conditions to obtain a specific activity (SA) suitable for *in vivo* µPET imaging was to use 200 µL of purified ^{89}Zr(ST) with 200 µg of DFO conjugated mAb. To optimise radiolabeling with ^{89}Zr(LT) and to provide the best comparison between ST and LT radiolabeling a range of volumes of purified ^{89}Zr(ST) were neutralised with the appropriate amount of 2 M Na$_2$CO$_3$. To these varying conditions, 200 µg of

conjugated DFO-Trastuzumab in PBS was added. Radiolabeling of the conjugated mAb was achieved at ambient temperatures at pH 7.0 within 1 h. Radiolabeling efficiency was assessed by iTLC and estimated SA was calculated based on the radiolabeling efficiency divided by the amount of starting DF-mAb; this provided a crude and reasonable estimation of SA (Table 4.4). For reactions using 200 µL of ST ^{89}Zr and 200 µg of DFO-Trastuzumab, a radiolabeling yield of 37% with a predicted SA of 0.16 MBq/µg was obtained. To match the amount of ^{89}Zr activity in a typical LT radiolabeling reaction using 200 µL of ^{89}Zr-oxalate, the volume of ^{89}Zr(ST) was decreased proportionally. Using 50 µL of ^{89}Zr(ST)in the radiolabeling reaction further improved radiolabeling yield to 81% while SA decreased to 0.10 MBq/µg; however, the bioconjugate was still sufficient for imaging. Generally, lower starting volumes of ^{89}Zr(ST)-oxalate in the radiolabeling reaction resulted in higher radiochemical yields, presumably because the amount of metal impurities (e.g. Fe^{3+}) that may compete for DFO binding sites also decreased as total volume decreased. When comparing directly the radiolabeling efficiency of DF-mAb (200 µg) with either 200 µL of LT or ST ^{89}Zr, LT radiochemical yields were superior displaying 51 compared to 38% RCY, respectively, suggesting that ^{89}Zr-oxalate isolated from a LT may contain lower concentrations of metal impurities compared to ST ^{89}Zr-oxalate. Reducing the ^{89}Zr(LT) volume in the reaction did not provide a bioconjugate of sufficient SA for *in vivo* µPET imaging.

Table 4.4 Radiolabeling conditions of DFO-Trastuzumab with either ^{89}Zr ST or LT. Radiochemical yield (RCY) determined from iLTC and predicted specific activity (SA) based on RCY.

	Solid target (ST)		Liquid target (LT)	
^{89}Zr (µL)	200	50	200	50
1 M oxalic acid (µL)	90	22.5	90	22.5
mAb [µg]	200	200	200	50
RCY	37%	81%	51%	49%
SA [MBq/µg]	0.16	0.10	0.09	0.07

For the *in vivo* study, the number of chelates per DFO-Trastuzumab was first determined by radioisotopic dilution to yield an average of 2.6 ± 0.3 DFO chelates per mAb. In order to obtain the best radiolabeling potential using either ^{89}Zr-(LT) or ^{89}Zr-(ST), DFO-Trastuzumab (200 μg) was incubated with the same volume of 200 µL of ^{89}Zr (ST: 78.4 MBq, LT: 42.2 MBq). After 60 min, iTLC results from the crude reaction showed better radiolabeling with the ^{89}Zr-(LT) (55%) than ^{89}Zr-(ST) (33%). Following PD-10 purification and concentration of the radiolabeled Trastuzumab, iTLC of the final products showed 97% and 98% radiochemical purity for the ^{89}Zr-(ST) and ^{89}Zr-(LT) reactions, respectively. The predicted SA estimation based on iTLC was consistent with previous radiolabeling performed during the optimization process. By size-exclusion HPLC, the SAs for ST (0.12 MBq/μg) and LT (0.15 MBq/μg) were determined and suitable for μPET imaging. The final activity of purified ^{89}Zr-DFO-Trastuzumab products prepared for animal injections were: ST: 18.6 MBq and LT: 15.5 MBq. Quality control of the ^{89}Zr-DFO-Trastuzumab to ensure intact immunoreactivity was performed and a 95% immunoreactive fraction was found.

4.2.10 *In vivo* Results

μPET-CT images were performed at 1, 3 and 5 days post-injection (Figure 4.2). Images showed similar high uptake of the ^{89}Zr-DFO-Trastuzumab within the SKOV-3 tumors as early as day 1 post-injection. For ^{89}Zr-(ST)-DFO-Trastuzumab and ^{89}Zr-(LT)-DFO-Trastuzumab, a typical biodistribution profile of a radiolabeled immunoconjugate was observed with high liver, heart and spleen uptake. High contrast PET images were obtained for both, enabling clear visualization of the tumor xenografts. Also, tumor uptake increased over the 5 day period for both compounds. Notably as with most ^{89}Zr-DFO complexes in mice, demetallation of the ^{89}Zr was observed and increased over the progression of the study; evident by the visual increase in bone uptake [131].

Biodistribution data corroborated the PET imaging results. High tumor uptake expressed as percent of injected dose per gram of tissue (%ID/g) at day 5 were the same for both groups; ST: 25.22 ± 3.63 %ID/g and LT: 21.66 ± 3.90 %ID/g (Table 4.5). ^{89}Zr-(LT)-DFO-Trastuzumab exhibited lower uptake in the uterus, which may be attributed to differences in ovulatory cycle in the group of mice. Minor differences in spleen uptake were observed ($p < 0.001$) which could not

be explained by any aggregates as none were observed during the size-exclusion HPLC performed control quality after radiolabeling (data not shown). No statistical differences in other organs of interest were noticed between the two groups ($p > 0.05$). Both groups exhibited similar tumour-to-blood or tumour-to-non-target organ (liver, spleen, kidneys or heart) ratios (Figure 4.3). Imaging quality and biodistribution showed no noticeable differences suggesting [89]Zr-(LT) to be a suitable alternative to [89]Zr-(ST).
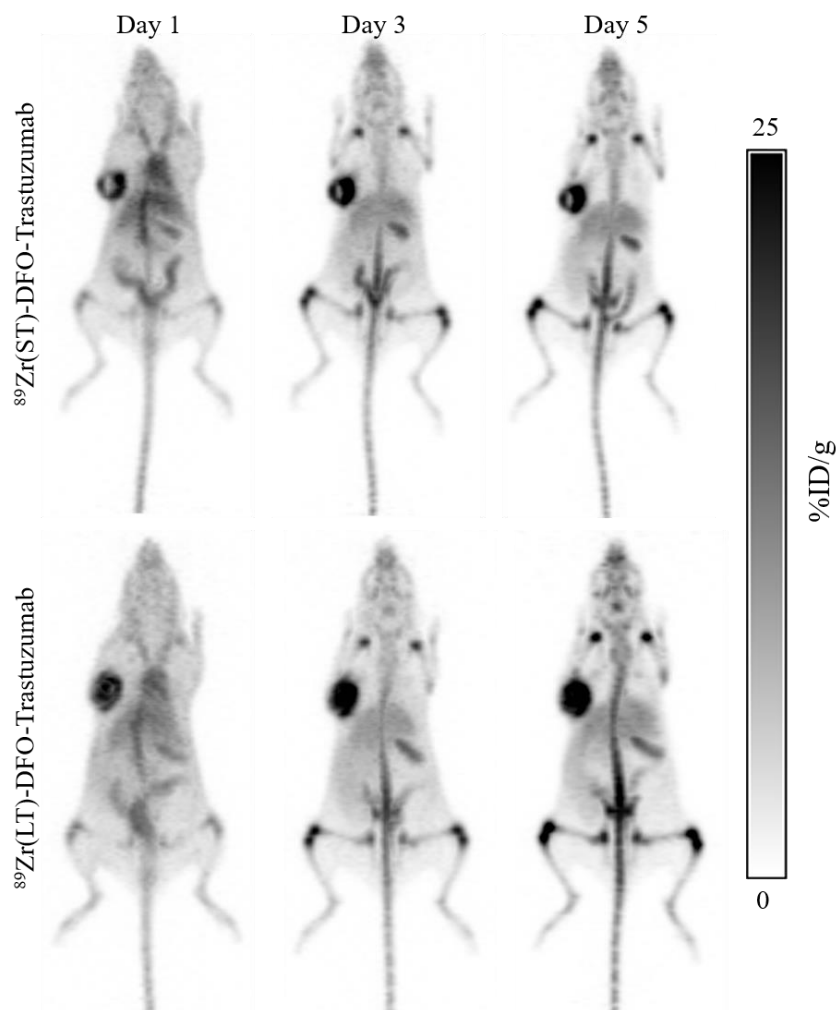
Figure 4.2 Representative PET images of DFO-Trastuzumab labeled with [89]Zr either from the solid (ST) or the liquid (LT) target. SKOV-3 tumours are visible on the right shoulder scale bar indicates %ID/g.

Table 4.5 Biodistribution data (mean %ID/g ± SD, n = 3) 5 days after injection of ^{89}Zr(ST)-DFO-Trastuzumab or ^{89}Zr(LT)-DFO-Trastuzumab in NSG mice bearing SKOV3 tumour xenografts. Significant differences are indicated with stars (p <0.05)

Tissues / Organs	^{89}Zr(ST)-DFO-Trastuzumab	^{89}Zr(LT)-DFO-Trastuzumab	
Blood	1.51 ± 0.54	2.88 ± 2.02	
Fat	0.56 ± 0.31	0.98 ± 0.10	
Uterus	20.06 ± 8.46	11.70 ± 2.07	*
Ovaries	5.83 ± 0.65	6.03 ± 2.43	
Intestine	3.26 ± 0.27	2.79 ± 0.52	
Stomach	1.90 ± 0.22	2.07 ± 0.29	
Spleen	66.73 ± 7.96	52.98 ± 9.50	*
Liver	8.26 ± 0.21	7.58 ± 0.96	
Pancreas	1.06 ± 0.05	1.33 ± 0.29	
Adrenals	3.10 ± 0.46	3.47 ± 0.22	
Kidney	2.87 ± 0.07	2.53 ± 0.79	
Lungs	2.77 ± 0.36	2.81 ± 0.78	
Heart	1.23 ± 0.17	1.20 ± 0.43	
SKOV-3 tumour	25.22 ± 3.63	21.66 ± 3.90	
Muscle	0.56 ± 0.01	0.54 ± 0.13	
Bone	12.11 ± 0.99	14.06 ± 0.85	
Brain	0.14 ± 0.04	0.16 ± 0.05	
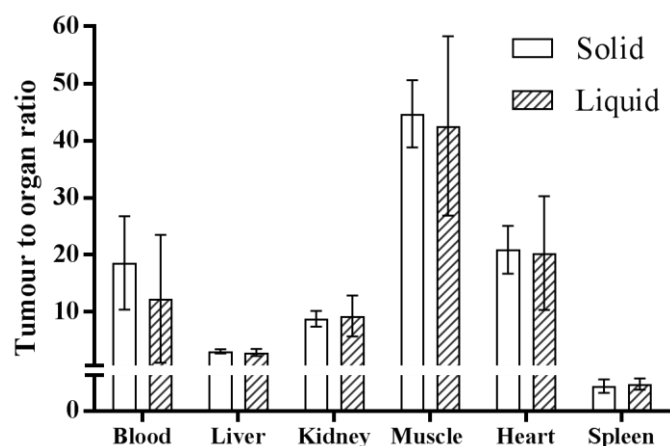
Figure 4.3 Tumour to non-target organs ratio of DFO-Trastuzumab labeled with ^{89}Zr either from the solid (ST) or the liquid (LT) target.

4.3   Conclusion

We have demonstrated production, purification and radiolabeling of antibodies using ^{89}Zr produced via a LT system. Comparing this with traditional ^{89}Zr-(ST) production, the radiolabeling of an antibody was successful with sufficient specific activities for *in vivo* pre-clinical imaging. With longer irradiation time on a LT system yield was improved provided that pressure constraints on the target were respected. ^{89}Zr-(LT) demonstrated higher purification yields and improved radiolabeling yields over ST produced ^{89}Zr. Reducing the volume of ^{89}Zr-(ST) -oxalate for radiolabeling resulted in higher and comparable radiochemical yields to that of LT. One presumable difference between the ST and LT was the higher content of metal impurities present in the ST solution that can compete for binding to DFO sites. Radiolabeling of DFO-Trastuzumab was successful with both ^{89}Zr-(ST) and ^{89}Zr-(LT), and an ideal specific activity of radiolabeled Trastuzumab was achieved. No discernible differences were observed in imaging quality or biodistribution between ST or LT ^{89}Zr-labeled immunoconjugates. Thus, LT ^{89}Zr shows promise for use in pre-clinical diagnostic imaging in cyclotron centres with only LT production set up.

Chapter 5: Separation, Purification and Radiolabeling of ^{68}Ga Produced from ^{68}Ge/^{68}Ga Generator and Cyclotron ^{68}Zn(p,n)^{68}Ga via a Liquid Target

5.1   Introduction

^{68}Ga is a positron emitting radioisotope that offers the opportunity for fast radiolabeling of novel small molecules, peptides, affibodies and antibody mimetics that are rapidly in development. The short half-life of ^{68}Ga ($T_{1/2}$ = 68 min) is well suited to biological half-life of these novel emerging biological conjugates.   Current ^{68}Ga production involves the use of either a relatively low capital cost of a germanium-68 (^{68}Ge; $T_{1/2}$ = 270.95 d) ^{68}Ge/^{68}Ga generator or via solid targetry approach, the latter infrequently used due to high cost associated with a dedicated solid target cyclotron system [106]. The low cost generator requires small hot cell real estate and is accompanied by a relatively simple purification produce making it ideal for clinical PET centres; however, there are limitations to a total yield from ^{68}Ge/^{68}Ga generator [135].   While the generator itself is a relatively inexpensive product, in centres where the demand for ^{68}Ga radiopharmaceuticals is infrequent, the eventual cost of per elution increases.   Cyclotron production of ^{68}Ga has been achieved with both solid and liquid target systems using a zinc as a starting material [75, 109, 136]. The purification methods outlined in literature are not suitable for ^{68}Ga due to its relatively short half-life.   While ^{68}Ga separation from the starting material was achieved the purification time exceeded that of the half-life of ^{68}Ga [109, 136].   In addition, high amounts of other metal impurities were not sufficiently separated from the ^{68}Ga; potentially impacting radiolabeling efficiency.   Here, we develop a method for ^{68}Ga liquid target production at BC Cancer Agency and develop a purification method to enable successful peptide radiolabeling.   In addition, we compare the radiolabeling yields, specific activity and *in vivo* biodistribution of a peptide, DOTATOC radiolabeled with ^{68}Ga produced either via liquid target cyclotron or generator system.

5.2 Materials

^{68}Ga eluted from an iThemba ^{68}Ge/^{68}Ga Generator (South Africa) was used for purification optimization studies. The liquid target material, enriched zinc oxide ^{68}ZnO (99.9%) was purchased from Isoflex (Ward Hill, MA, USA). Ultrapure nitric acid and hydrochloric acid (TraceMetal™ grade) were obtained from Fisher Scientific (Ottawa, Ontario, Canada). A Millipore system (Direct-Q® 3UV with Pump, 18 MΩcm-1) provided ultrapure water. AG50W-X8 resin was purchased from BioRad (Hercules, California, USA). DGA and LN resins were purchased from Triskem International (Bruz France). Iron test strips with range from 0-5 mg/L were purchased from Hach (London, Ontario, Canada). Quantofix Zinc test strips from Macherey-Nagal were purchased from Sigma (Oakville, Ontario, Canada). A peristaltic pump used for the semi-automated system was purchased from Welco, model number WPX1-P1/16S4-BP (Tokyo, Japan). GMP grade DOTA-TOC was purchased from Advanced Biochemical Compounds (Radeberg, Germany). Purification of radiolabeled ^{68}Ga-DOTA-TOC was performed by high performance liquid chromatography (HPLC) using a C-18 semi-preparative column (Phenomenex C18, 5 μm, 250 x 10mm) on an Agilent™ system equipped with a model 1200 quaternary pump, a model 1200 UV absorbance detector (set at 220 nm), and a Bioscan (Washington, DC) NaI scintillation detector. The radiodetector was connected to a Bioscan B-FC-1000 flow-count system, and the output from the Bioscan flow-count system was fed into an Agilent 35900E interface, which converted the analog signal to a digital signal. C18 Sep-Pak cartridges (1cc, 50 mg) were obtained from Waters Corporation (Milford, MA) and conditioned with 5 mL 100% ethanol and 10 mL 0.05 M ammonium formate. Quality control and specific activity determination of the radiolabeled ^{68}Ga-DOTA-TOC was conducted on a C-18 analytical column (Phenomenex C18, 5 μm, 250 x 4.6 mm).

5.2.1 Liquid Target Preparation

^{68}ZnO (0.5 g) was dissolved in ultrapure HNO_3 (0.5M) in a two molar excess of HNO_3 to ZnO and stirred for 1-2 hours. The solution was then evaporated to dryness on a roto-vap. 0.5M HNO_3 was added to obtain a concentration of ^{68}Zn of ~1.3 M.

5.2.2 Liquid Target Preparation

Experiments were performed on a TR19 cyclotron at BCCA (Vancouver, Canada). Irradiations were performed in a niobium-body target (ASCI, Richmond, Canada) with an internal target volume of 6.6 mL and filled with 3.8 mL of target solution. The beam window used a 30 μm thick a Havar® foil (Hamilton Precision, Lancaster, PA, USA). The target chamber was irradiated with a 10 mm wide circular collimated Gaussian beam. Irradiations were performed at 13.8 MeV with a current in the range of either ~9 μA or ~18 μA. The target solution was unloaded and transferred with pressurized helium; subsequently the solutions were collected into a vial in a hot cell.

5.2.3 $^{Nat/68}$Zn/^{68}Ga Separation

A variety of purification methods using a combination of DGA, AG50W-X8 and LN resins with varying resin amounts and order in purification design were tested. DGA resin was conditioned in 7 M HCl once packed between two 10 μm polyethylene frits in a 1 mL reservoir; LN resin was first incubated with H_2O for 20 min to swell and then in 7 M HCl once packed into a 1 or 4 mL reservoir between two frits. AG50W-X8 resin was conditioned in 10 M HCl for at least 20 min and subsequently loosely packed on top of one frit in a 15 mL reservoir. The resin columns were capped at the exit of the reservoir to prevent the resins from drying.

To test and optimize purification procedures, ^{68}Ga(^{68}Ga-*gen*) was eluted from the generator with 0.6 M HCl (5.0 mL) and was added to a mock solution of zinc nitrate (^{nat}Zn) (0.5 g) with concentrated ultrapure HNO_3. This solution was then spiked with iron chloride (0.145 mg) to reproduce possible impurity conditions post irradiation. Once a purification procedure was established it was then performed on cyclotron produced ^{68}Ga. One hour post EOB the cyclotron produced ^{68}Ga (^{68}Ga-*cyclo*) solution was removed from the hot cell and aliquots (2 μL) were taken for gamma spec analysis.

Separation of ^{68}Ga from ^{nat}Zn was performed using purification system cyclo-1, 2 and 4. Separation of ^{68}Ga from ^{68}Zn was performed using purification system cyclo-3 and 4. Purification system cyclo-1 consisted of the following resins; DGA (100 mg) and LN (50 mg)

with purification procedures provided in Figure 5.2(a). Purification system cyclo-2 was the same as system cyclo-1 with the addition of DGA (50 mg) after the LN (Figure 5.2(b)). Purification system cyclo-3 consisted of DGA (100 mg), LN (1000g) and DGA (50 mg) (Figure 5.3). AG50W-X8 (3.5 g) cation exchange resin was introduced in purification system cyclo-4 followed with LN (1000 mg) and DGA (30 mg) (Figure 5.4). Once a purification method was established, a semi-automated system was devised to decrease dose to the radiochemist.

5.2.4   Radiolabeling of DOTATOC

Purified ^{68}GaCl$_3$ was added to an 8 mL glass vial preloaded with 25 or 50 μg of DOTATOC and 0.7 mL of HEPES buffer solution (2 M, pH 5). The vial was sealed and heated in a microwave for 90 seconds. A semi-preparative column was used to separate the ^{68}Ga-DOTATOC from unlabeled DOTATOC and free ^{68}GaCl$_3$ with 79% PBS buffer and 21% acetonitrile (MeCN) at a 4.5mL/min flow rate. For preliminary optimization of the purification process the radiochemical yield was determined by HPLC. For complete radiolabeling analysis, ^{68}Ga-DOTATOC was collected from the HPLC separation and diluted with 0.05M ammonium formate solution (50 mL) and passed through a C18 light Sep-Pak cartridge. The final product was eluted in 100% ethanol and formulated in PBS for animal studies. To determine purity and specific activity, an aliquot of the purified product was injected on an analytical C-18 column at a flow rate of 2 ml/min with 79% PBS and 21% acetonitrile.

5.2.5   μPET/CT Imaging and Biodistribution

All animal experiments were performed at the Animal Resource Centre of the BC Cancer Agency Research Centre in accordance with the institutional guidelines of the University of British Columbia Animal Care Committee (Vancouver, BC, Canada) and under the supervision of authorized investigators. Female immunodeficient NOD.Cg-Prkdc^{scid} Il2rg^{tm1Wjl}/SzJ (NSG) mice (obtained from an in-house breeding colony) were administered a 60-day slow-release estradiol pellet implant (0.72 mg) (Innovative Research of America, Sarasota, FL, USA). A week post pellet implant the mice were subcutaneously injected with 5 x 10^6 ZR75-1 cells in matrigel (BD Biosciences, San Jose, CA, USA) on the right shoulder.

Four weeks post cell inoculation mice were anaesthetised with isoflurane (2% O_2) and injected via intravenous tail vein injection with 4.63±0.16 MBq of ^{68}Ga-*gen*DOTATOC or 5.01±0.51 MBq of ^{68}Ga-*cyclo*DOTATOC for PET studies. PET images of a 10 min duration were acquired 1 h post-injection using a Siemens Inveon microPET/CT scanner (Siemens Medical Solutions, Knoxville, TN, USA) and under anesthesia (2% isoflurane-O_2). Each mouse underwent a CT scan for attenuation correction followed by a PET acquisition. Images were reconstructed using the 3-dimensional ordered-subsets expectation maximization (OSEM3D, 2 iterations) followed by a fast maximum *a priori* algorithm (FastMAP: 18 iterations) and corrected for attenuation based on the CT image.

For biodistribution studies, mice were injected with 1.61±0.26 MBq ^{68}Ga-*gen*DOTATOC or 1.54±0.37 MBq of ^{68}Ga-*cyclo*DOTATOC. After 60 min after injection of the ^{68}Ga-DOTATOC, both imaging and biodistribution mice were euthanized by inhalation of isoflurane followed by CO_2. Blood was withdrawn by intracardiac puncture, and then tumours and organs of interest were harvested, washed in PBS and weighed after blotted drying. Activity of each sample was measured by a gamma counter with decay correction. The activity uptake was expressed as a percentage of the injected dose per gram of tissue (%ID/g).

5.3   Results and Discussion

5.3.1 ^{68}Zn/^{68}Ga Production via a Cyclotron in a Liquid Target

^{68}Ga was produced with a 13.9 MeV proton beam from enriched ^{68}Zn via the ^{68}Zn(p,n)^{68}Ga reaction. Irradiation time, current and applied dose were optimized to maximize yield with minimizing rapid pressure rise. As with most liquid target irradiations the formation of oxygen and hydrogen gas formed from hydroxyl radicals caused a rapid rate of gas evolution, resulting in a rapid pressure rise. High pressures in a closed target have been reported by other groups and can be quite severe in the event that the pressure reaches the maximum tolerated psi of the target [108]. One aspect, as discussed in the previous chapter with ^{89}Zr liquid target production is that the pressure rise limits irradiation time and consequently reduces potential yield.

Our initial ^{68}Ga production runs were limited to ~ 30 min durations and a final dose of ~370 µA·min as pressure rise reached our maximum threshold of 150 psi. Our maximum threshold

was based on the certification from ACSI of a maximum tolerable pressure of 200 psi with a H_2O irradiation. To reduce the rate of pressure rise, we increased the concentration of nitric acid from 0.2 to 0.5 M in the solution as previous studies showed that increasing nitric acid concentration in the target solution successfully reduced the evolution of gases [109]. Increased levels of nitrate in the solution decrease the rate of gas evolution by combining hydroxyl radicals into H_2O. We also increased the loop between the target and pressure transducer (PT) to increase volume to alleviate the pressure rise (Figure 5.1). With these modifications, we could increase both beam time (123 ± 26 min) and beam current from 7 to 22 μA to achieve higher yields of ^{68}Ga production (Table 5.1). It was a challenge to accurately determine the volume of irradiated solution post transfer from the target to the hot cell. We attempted to measure the volume using a pipette within (± 0.5 mL), however this resulted in unnecessary exposure. With our current set up we didn't have the option of pre-weighing an empty vial in which the irradiated solution was transferred to and post-weighing a radioactive sample. To obtain volume estimate of the transferred irradiated solution we loaded 5.47 ± 0.04 mL of H_2O into the target. The solution in the target was then flushed with helium as per standard protocol after irradiation and collected into a pre-weighed vial in the hot cell. The average volume if the collected H_2O was 5.29 ± 0.10 mL.
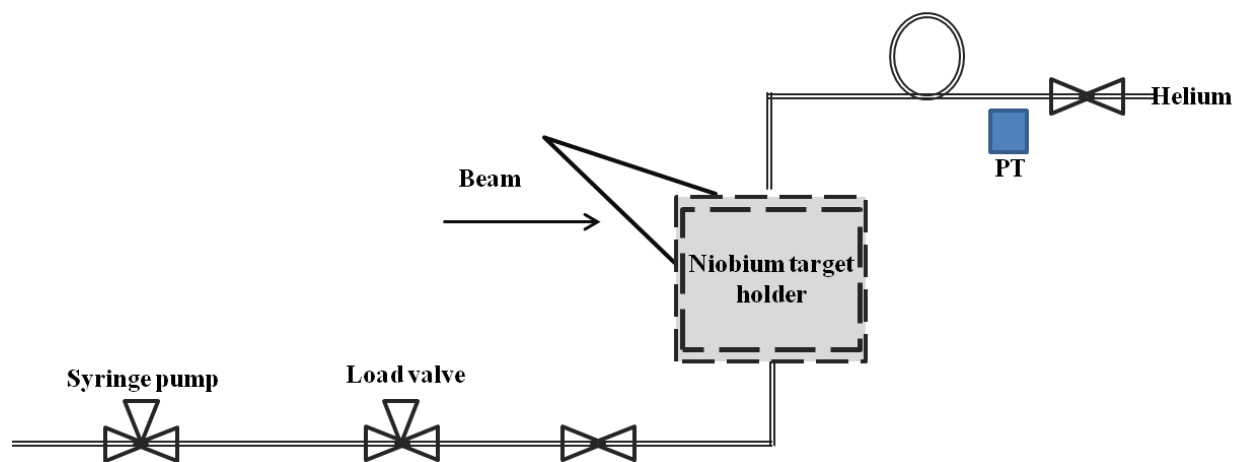
Figure 5.1 Liquid target setup.

Table 5.1 ^{68}Zn(p,n)^{68}Ga production yields from 13.8 MeV proton bombardment in liquid target on a TR19 cyclotron.

Beam time [min]	41 ± 11	62 ± 8	87 ± 14	123 ± 26
Dose [μA.min]	370 ± 62	1090 ± 42	1673 ± 192	2105 ± 166
Number of runs	5	5	21	5
Beam current [μA]	9.4 ± 2.7	17.7 ± 2.5	19.5 ± 2.2	17.6 ± 3
Beam time [min]	41 ± 11	62 ± 8	87 ± 14	123 ± 26
EOB Yield [MBq]	541 ± 321	1825 ± 417	2649 ± 555	3564 ± 608
Saturated Yield [MBq/μA]	168 ± 85	222 ± 53	192 ± 104	288 ± 25

5.3.2 $^{68/nat}$Zn/^{68}Ga Separation

Based on literature, separation of gallium from zinc is most effective when using a cation exchange resin [104]. However, the lengthy procedure is not ideal for ^{68}Ga purification. Previously reported purification methods for ^{68}Ga-cyclo liquid target production find over 2 ppm of Fe^{3+} in the final purified ^{68}Ga product [136, 137]. Based on results from Oehlke et al. a Fe^{3+} to ligand ratio of 1 would reduce the radiolabeling yield by 20% [138, 139]. Considering the radiolabeling yield was assessed by HPLC, we can presume isolated yields to be less. Based on 25 μg of DOTATOC, a maximum of 1 ppm of Fe^{3+} is permissible in 1.0 mL of purified ^{68}Ga. Considering the possibility of additional metal impurities and non-irradiated ^{68}Zn common with liquid target production we aimed to limit Fe^{3+} in the purified ^{68}Ga to less than 0.5 ppm. Based on Horwitz et al. [140] the DGA resin should have minimal potential to trap zinc at any concentration of HNO_3 or HCl and as such, DGA was used initially to separate Zn^{2+} from the ^{68}Ga^{3+}. LN resin has the potential to trap Ga^{3+} and Fe^{3+} in high HCl molar conditions then elute Ga^{3+} and retain Fe^{3+} in lower HCl molar conditions.

To optimize purification conditions, the mock solution using eluted ^{68}Ga-gen was mixed with concentrated HCl to obtain a 7 M concentration (Figure 5.2(a) purification system cyclo-1). ^{68}Ga^{3+} adsorbs on the DGA (100 mg) at high HCl molar conditions while Zn should not trap with these conditions. As Fe^{3+} and Ga^{3+} have similar retention and adsorption characteristics with DGA, the Fe^{3+} was trapped and consequently eluted with the H_2O used to de-absorb Ga^{3+} from

91

the resin. Thus, a second resin (LN, 50 mg) was used to separate the Ga^{3+} from the Fe^{3+}. The LN resin retains Ga^{3+} and Fe^{3+} at higher concentrations of HCl (5 – 7 M). At lower HCl concentrations (0.5 -1 M), Ga^{3+} will de-adsorb from the resin while Fe^{3+} remains on the column. We found breakthrough of ^{68}Ga on the LN to be less with 7 M rather than 5 M HCl. The purified ^{68}Ga was eluted with 0.6 mL of 1.0 M HCl. This purification method took 41 ± 7 min and resulted in 88 ± 3% (n = 6) ^{68}Ga decay corrected to start of purification. Radiolabeling was performed with 50 µg of DOTATOC. An average radiolabeling conversion yield, obtained from HPLC analysis was 43 ± 22% (n = 4), (Table 5.2). Radiolabeling with 1.0 M HCl was poor and inconsistent. Unlike the DGA resin, drying of the LN resin was not favourable; if the LN resin was dried prior to elution, more ^{68}Ga was retained on the column compared to when the resin was not dried during the first elution. Consequently, the elution volume of the purified ^{68}Ga was not consistent. It was a challenge for radiolabeling and for any potential automated robust radiolabeling procedures. We found with using 100 µL of the purified ^{68}Ga the radiolabeling conversion yield improved to 95% (n = 1). However, this negated the benefits of producing high yields of ^{68}Ga and would reduce the potential specific activity of the final product.
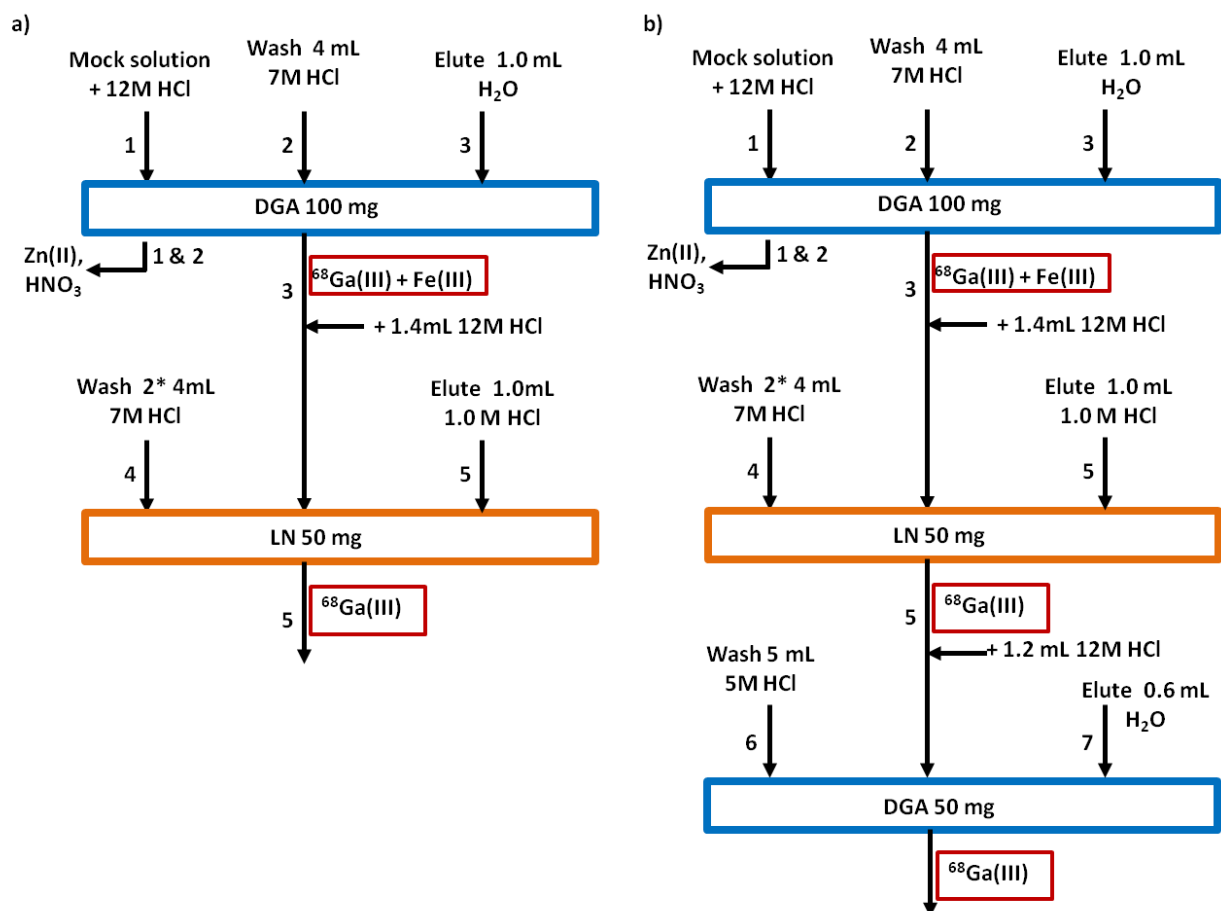
Figure 5.2 Purification system cyclo-1 using a combination of DGA and LN resins (a). A second DGA resin was used (b) to elute ^{68}Ga in H_2O for system cyclo-2

To eliminate the challenges with buffering 1.0 M HCl ^{68}Ga, a second DGA resin (50 mg) was introduced at the end of the purification step to convert the ^{68}Ga from the 1.0 M HCl condition to H_2O (Figure 5.2(b) purification system cyclo-2). Once the ^{68}Ga was loaded on to the second DGA resin, the resin was washed with 5.0 M HCl (5.0 mL) and subsequently air dried. H_2O (0.6 mL) was used to elute the ^{68}Ga and since the column was dry it enabled more a consistent pH and volume of the purified ^{68}Ga. A purification yield of $85 \pm 4\%$ and purification time of 45 ± 7 min (n = 2) was achieved and was still reduced compared to published LT purification methods [136, 137]. Radiolabeling yield with ^{68}Ga purified with this approach improved to 77 ± 30 %, however, still with some variations in yield. To assess whether these radiolabeling yields were sufficient, the ^{68}Ga-DOTATOC was separated and collected via HPLC. Isolated yields of $10 \pm$

2% (n = 2) were calculated based on the purified, isolated ^{68}Ga-DOTATOC to the starting ^{68}Ga activity in the reaction, non-decayed corrected.

The poor isolated yields suggested high impurities were still present in the purified ^{68}Ga solution. Potassium thiocyanate reacts with Fe^{3+} ions and forms a red colour; and even at low ppm there is a visible colour change. Incubation of potassium thiocyanate in the purified ^{68}Ga solution caused a visible colour change. To improve ^{68}Ga and Fe^{3+} separation, a solution of $FeCl_3$ was loaded on 50, 500 or 1000 mg of LN resin. Better retention of Fe^{3+} was found using 1000 mg compared to 500 mg of LN resin (data not shown). Thus, the three-resin approach increasing the amount of LN resin was designed (DGA 100 mg, LN 1000 mg and DGA 30 mg) (Figure 5.3, cyclo-3).

^{68}Ga-*cyclo* was produced and purified using the cyclo-3 purification set up. Purification time, determined from start of purification to final purified ^{68}Ga was within the range of the previous trials at 48 ± 11 min. However, the purification yield was reduced to 69 ± 5 % (n = 2). Radiolabeling conversion yields of DOTATOC were poor 6 ± 2% (n = 2); and, as in previous test runs, reducing the volume of ^{68}Ga used for radiolabeling (50 µL), the RCY improved to 19 % (n = 1). Determination of Fe^{3+} content in the purified ^{68}Ga samples using iron test strips were on the order of < 2 ppm. While this was higher than our ideal acceptable limits, the poor radiolabeling yield suggested another contributing impurity. This impurity was most likely zinc and thus a modification in the purification protocol was required.
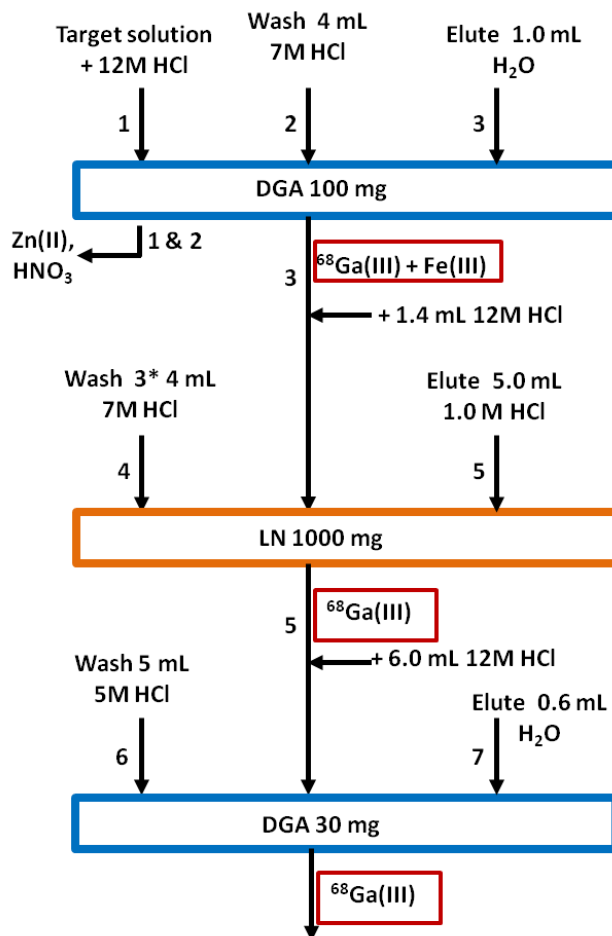
Figure 5.3 Purification schematic (cyclo-3) with DGA and LN resins; with an increase in LN resin to improve ^{68}Ga separation from Fe^{3+} for ^{68}Ga-*cyclo*.

A three-resin system using cation exchange resin AG50W-X8 (3.5 g), LN (1 g) and DGA (30 mg) was devised (Figure 5.4, cyclo-4). Further literature investigation into the DGA resin with zinc and gallium showed similar retention and de-absorption of these two elements with HCl, suggesting that DGA is not suited for zinc and gallium separation [141]. Using the mock solution, the average purification time was 97 ± 30 min with a purification yield of $74 \pm 6\%$ (n = 3). To improve specific activity for small animal *in vivo* studies radiolabeling was performed with 25 μg of DOTATOC. This resulted in a RCY of $97 \pm 2\%$ based on HPLC with an isolated yield of $54 \pm 5\%$ (n = 2). Translating this method for ^{68}Ga-*cyclo* purification, a purification yield of $64 \pm 10\%$ was achieved within 103 ± 15 min (n = 3). Radiolabeling yield was consistent as with mock runs of 97% (n = 1).
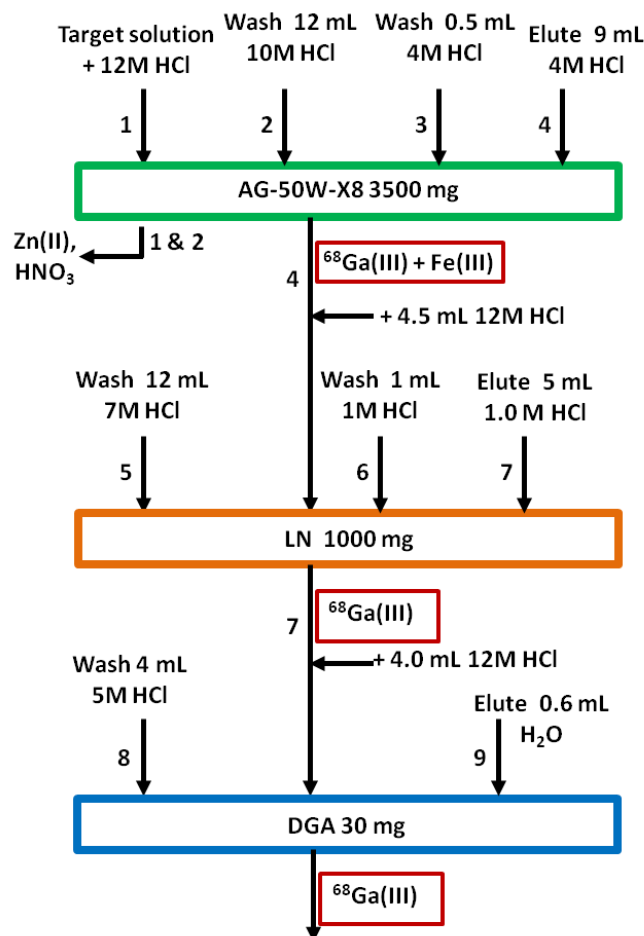
Figure 5.4 Purification schematic (cyclo-4) utilizing AG50W-X8, LN and DGA resins for improved ^{68}Ga-*cyclo* separation from Zn^{2+} and Fe^{3+}.

To decrease the purification time and reduce radiation exposure a semi-automatic system was devised. Using 1 pump for all three resins reduced the purification time of the mock ^{68}Ga solution to 69 ± 16 min; however, decayed corrected purification yield also decreased to 39 ± 16% (n = 2). RCY and isolated yields of ^{68}GaDOTATOC were poor at 61% and 4% respectively (n = 1). Testing the purified ^{68}Ga with iron and zinc strips showed > 100 ppm of Zn^{2+} and > 5 ppm Fe^{3+} in the purified ^{68}Ga. Separation of ^{68}Ga from Zn^{2+} and Fe^{3+} contaminants using one peristaltic pump for all three resins was not effective evident with the poor radiolabeling yield of ^{68}GaDOTATOC. With this system, all three resins were serviced by the same pump which

forced the solution from one resin to the next to be pumped through the same line. A purification system with three peristaltic pumps, one dedicated to each resin was designed and prevented the spread of metal impurities during the purification.

^{68}Ga-cyclo separation using the three pumps required a longer purification time (99 ± 16 min) compared to the 1 pump system due to the need to switch the power supply to each pump when switching from one resin to the next. This physical constraint would be a contributing factor to purification time with a fully automated system. ^{68}Ga was purified with 50 ± 10% decayed corrected yield (n = 5). However, despite the lower purification yield, radiolabeling conversion yield of 25 μg of DOTATOC was consistent at 91 ± 6% with an isolated yield of 25 ± 10% (n = 4).

Table 5.2 ^{68}Ga separation, and purification yields either with a mock solution or from cyclotron production with various separation schemes. The associated radiolabeling yields of ^{68}Ga-DOTATOC are presented as radiochemical conversion yield assessed by HPLC. (N/A = not acquired).

	Gallium source	# of runs	Resin type and amount			Final ^{68}Ga elution	Yield non DC [%]	Yield DC [%]	Time [min]	RCY determined by HPLC [%]	Isolated Yield non DC [%]
			^{68}Ga purification and separation							**^{68}Ga-DOTATOC radiolabeling**	
			1	2	3						
Manual purification	Mock	6	DGA 100 mg	LN 50 mg	---	1.0 M HCl	58 ± 5	88 ± 3	41 ± 7	43 ± 22 [c]	N/A
	Mock	2	DGA 100 mg	LN 50 mg	DGA 50 mg	H_2O	50 ± 4	85 ± 4	45 ± 7	77 ± 30 [b]	10 ± 2
	Cyclotron	2	DGA 100 mg	LN 1000 mg	DGA 50 mg	H_2O	42 ± 1	69 ± 5	48 ± 11	6 ± 2 [b]	2 ± 1
	Mock	3	AG50W-X8 3500 mg	LN 1000 mg	DGA 30 mg	H_2O	28 ± 8	74 ± 8	97 ± 30	97 ± 2 [b]	54 ± 5
	Cyclotron	3	AG50W-X8 3500 mg	LN 1000 mg	DGA 30 mg	H_2O	23 ± 5	64 ± 10	103 ± 15	97 [a]	44
1 pump	Mock	2	AG50W-X8 3500 mg	LN 1000 mg	DGA 30 mg	H_2O	18 ± 7	39 ± 16	69 ± 16	61 [a]	4
3 pumps	Cyclotron	5	AG50W-X8 3500 mg	LN 1000 mg	DGA 30 mg	H_2O	19 ± 5	50 ± 10	99 ± 16	91 ± 6 [c]	25 ± 10

[a] n = 1, [b] n = 2, [c] n = 4

5.3.3   Gamma Spectrum Analysis

Dose calibrator measurements performed within 1 h of EOB do not consider activity from ^{13}N or ^{11}C co-produced with ^{68}Ga during irradiation. Even with gamma spectral analysis is it difficult to distinguish between ^{13}N and ^{11}C yields as both have gamma emissions at 511 keV. Gamma spectral analysis of 2 µL of irradiated solution samples analysed 9 h post EOB showed predominant gamma emission at 511 and 1077 keV corresponding to ^{68}Ga (Figure 5.5). There were some impurities of ^{67}Ga evident with lower energy emissions at 93, 184, 300 and 393 keV. However, the contribution of ^{67}Ga corresponds to 0.014 % of the total ^{68}Ga produced. ^{66}Ga was also present with a lower isotopic impurity of 0.009% of the total ^{68}Ga produced.
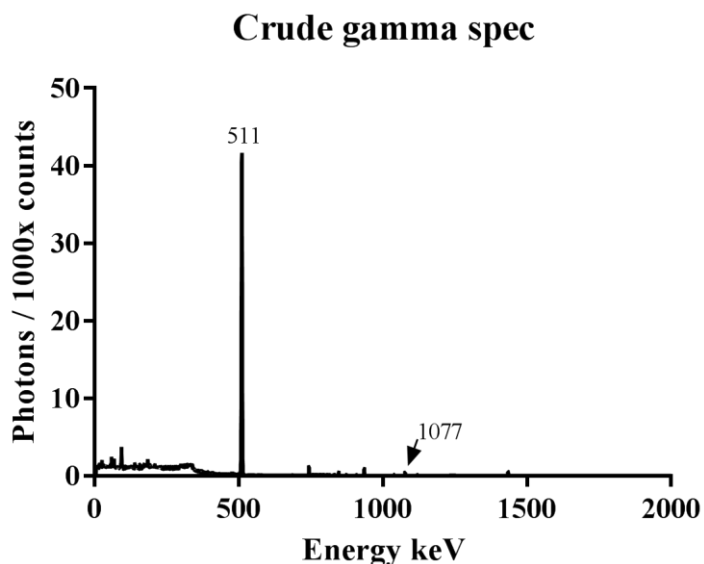
Figure 5.5 Gamma spec analysis of the irradiated non-purified solution.   Analysis was performed 9 h EOB.

5.3.4 Results Specific for the PET imaging study of ^{68}GaDOTATOC

5.3.4.1 Production Results

Elution of the generator with 0.6 M HCl produced 0.36 GBq of ^{68}Ga-*gen* at time of elution measured with a dose calibrator. Irradiation of 0.5 g of ^{68}Zn(NO$_3$)$_2$ with an average beam current of 18 µA for 109 min produced 2.76 GBq of ^{68}Ga-*cyclo* as measured with a dose calibrator, 39 min post EOB.

5.3.4.2 Purification Results

^{68}Ga-*cyclo* separation and purification was achieved in 90 min and resulted in 380 MBq available for radiolabeling with a 42 % decayed corrected yield based on dose calibrator measurement. ^{68}Ga-*gen* separation and purification resulted in a yield of 297 MBq available for radiolabeling.

5.3.4.3 Radiolabeling

Purified ^{68}Ga-*gen* (297 MBq) and ^{68}Ga-*cyclo* (380 MBq) was successfully radiolabeled to DOTATOC (25 µg) with radiolabeling conversion yields of 96 % and 94 % respectively; as determined by HPLC. ^{68}Ga-DOTATOC was purified and collected by HPLC and trapped on a C-18 sep pak. Elution of the sep pak produced; 93 MBq of ^{68}Ga-*gen*-DOTATOC and 88 MBq of ^{68}Ga-*cyclo*-DOTATOC. Quality control of the purified products yielded a radiochemical purity of > 98 % for both. Specific activity was calculated as 115 MBq/nmol for ^{68}Ga-*gen*-DOTATOC and 443 MBq/nmol for ^{68}Ga-*cyclo*-DOTATOC

5.3.4.4 *In vivo* Results

µPET-CT images performed at 1 h post-injection (Figure 5.6) showed similar high uptake of the ^{68}Ga-DOTATOC within the ZR75-1 tumours. For both ^{68}Ga-*gen* and ^{68}Ga-*cyclo*, a typical biodistribution profile of ^{68}Ga-DOTATOC was observed with high kidney and bladder uptake. Sharp contrast PET images were obtained, enabling clear visualization of the tumour xenografts. Biodistribution data corroborated the PET imaging results. High tumour uptake expressed as percent of injected dose per gram of tissue (%ID/g) were the same for both groups; ^{68}Ga-*gen*: 18.34 ± 3.41 %ID/g and ^{68}Ga-*cyclo*: 18.17 ± 5.69 %ID/g (Table 5.3). High uptake of either

^{68}Ga-DOTATOC was evident in the pancreas and lungs, an expected result due to the high expression of somatostatin receptors in these organs [86]; all other organs showed no statistical differences in absolute uptake.
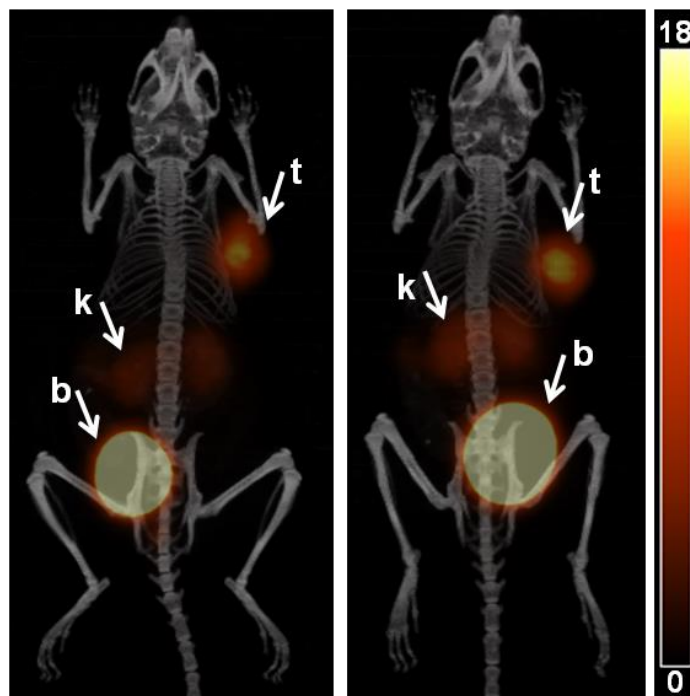
Figure 5.6 Representative maximum projection PET images fused with CT of DOTA-TOC radiolabeled with ^{68}Ga either from the generator (left) or the cyclotron (right). ZR75-1 tumours (t) are visible on the right shoulder as well as kidney (k) uptake and bladder (b), scale bar indicates %ID/g.

Table 5.3 Biodistribution data (mean ± SD %ID/g, n = 6) 1 hour after injection of ⁶⁸Ga-*gen*-DOTATOC or ⁶⁸Ga-*cyclo*-DOTATOCin NSG mice bearing ZR75-1 tumours.

Tissues / Organs	⁶⁸Ga-*gen*-DOTATOC	⁶⁸Ga-*cyclo*-DOTATOC
Blood	0.53 ± 0.17	0.80 ± 0.19
Fat	0.19 ± 0.07	0.36 ± 0.18
Ovaries	0.83 ± 0.29	0.87 ± 0.21
Uterus	0.61 ± 0.16	0.86 ± 0.11
Intestine	2.14 ± 0.79	2.16 ± 0.82
Spleen	0.47 ± 0.21	0.66 ± 0.19
Pancreas	10.95 ± 2.50	12.40 ± 2.8
Stomach	2.45 ± 1.12	2.81 ± 1.55
Liver	0.55 ± 0.14	0.72 ± 0.10
Adrenals	4.85 ± 1.77	6.41 ± 3.55
Kidney	11.37 ± 1.51	13.81 ± 2.65
Heart	0.31 ± 0.10	0.39 ± 0.05
Lungs	11.43 ± 6.48	7.73 ± 4.41
Tumour	18.34 ± 3.41	18.17 ± 5.69
Muscle	0.15 ± 0.06	0.21 ± 0.05
Bone	0.38 ± 0.22	0.49 ± 0.13
Brain	0.04 ± 0.01	0.06 ± 0.01

5.4   Conclusion

We developed a method for ⁶⁸Ga purification that is sufficient for radiolabeling of bioconjugates, a process that until now resulted in poor radiolabeling yields. The three resin system separated ⁶⁸Ga from the starting zinc material with the AG50W-X8 resin and the use of LN resin significantly reduced iron content. The addition of a DGA resin enabled purification of ⁶⁸Ga in consistent volume and pH allowing for robust radiolabeling. These resin combinations resulted

in successful radiolabeling of DOTA-TOC, with high radiochemical yield. We have demonstrated production, purification and radiolabeling of DOTATOC using ^{68}Ga produced via a LT system suitable for *in vivo* studies. Comparing this with traditional ^{68}Ga production from a generator, the radiolabeling of DOTATOC was successful with sufficient specific activities for *in vivo* pre-clinical imaging. Increased irradiation time on a LT system can increase yield providing the pressure constraints on the target are respected. No discernible differences were observed in imaging quality or biodistribution between generator or LT ^{68}Ga-labeled peptide. Thus, LT ^{68}Ga shows promise for use in pre-clinical diagnostic imaging in cyclotron centres without the need for a ^{68}Ge/^{68}Ga generator.

Chapter 6: Conclusion

6.1 Summary of Study and Findings

In chapter 2, we compared two bifunctional chelators suitable for ^{111}In radiolabeling and compared them by assessing antibody biodistribution with SPECT imaging. The biodistribution of the p-SCN-Bn-DTPA and p-SCN-Bn-CHX-A"-DTPA chelators conjugated to Trastuzumab and radiolabeled with ^{111}In showed similar uptake at day 1, 3 and 5 post injection. In addition, we attempted to accelerate the pharmacokinetics of radiolabeled antibodies to increase clearance and obtain higher tumour to background contrast at earlier time points. However, the approach of administrating large doses of Rabbit IgG or Rabbit IgG-Fc was not successful. In chapter 2 we screened antibody candidates to assess E-cadherin expression *in vivo* using ^{111}In labeled mAbs. Rat DECMA-1 and Rabbit EP700Y E-cadherin antibody candidates demonstrated good binding of E-cadherin for flow cytometry analysis in breast cancer cells and breast cancer cells derived from tumours. Rabbit 24E10 and Rabbit EP700Y showed good binding, evident with the high staining obtained from IHC analysis of breast cancer tumours. However, imaging results obtained from using these antibodies radiolabeled with ^{111}In, did not show superior uptake in E-cadherin expressing tumours compared to an IgG isotype control. In chapter 3, we demonstrated the production of ^{89}Zr with a solid target and compared the effects of altering starting material (mass, diameter, purity) and beam parameters (energy, duration and current) on yield and purity. Optimization of production permitted high radiolabeling yields of antibodies. Furthermore, we investigated the effects on biodistribution by administrating different antibody amounts (4, 18 or 30 μg). We observed that lower doses of antibody resulted in higher spleen and liver uptake. In chapter 4, we demonstrated the ability to produce sufficient yields of ^{89}Zr with a liquid target. Here the production yields of ^{89}Zr were sufficient for radiolabeling antibodies for PET imaging. A comparison between solid and liquid target ^{89}Zr was performed and no differences in antibody biodistribution was observed. In chapter 5, we demonstrated the ability to produce ^{68}Ga with a liquid target. Here, we developed and optimized purification methods to permit high radiolabeling of DOTATOC. We then compared the feasibility of liquid

target ^{68}Ga for radiolabeling and performed comprehensive *in vivo* studies compared with generator ^{68}Ga. Liquid target ^{68}Ga performed as successfully as generator ^{68}Ga in terms of radiolabeling and *in vivo* biodistribution of DOTATOC using PET.

6.2 Strength and Limitations

This thesis started with using a well validated approach to ^{111}In mAb imaging to optimize mAb imaging in preclinical models using established mAbs and also novel E-cadherin mAbs. In parallel, ^{89}Zr production was implemented using conventional solid target production to enable immunoPET imaging. Here, we tested a variety of targets to optimize and improve purification and radiolabeling yields. Following the methods we established for ^{89}Zr production and immunoPET imaging, we then translated the approach to liquid target ^{89}Zr production. Here we demonstrated the feasibility of radiometal production of ^{89}Zr and antibody radiolabeling with sufficient specific activity for *in vivo* preclinical studies without the need for a solid target set up. Eliminating the need for an expensive and bulky solid target setup expands liquid target ^{89}Zr to existing cyclotron centers. This liquid target production approach was then adapted to ^{68}Ga, eliminating the need of a generator; a benefit to centres where the requirement for ^{68}Ga is infrequent.

The multidisciplinary aspects of this thesis: from cyclotron radiometal production to *in vivo* analysis provided the opportunity to explore all aspects of nuclear molecular targeted imaging. We can understand and appreciate the requirements and feasibility of each step as individual components and how they combine for the end goal of *in vivo* imaging. The dynamic interplay between the feasibility of production encouraged a strong understanding of all the components. ^{89}Zr and ^{68}Ga are emerging radioisotopes in the preclinical and clinical nuclear medicine field. We took the approach of liquid target production and tested the ability to purify and radiolabel these radioisotopes to make them more accessible to the nuclear medicine community.

This project is not without limitations; with increased irradiation time, the yield for liquid target ^{89}Zr was still not superior to that of solid target ^{89}Zr. With the solid target ^{89}Zr in chapter 3 we were able to produce, purify and radiolabel enough ^{89}Zr for 20 pre-clinical subjects. This would not be possible with liquid target ^{89}Zr without an improvement in end of bombardment yield.

The separation and purification of liquid target ^{68}Ga from the staring material and metal impurities is not well suited to the 68 min half life of ^{68}Ga. E-cadherin itself being a cell-cell adherent protein served to be a challenging target, while the cells demonstrated high expression as determined by flow cytometry and immunohistochemistry our *in vivo* results were not as positive. The characteristics of being a cell-cell adhesion protein may limit the accessibility of protein. This limited accessibility may require smaller vectors such as small molecules as opposed to a large vector such as an antibody.

6.3 Overall Significance and Implications

The approach to radiometal production with a liquid target expands the use of radiometals to cyclotron centers that are only equipped with liquid target production capabilities. It also provides the opportunity to readily produce a variety of radiometals when required. The impact on diagnostic imaging will be greatly improved with the availability of novel bioconjugates radiolabeled with radiometals.

With over 18 cyclotron centers in Canada alone the production and radiolabeling of radiometals produced with a liquid target will benefit these centers that do not have the infrastructure for solid target radiometal production. On a global scale, out of more than 800 cyclotrons, over 75% of these cyclotrons serve clinical and or research facilities with radioisotopes. Liquid target radiometal production will increase the variety of radiometals available to both clinical and research facilities. This in turn will improve the ability to radiolabel novel targeting vectors to increase the radiopharmaceuticals options and expand on the conventional FDG approach to oncology diagnostics. Patients will be able to receive a diagnostic scan with a radiopharmaceutical that is tailored to their disease type improving personalized medicine.

6.4 Future Directions

The approach to radiometal production with a liquid target expands the use of radiometals to cyclotron centers that are only equipped with liquid target production capabilities. It also provides the opportunity to readily produce a variety of radiometals when required. The impact

on diagnostic imaging will be greatly improved with the availability of novel bioconjugates radiolabeled with radiometals.

One avenue for improvement is the purification time of ^{68}Ga; currently, the end of bombardment yield was much higher than the maximum output of a ^{68}Ge/^{68}Ga generator. The long purification time separating Ga from the starting material and metal impurities may have not been a concern with a Ga isotope with a long half life. However, considering the short half-life of ^{68}Ga, the isolated recovered yield was low and negated the benefits of the high end of bombardment yields. Automating the purification system and starting purification at end of bombardment would reduce purification time and improve isolated yield. It would also be essential for routine ^{68}Ga production. Unlike liquid target ^{68}Ga, the purification process of liquid target ^{89}Zr was fast and similar to that of solid target ^{89}Zr. However, under the current production methods we were limited to approximately 100 MBq of ^{89}Zr at end of bombardment. Post purification and antibody radiolabeling yields were sufficient for imaging approximately 6-8 pre-clinical subjects. While not sufficient for a comprehensive pre-clinical *in vivo* study with multiple biodistribution time points, this may be suitable for one or two patient doses. In a clinical centre where the demand for ^{89}Zr is infrequent the liquid target approach may be well suited.

While we demonstrated the ability to radiolabel liquid target produced ^{89}Zr and ^{68}Ga for antibodies and peptides respectively, there are many other radiometals that have been produced with a liquid target [88, 109, 142]. Scandium-44 (^{44}Sc) is a positron emitter conventionally produced either from a titatnium-44 ^{44}Ti/^{44}Sc generator with maximum yields of 185 MBq or via solid target cyclotron production with enriched calcium-44 (^{44}Ca). ^{44}Ti has a half life of 60 years, requiring years of long-term storage of the generator before safe disposal. The half life of ^{44}Sc ($T_{1/2} = 3.97$ h) is well suited to vectors with slightly longer biological half lives that vectors radiolabeled with ^{68}Ga. Antibody fragments F(ab')2 and Fab are examples of vectors that are well suited to the half life of ^{44}Sc [72]. Similarly, with ^{68}Ga and ^{89}Zr, the liquid target production of ^{44}Sc has been achieved, however this process with complete radiolabeling and *in vivo* studies have not been validated. Another positron emitting radiometal with a similar half life is ^{61}Cu ($T_{1/2} = 3.33$ h). This radiometal can be produced with enriched zinc-64 (^{64}Zn) in a ^{64}Zn(p,α)^{61}Cu reaction at low energies suited for a clinical cyclotron.

Understanding the interplay between radiometal production and the requirements needed for nuclear medicine imaging will forward the development of novel radiotracers and make them more accessible to the nuclear medicine community.

Bibliography

[1] Price EW and Orvig C. Matching chelators to radiometals for radiopharmaceuticals. Chem Soc Rev 2014;43:260-90.

[2] Honarvar H, Strand J, Perols A, Orlova A, Selvaraju RK, Karlstrom AE, et al. Position for Site-Specific Attachment of a DOTA Chelator to Synthetic Affibody Molecules Has a Different Influence on the Targeting Properties of Ga-68-Compared to In-111-Labeled Conjugates. Mol Imaging 2014;13.

[3] Malmberg J, Perols A, Varasteh Z, Altai M, Braun A, Sandstrom M, et al. Comparative evaluation of synthetic anti-HER2 Affibody molecules site-specifically labelled with In-111 using N-terminal DOTA, NOTA and NODAGA chelators in mice bearing prostate cancer xenografts. Eur J Nucl Med Mol I 2012;39:481-92.

[4] Jodal L, Le Loirec C, and Champion C. Positron range in PET imaging: an alternative approach for assessing and correcting the blurring. Physics in medicine and biology 2012;57:3931-43.

[5] Wood KA, Hoskin PJ, and Saunders MI. Positron emission tomography in oncology: A review. Clin Oncol-Uk 2007;19:237-55.

[6] Ishibashi K, Onishi A, Fujiwara Y, Ishiwata K, and Ishii K. Plasma Glucose Levels Affect Cerebral 18F-FDG Distribution in Cognitively Normal Subjects With Diabetes. Clinical nuclear medicine 2016;41:e274-80.

[7] Nabi HA and Zubeldia JM. Clinical applications of (18)F-FDG in oncology. Journal of nuclear medicine technology 2002;30:3-9; quiz 10-1.

[8] Wadas TJ, Wong EH, Weisman GR, and Anderson CJ. Coordinating Radiometals of Copper, Gallium, Indium, Yttrium, and Zirconium for PET and SPECT Imaging of Disease. Chem Rev 2010;110:2858-902.

[9] Gotzmann C, Trapp N, Weber W, and Bartholoma MD. Highly stable chelators for radiocopper based on TACN with pendant azaheterocyclic arms. J Labelled Compd Rad 2013;56:S67-S.

[10] Zhang L, Ward ML, Phillips ARJ, Zhang SP, Kennedy J, Barry B, et al. Protection of the heart by treatment with a divalent-copper-selective chelator reveals a novel mechanism underlying cardiomyopathy in diabetic rats. Cardiovasc Diabetol 2013;12.

[11] Lu J, Pontre B, Pickup S, Choong SY, Li MM, Xu H, et al. Treatment with a copper-selective chelator causes substantive improvement in cardiac function of diabetic rats with left-ventricular impairment. Cardiovasc Diabetol 2013;12.

[12] Cho HY, Blum RA, Sunderland T, Cooper GJS, and Jusko WJ. Pharmacokinetic and Pharmacodynamic Modeling of a Copper-Selective Chelator (TETA) in Healthy Adults. J Clin Pharmacol 2009;49:916-28.

[13] Zhang L, Phillips ARJ, Ward ML, and Cooper GJS. Reversal of Diabetes-Evoked Changes in Cardiac Function by Treatment with a Copper (Ii)-Selective Chelator. J Physiol Sci 2009;59:315-.

[14] Cooper GJS, Young AA, Gamble GD, Occleshaw CJ, Dissanayake AM, Cowan BR, et al. A copper(II)-selective chelator ameliorates left-ventricular hypertrophy in type 2 diabetic patients: a randomised placebo-controlled study. Diabetologia 2009;52:715-22.

[15] Gong D, Lu J, Chen X, Reddy S, Crossman DJ, Glyn-Jones S, et al. A copper(II)-selective chelator ameliorates diabetes-evoked renal fibrosis and albuminuria, and suppresses pathogenic

TGF-beta activation in the kidneys of rats used as a model of diabetes. Diabetologia 2008;51:1741-51.

[16] Jullig M, Chen XY, Hickey AJ, Crossman DJ, Xu AM, Wang Y, et al. Reversal of diabetes-evoked changes in mitochondrial protein expression of cardiac left ventricle by treatment with a copper(II)-selective chelator. Proteom Clin Appl 2007;1:387-99.

[17] Jodal L, Le Loirec C, and Champion C. Positron range in PET imaging: non-conventional isotopes. Physics in medicine and biology 2014;59:7419-34.

[18] Nawaz S, Berry DJ, Ballinger JR, and Blower PJ. Comparison of Chelators Which Bind Gallium-68 at Room Temperature. Eur J Nucl Med Mol I 2011;38:S193-S.

[19] McCarthy DW, Shefer RE, Klinkowstein RE, Bass LA, Margeneau WH, Anderson CJ, et al. The efficient production of high specific activity copper-64 using a biomedical cyclotron. J Nucl Med 1996;37:233-.

[20] Paul RL, Dearling J, Halsted P, Ballinger J, Lewis JS, Martin KE, et al. Son of CuATSM: Towards Optimised Second-generation Copper Complexes for HypoxiaImaging. Eur J Nucl Med Mol I 2005;32:S269-S.

[21] Lewis JS, Dearling JLJ, Sosabowski JK, Zweit J, Carnochan P, Kelland LR, et al. Copper bis(diphosphine) complexes: radiopharmaceuticals for the detection of multi-drug resistance in tumours by PET. Eur J Nucl Med 2000;27:638-46.

[22] Dearling JLJ, Lewis JS, Mullen GED, Rae MT, Zweit J, and Blower PJ. Design of hypoxia-targeting radiopharmaceuticals: selective uptake of copper-64 complexes in hypoxic cells in vitro. Eur J Nucl Med 1998;25:788-92.

[23] Palacios J, Garcia-Macias MC, Bryant B, Sobel ME, and Merino MJ. E-cadherin (ECD) gene inactivation in pleomorphic lobular carcinoma (PLC) of the breast. Modern Pathol 2002;15:45a-a.

[24] Lewis JS, Heath SL, Powell AK, Zweit J, and Blower PJ. Diphosphine bifunctional chelators for low-valent metal ions. Crystal structures of the copper(I) complexes [CuClL(2)(1)] and [CuL(2)(1)][PF6] [L(1) equals 2,3-bis(diphenylphosphino)maleic anhydride]. J Chem Soc Dalton 1997:855-61.

[25] Moll R, Mitze M, Frixen UH, and Birchmeier W. Differential Loss of E-Cadherin Expression in Infiltrating Ductal and Lobular Breast Carcinomas. Am J Pathol 1993;143:1731-42.

[26] Palacios J, Sarrio D, Garcia-Macias MC, Bryant B, Sobel ME, and Merino MJ. Frequent E-cadherin gene inactivation by loss of heterozygosity in pleomorphic lobular carcinoma of the breast. Modern Pathol 2003;16:674-8.

[27] Palacios J, Garcia-Macias MC, Bryant B, Sobel ME, and Merino MJ. E-cadherin (ECD) gene inactivation in pleomorphic lobular carcinoma (PLC) of the breast. Lab Invest 2002;82:45a-a.

[28] Palacios J, Bryant B, Hardisson D, Sobel ME, and Merino MJ. cDNA microarray gene expression analysis of microdissected frozen ductal breast carcinomas after linear RNA amplification. Lab Invest 2002;82:45a-a.

[29] Palacios J, Bryant B, Hardisson D, Sobel ME, and Merino MJ. cDNA microarray gene expression analysis of microdissected frozen ductal breast carcinomas after linear RNA amplification. Modern Pathol 2002;15:45a-a.

[30] Zhao DF, Liao XW, and Yin DD. Evaluation of CO_2 enhanced oil recovery and sequestration potential in low permeability reservoirs, Yanchang Oilfield, China. J Energy Inst 2014;87:306-13.

[31] Qureshi HS, Linden MD, Divine G, and Raju UB. E-cadherin status in breast cancer correlates with histologic type but does not correlate with established prognostic parameters. Am J Clin Pathol 2006;125:377-85.

[32] Divine G, Linden MD, Raju U, and Qureshi HS. E-cadherin in pleomorphic lobular carcinoma in situ and indeterminant carcinoma in-situ of breast. Modern Pathol 2003;16:44a-a.

[33] Nakamoto Y, Tatsumi M, Hammoud D, Cohade C, Osman MM, and Wahl RL. Normal FDG distribution patterns in the head and neck: PET/CT evaluation. Radiology 2005;234:879-85.

[34] Qureshi HS, Divine G, Linden MD, and Raju U. E-cadherin in pleomorphic lobular carcinoma in situ and indeterminant carcinoma in-situ of breast. Lab Invest 2003;83:44a-a.

[35] Qureshi HS, Raju UB, Divine GW, and Linden MD. Pleomorphic lobular carcinoma in situ of the breast: Diagnostic value of E-cadherin. Am J Clin Pathol 2002;118:650-.

[36] Bassis CM and Visick KL. The cyclic-di-GMP phosphodiesterase BinA negatively regulates cellulose-containing biofilms in Vibrio fischeri. Journal of bacteriology 2010;192:1269-78.

[37] Jahangiri P, Zacchia NA, Buckley K, Benard F, Schaffer P, Martinez DM, et al. An analytical approach of thermodynamic behavior in a gas target system on a medical cyclotron. Applied radiation and isotopes : including data, instrumentation and methods for use in agriculture, industry and medicine 2016;107:252-8.

[38] Kafka A, Tomas D, Beros V, Pecina HI, Zeljko M, and Pecina-Slaus N. Brain Metastases from Lung Cancer Show Increased Expression of DVL1, DVL3 and Beta-Catenin and Down-Regulation of E-Cadherin. Int J Mol Sci 2014;15:10635-51.

[39] Pecina-Slaus N, Martic TN, Deak AJ, Zeljko M, Hrascan R, Tomas D, et al. Genetic and protein changes of E-cadherin in meningiomas. J Cancer Res Clin 2010;136:695-702.

[40] Desmond KW, Zacchia NA, Waite JH, and Valentine MT. Dynamics of mussel plaque detachment. Soft matter 2015;11:6832-9.

[41] Lacaille J, Ly J, Zacchia N, Bourkas S, Glaser E, and Knauper B. The effects of three mindfulness skills on chocolate cravings. Appetite 2014;76:101-12.

[42] Uematsu H, Sadato N, Yonekura Y, Tsuchida T, Nakamura S, Sugimoto K, et al. Coregistration of FDG PET and MRI of the head and neck using normal distribution of FDG. J Nucl Med 1998;39:2121-7.

[43] Glaudemans AW, de Vries EF, Galli F, Dierckx RA, Slart RH, and Signore A. The use of (18)F-FDG-PET/CT for diagnosis and treatment monitoring of inflammatory and infectious diseases. Clinical & developmental immunology 2013;2013:623036.

[44] Kim JW and Dang CV. Cancer's molecular sweet tooth and the Warburg effect. Cancer Res 2006;66:8927-30.

[45] Pecina-Slaus N, Eva-Martic TN, Beros V, and Tomas D. Genetic alterations of E-cadherin and beta-catenin in germinoma and teratoma: Report of two central nervous system cases. Pathol Oncol Res 2007;13:370-4.

[46] Pecina-Slaus N, V K, Zigmund M, Slaus M, Nikuseva-Martic T, and Cacic M. E-cadherin and beta-catenin expression patterns in malignant melanoma assessed by image analysis. Febs J 2005;272:130-.

[47] Pecina-Slaus N, Gall-Troselj K, Slaus M, Radic K, Nikuseva-Martic T, and Pavelic K. Genetic changes of the E-cadherin and APC tumour suppressor genes in clear cell renal cell carcinoma. Pathology 2004;36:145-51.

[48] Pecina-Slaus N. Tumor suppressor gene E-cadherin and its role in normal and malignant cells. Cancer Cell Int 2003;3.

[49] Vaccaro C, Zhou JC, Ober RJ, and Ward ES. Engineering the Fc region of immunoglobulin G to modulate in vivo antibody levels. Nature biotechnology 2005;23:1283-8.

[50] Zacchia NA and Valentine MT. Design and optimization of arrays of neodymium iron boron-based magnets for magnetic tweezers applications. The Review of scientific instruments 2015;86:053704.

[51] Koleva-Kolarova RG, Greuter MJW, van Kruchten M, Vermeulen KM, Feenstra T, Buskens E, et al. The value of PET/CT with FES or FDG tracers in metastatic breast cancer: a computer simulation study in ER-positive patients. Brit J Cancer 2015;112:1617-25.

[52] Ward ES, Martinez C, Vaccaro C, Zhou J, Tang Q, and Ober RJ. From sorting endosomes to exocytosis: Association of Rab4 and Rab11 GTPases with the fc receptor, FcRn, during recycling. Mol Biol Cell 2005;16:2028-38.

[53] Ward ES, Martinez C, Vaccaro C, Zhou J, Tang Q, and Ober RJ. Analysis of the roles of Rab4 and Rab11 GTPases in the intracellular trafficking of the Fc receptor, FcRn. Mol Biol Cell 2004;15:75a-a.

[54] Christianson GJ, Sun VZ, Akilesh S, Pesavento E, Proetzel G, and Roopenian DC. Monoclonal antibodies directed against human FcRn and their applications. Mabs-Austin 2012;4:208-16.

[55] Akilesh S, Huber TB, Wu H, Wang G, Hartleben B, Kopp JB, et al. Podocytes use FcRn to clear IgG from the glomerular basement membrane. Proceedings of the National Academy of Sciences of the United States of America 2008;105:967-72.

[56] Ferreira MP, Ferrari RA, Gravalos ED, Martins MD, Bussadori SK, Gonzalez DA, et al. Effect of low-energy gallium-aluminum-arsenide and aluminium gallium indium phosphide laser irradiation on the viability of C2C12 myoblasts in a muscle injury model. Photomedicine and laser surgery 2009;27:901-6.

[57] Ferreira CL, Lamsa E, Woods M, Duan Y, Fernando P, Bensimon C, et al. Evaluation of bifunctional chelates for the development of gallium-based radiopharmaceuticals. Bioconjug Chem 2010;21:531-6.

[58] Akilesh S, Christianson GJ, Roopenian DC, and Shaw AS. Neonatal FcR expression in bone marrow-derived cells functions to protect serum IgG from catabolism. J Immunol 2007;179:4580-8.

[59] Aad G, Abbott B, Abdallah J, Abdelalim AA, Abdesselam A, Abdinov O, et al. Measurement of the jet fragmentation function and transverse profile in proton-proton collisions at a center-of-mass energy of 7 TeV with the ATLAS detector. Eur Phys J C 2011;71.

[60] Vlasak J and Ionescu R. Fragmentation of monoclonal antibodies. Mabs-Austin 2011;3:253-63.

[61] de Sa A, Matias AA, Prata MI, Geraldes CF, Ferreira PM, and Andre JP. Gallium labeled NOTA-based conjugates for peptide receptor-mediated medical imaging. Bioorganic & medicinal chemistry letters 2010;20:7345-8.

[62] Green DE, Ferreira CL, Stick RV, Patrick BO, Adam MJ, and Orvig C. Carbohydrate-bearing 3-hydroxy-4-pyridinonato complexes of gallium(III) and indium(III). Bioconjug Chem 2005;16:1597-609.

[63] Oehlke E, Lengkeek NA, Le VS, Pellegrini PA, Greguric I, and Weiner R. The role of additives in moderating the influence of Fe(III) and Cu(II) on the radiochemical yield of [(6)(8)Ga(DOTATATE)]. Applied radiation and isotopes : including data, instrumentation and methods for use in agriculture, industry and medicine 2016;107:13-6.

[64] Oehlke E, Le VS, Lengkeek N, Pellegrini P, Jackson T, Greguric I, et al. Influence of metal ions on the (6)(8)Ga-labeling of DOTATATE. Applied radiation and isotopes : including data, instrumentation and methods for use in agriculture, industry and medicine 2013;82:232-8.

[65] Loktionova NS, Belozub AN, Filosofov DV, Zhernosekov KP, Wagner T, Turler A, et al. Improved column-based radiochemical processing of the generator produced 68Ga. Applied radiation and isotopes : including data, instrumentation and methods for use in agriculture, industry and medicine 2011;69:942-6.

[66] Holland JP, Williamson MJ, and Lewis JS. Unconventional Nuclides for Radiopharmaceuticals. Mol Imaging 2010;9:1-20.

[67] Ak I, Stokkel MPM, and Pauwels EKJ. Positron emission tomography with 2-[F-18]fluoro-2-deoxy-D-glucose in oncology Part II. The clinical value in detecting and staging primary tumours. J Cancer Res Clin 2000;126:560-74.

[68] Fani M, Andre JP, and Maecke HR. 68Ga-PET: a powerful generator-based alternative to cyclotron-based PET radiopharmaceuticals. Contrast media & molecular imaging 2008;3:67-77.

[69] Zhernosekov KP, Filosofov DV, Baum RP, Aschoff P, Bihl H, Razbash AA, et al. Processing of generator-produced 68Ga for medical application. J Nucl Med 2007;48:1741-8.

[70] Vis R, Lavalaye J, and van de Garde EM. GMP-compliant (68)Ga radiolabelling in a conventional small-scale radiopharmacy: a feasible approach for routine clinical use. EJNMMI research 2015;5:27.

[71] Desmond KW, Zacchia NA, Waite JH, and Valentine MT. Dynamics of mussel plaque detachment. Soft matter 2015;11:6832-9.

[72] Wolfe AJ and Visick KL. Get the message out: cyclic-Di-GMP regulates multiple levels of flagellum-based motility. Journal of bacteriology 2008;190:463-75.

[73] Mastren T, Radchenko V, Bach HT, Balkin ER, Birnbaum ER, Brugh M, et al. Bulk production and evaluation of high specific activity 186gRe for cancer therapy using enriched 186WO3 targets in a proton beam. Nucl Med Biol 2017;49:24-9.

[74] Frangipani E, Visaggio D, Heeb S, Kaever V, Camara M, Visca P, et al. The Gac/Rsm and cyclic-di-GMP signalling networks coordinately regulate iron uptake in Pseudomonas aeruginosa. Environmental microbiology 2014;16:676-88.

[75] Engle JW, Lopez-Rodriguez V, Gaspar-Carcamo RE, Valdovinos HF, Valle-Gonzalez M, Trejo-Ballado F, et al. Very high specific activity (6)(6)/(6)(8)Ga from zinc targets for PET. Applied radiation and isotopes : including data, instrumentation and methods for use in agriculture, industry and medicine 2012;70:1792-6.

[76] Englebienne P and Slegers G. Estimation of the specific activity of radioiodinated gonadotrophins: comparison of three methods. J Immunol Methods 1983;56:135-40.

[77] Banerjee SR and Pomper MG. Clinical applications of Gallium-68. Applied radiation and isotopes : including data, instrumentation and methods for use in agriculture, industry and medicine 2013;76:2-13.

[78] Zeglis BM, Houghton JL, Evans MJ, Viola-Villegas N, and Lewis JS. Underscoring the influence of inorganic chemistry on nuclear imaging with radiometals. Inorg Chem 2014;53:1880-99.

[79] Griffeth LK. Use of PET/CT scanning in cancer patients: technical and practical considerations. Proceedings 2005;18:321-30.

[80] Slamon DJ, Clark GM, Wong SG, Levin WJ, Ullrich A, and McGuire WL. Human breast cancer: correlation of relapse and survival with amplification of the HER-2/neu oncogene. Science 1987;235:177-82.

[81] Anderson DW, Epstein JS, Lee TH, Lairmore MD, Saxinger C, Kalyanaraman VS, et al. Serological confirmation of human T-lymphotropic virus type I infection in healthy blood and plasma donors. Blood 1989;74:2585-91.

[82] Reissmann PT, Simon MA, Lee WH, and Slamon DJ. Studies of the retinoblastoma gene in human sarcomas. Oncogene 1989;4:839-43.

[83] Kastan MB, Slamon DJ, and Civin CI. Expression of protooncogene c-myb in normal human hematopoietic cells. Blood 1989;73:1444-51.

[84] Ehrlich GD, Davey FR, Kirshner JJ, Sninsky JJ, Kwok S, Slamon DJ, et al. A polyclonal CD4+ and CD8+ lymphocytosis in a patient doubly infected with HTLV-I and HIV-1: a clinical and molecular analysis. American journal of hematology 1989;30:128-39.

[85] Vosjan MJWD. P-Isothiocyanatobenzyl-desferrioxamine: a new bifunctional chelate for facile radiolabeling of monoclonal antibodies with zirconium-89 for immuno-PET imaging. Eur J Nucl Med Mol I 2009;36:S233-S.

[86] Reubi JC, Kvols L, Krenning E, and Lamberts SW. Distribution of somatostatin receptors in normal and tumor tissue. Metabolism: clinical and experimental 1990;39:78-81.

[87] Pillai MRA, Dash A, and Knapp FF. Sustained Availability of Tc-99m: Possible Paths Forward. J Nucl Med 2013;54:313-23.

[88] Hoehr C, Morley T, Buckley K, Trinczek M, Hanemaayer V, Schaffer P, et al. Radiometals from liquid targets: 94mTc production using a standard water target on a 13 MeV cyclotron. Applied radiation and isotopes : including data, instrumentation and methods for use in agriculture, industry and medicine 2012;70:2308-12.

[89] Benard F, Buckley KR, Ruth TJ, Zeisler SK, Klug J, Hanemaayer V, et al. Implementation of Multi-Curie Production of Tc-99m by Conventional Medical Cyclotrons. J Nucl Med 2014;55:1017-22.

[90] Yoshinaga K, Klein R, and Tamaki N. Generator-produced rubidium-82 positron emission tomography myocardial perfusion imaging-From basic aspects to clinical applications. J Cardiol 2010;55:163-73.

[91] Rosch F. Past, present and future of 68Ge/68Ga generators. Applied radiation and isotopes : including data, instrumentation and methods for use in agriculture, industry and medicine 2013;76:24-30.

[92] Rosch RPBaF. Theranostics, Gallium-68, and Other Radionuclides. Berlin: Springer; 2013, p. 3-16.

[93] Jahangiri P, Zacchia NA, Buckley K, Benard F, Schaffer P, Martinez DM, et al. An analytical approach of thermodynamic behavior in a gas target system on a medical cyclotron. Appl Radiat Isotopes 2016;107:252-8.

[94] Zacchia NA, Martinez DM, and Hoehr C. Foil degradation in a salt solution target. AIP Conference Proceedings 2017;1845:020024.

[95] Uddin MS, Hagiwara M, Baba M, Tarkanyi F, and Ditroi F. Experimental studies on excitation functions of the proton-induced activation reactions on yttrium. Applied radiation and isotopes : including data, instrumentation and methods for use in agriculture, industry and medicine 2005;63:367-74.

[96] Koukourakis MI, Giatromanolaki A, Bottini A, Cappelletti MR, Zanotti L, Allevi G, et al. Prospective neoadjuvant analysis of PET imaging and mechanisms of resistance to Trastuzumab shows role of HIF1 and autophagy. Br J Cancer 2014;110:2209-16.

[97] Milani A, Montemurro F, Gioeni L, Aglietta M, and Valabrega G. Role of trastuzumab in the management of HER2-positive metastatic breast cancer. Breast cancer 2010;2:93-109.

[98] Xu H, Baidoo KE, Wong KJ, and Brechbiel MW. A novel bifunctional maleimido CHX-A" chelator for conjugation to thiol-containing biomolecules. Bioorganic & medicinal chemistry letters 2008;18:2679-83.

[99] Zacchia NA and Valentine MT. Design and optimization of arrays of neodymium iron boron-based magnets for magnetic tweezers applications. Review of Scientific Instruments 2015;86.

[100] Holland JP, Sheh YC, and Lewis JS. Standardized methods for the production of high specific-activity zirconium-89. Nucl Med Biol 2009;36:729-39.

[101] Kobayashi H, Wu C, Yoo TM, Sun BF, Drumm D, Pastan I, et al. Evaluation of the in vivo biodistribution of yttrium-labeled isomers of CHX-DTPA-conjugated monoclonal antibodies. J Nucl Med 1998;39:829-36.

[102] Boswell CA and Brechbiel MW. Development of radioimmunotherapeutic and diagnostic antibodies: an inside-out view. Nucl Med Biol 2007;34:757-78.

[103] McCarthy DW, Shefer RE, Klinkowstein RE, Bass LA, Margeneau WH, Cutler CS, et al. Efficient production of high specific activity 64Cu using a biomedical cyclotron. Nucl Med Biol 1997;24:35-43.

[104] Goldenberg DM, Juweid M, Dunn RM, and Sharkey RM. Cancer imaging with radiolabeled antibodies: new advances with technetium-99m-labeled monoclonal antibody Fab' fragments, especially CEA-Scan and prospects for therapy. Journal of nuclear medicine technology 1997;25:18-23; quiz 34.

[105] Pandey MK, Bansal A, Engelbrecht HP, Byrne JF, Packard AB, and DeGrado TR. Improved production and processing of (8)(9)Zr using a solution target. Nucl Med Biol 2016;43:97-100.

[106] Wu AM. Engineered antibodies for molecular imaging of cancer. Methods 2014;65:139-47.

[107] Higgins LJ and Pomper MG. The evolution of imaging in cancer: current state and future challenges. Seminars in oncology 2011;38:3-15.

[108] Pandey MK, Engelbrecht HP, Byrne JP, Packard AB, and DeGrado TR. Production of 89Zr via the 89Y(p,n)89Zr reaction in aqueous solution: effect of solution composition on in-target chemistry. Nucl Med Biol 2014;41:309-16.

[109] Oehlke E, Hoehr C, Hou X, Hanemaayer V, Zeisler S, Adam MJ, et al. Production of Y-86 and other radiometals for research purposes using a solution target system. Nucl Med Biol 2015;42:842-9.

[110] Pauwels EKJ, Sturm EJC, Bombardieri E, Cleton FJ, and Stokkel MPM. Positron-emission tomography with [F-18]fluorodeoxyglucose Part I. Biochemical uptake mechanism and its implication for clinical studies. J Cancer Res Clin 2000;126:549-59.

[111] Lonneux M, Lawson G, Ide C, Bausart R, Remacle M, and Pauwels S. Positron emission tomography with fluorodeoxyglucose for suspected head and neck tumor recurrence in the symptomatic patient. Laryngoscope 2000;110:1493-7.

[112] Goldenberg DM. Carcinoembryonic antigen as a target cancer antigen for radiolabeled antibodies: prospects for cancer imaging and therapy. Tumour biology : the journal of the International Society for Oncodevelopmental Biology and Medicine 1995;16:62-73.

[113] Goldenberg DM. Targeting of cancer with radiolabeled antibodies. Prospects for imaging and therapy. Archives of pathology & laboratory medicine 1988;112:580-7.

[114] Munley MT, Kagadis GC, McGee KP, Kirov AS, Jang S, Mutic S, et al. An introduction to molecular imaging in radiation oncology: a report by the AAPM Working Group on Molecular Imaging in Radiation Oncology (WGMIR). Medical physics 2013;40:101501.

[115] Kumar R, Sonkawade RG, Tripathi M, Sharma P, Gupta P, Kumar P, et al. Production of the PET bone agent (18)F-fluoride ion, simultaneously with (18)F-FDG by a single run of the medical cyclotron with minimal radiation exposure- a novel technique. Hellenic journal of nuclear medicine 2014;17:106-10.

[116] Meares CF, McCall MJ, Reardan DT, Goodwin DA, Diamanti CI, and McTigue M. Conjugation of antibodies with bifunctional chelating agents: isothiocyanate and bromoacetamide reagents, methods of analysis, and subsequent addition of metal ions. Anal Biochem 1984;142:68-78.

[117] Kircher MF, Hricak H, and Larson SM. Corrigendum to "Molecular imaging for personalized cancer care" [Mol. Oncol. 6(2) (2012) 182-195]. Molecular oncology 2016;10:1627.

[118] Kircher MF, Hricak H, and Larson SM. Molecular imaging for personalized cancer care. Molecular oncology 2012;6:182-95.

[119] Qaim SM. Nuclear data for production and medical application of radionuclides: Present status and future needs. Nucl Med Biol 2017;44:31-49.

[120] Papapanagiotou A, Daskalakis G, Siasos G, Gargalionis A, and Papavassiliou AG. The Role of Platelets in Cardiovascular Disease: Molecular Mechanisms. Current pharmaceutical design 2016;22:4493-505.

[121] Krysko DV, Agostinis P, Krysko O, Garg AD, Bachert C, Lambrecht BN, et al. Emerging role of damage-associated molecular patterns derived from mitochondria in inflammation. Trends in immunology 2011;32:157-64.

[122] Fillingham JS, Garg J, Tsao N, Vythilingum N, Nishikawa T, and Pearlman RE. Molecular genetic analysis of an SNF2/brahma-related gene in Tetrahymena thennophila suggests roles in growth and nuclear development. Eukaryot Cell 2006;5:1347-59.

[123] Thisgaard H, Jensen M, and Elema DR. Medium to large scale radioisotope production for targeted radiotherapy using a small PET cyclotron. Appl Radiat Isotopes 2011;69:1-7.

[124] Imai K and Takaoka A. Comparing antibody and small-molecule therapies for cancer. Nat Rev Cancer 2006;6:714-27.

[125] Trillsch F, Kuerti S, Eulenburg C, Burandt E, Woelber L, Prieske K, et al. E-Cadherin fragments as potential mediators for peritoneal metastasis in advanced epithelial ovarian cancer. Br J Cancer 2016;114:207-12.

[126] van Dongen GA, Visser GW, Lub-de Hooge MN, de Vries EG, and Perk LR. Immuno-PET: a navigator in monoclonal antibody development and applications. The oncologist 2007;12:1379-89.

[127] Warram JM, de Boer E, Sorace AG, Chung TK, Kim H, Pleijhuis RG, et al. Antibody-based imaging strategies for cancer. Cancer metastasis reviews 2014;33:809-22.

[128] Vrouenraets MB, Visser GW, Stewart FA, Stigter M, Oppelaar H, Postmus PE, et al. Development of meta-tetrahydroxyphenylchlorin-monoclonal antibody conjugates for photoimmunotherapy. Cancer Res 1999;59:1505-13.

[129] Gagnon K, Jensen M, Thisgaard H, Publicover J, Lapi S, McQuarrie SA, et al. A new and simple calibration-independent method for measuring the beam energy of a cyclotron. Applied radiation and isotopes : including data, instrumentation and methods for use in agriculture, industry and medicine 2011;69:247-53.

[130] Fosgerau K and Hoffmann T. Peptide therapeutics: current status and future directions. Drug discovery today 2015;20:122-8.

[131] Lacaille J, Ly J, Zacchia N, Bourkas S, Glaser E, and Knauper B. The effects of three mindfulness skills on chocolate cravings. Appetite 2014;76:101-12.

[132] Stokely MH. Deployment, Testing and Analysis of Advanced Thermosyphon Target Systems for Production of Aqueous Fluorine-18 Via Oxygen-18 (p,n) fluorine-18. Raleigh, North Carolina: North Carolina State University; 2008.

[133] Psimadas D, Fani M, Gourni E, Loudos G, Xanthopoulos S, Zikos C, et al. Synthesis and comparative assessment of a labeled RGD peptide bearing two different (9)(9)mTc-tricarbonyl chelators for potential use as targeted radiopharmaceutical. Bioorganic & medicinal chemistry 2012;20:2549-57.

[134] Fani M, Maecke HR, and Okarvi SM. Radiolabeled peptides: valuable tools for the detection and treatment of cancer. Theranostics 2012;2:481-501.

[135] Weissleder R and Pittet MJ. Imaging in the era of molecular oncology. Nature 2008;452:580-9.

[136] Pandey MK, Byrne JF, Jiang H, Packard AB, and DeGrado TR. Cyclotron production of (68)Ga via the (68)Zn(p,n)(68)Ga reaction in aqueous solution. American journal of nuclear medicine and molecular imaging 2014;4:303-10.

[137] Oehlke E, Hoehr C, Hou XC, Hanemaayer V, Zeisler S, Adam MJ, et al. Production of Y-86 and other radiometals for research purposes using a solution target system. Nucl Med Biol 2015;42:842-9.

[138] Oehlke E, Le V, Lengkeek N, Pellegrini P, Jackson T, Greguric I, et al. Influence of metal ions on the Ga-68-labeling of DOTATATE. Appl Radiat Isotopes 2013;82:232-8.

[139] Oehlke E, Lengkeek NA, Le VS, Pellegrini PA, Greguric I, and Weiner R. The role of additives in moderating the influence of Fe(III) and Cu(II) on the radiochemical yield of [Ga-68(DOTATATE)]. Appl Radiat Isotopes 2016;107:13-6.

[140] Seo Y, Mari C, and Hasegawa BH. Technological development and advances in single-photon emission computed tomography/computed tomography. Seminars in nuclear medicine 2008;38:177-98.

[141] Pourmand A and Dauphas N. Distribution coefficients of 60 elements on TODGA resin: application to Ca, Lu, Hf, U and Th isotope geochemistry. Talanta 2010;81:741-53.

[142] Hoehr C, Oehlke E, Benard F, Lee CJ, Hou X, Badesso B, et al. (44g)Sc production using a water target on a 13MeV cyclotron. Nucl Med Biol 2014;41:401-6.